

Design of a DC/DC Step-Down Converter for Electrolyzers Powered by LVDC Grids

Merijn Van Deyck

Thesis voorgedragen tot het behalen
van de graad van Master of Science
in de ingenieurswetenschappen:
energie

Promotoren:

Prof. Dr. Ir. Johan Driesen
Prof. Dr. Ir. Wilmar Martinez

Assessoren:

Prof. Dr. Ir. Johan Driesen
Prof. Dr. Ir. Wilmar Martinez
Dipl.-Phys Jens D. Moschner
Prof. Dr. Ir. Ruth V. Sabariego

Begeleider:

Ir. Mohamed A. Yasko

© Copyright KU Leuven

Zonder voorafgaande schriftelijke toestemming van zowel de promotoren als de auteur is overnemen, kopiëren, gebruiken of realiseren van deze uitgave of gedeelten ervan verboden. Voor aanvragen tot of informatie i.v.m. het overnemen en/of gebruik en/of realisatie van gedeelten uit deze publicatie, wend u tot Faculteit Ingenieurswetenschappen, Kasteelpark Arenberg 1 bus 2200, B-3001 Heverlee, +32-16-321350.

Voorafgaande schriftelijke toestemming van de promotoren is eveneens vereist voor het aanwenden van de in deze masterproef beschreven (originele) methoden, producten, schakelingen en programma's voor industrieel of commercieel nut en voor de inzending van deze publicatie ter deelname aan wetenschappelijke prijzen of wedstrijden.

Preface

Working on a project as important and large as a master thesis is not an easy task. The pressure and excitement that comes with devising and writing this project, which represents the final obstacle as well as the crown piece of the successful completion of an education, is not to be underestimated. I am therefore certain that I would not have been able to complete this project without the help and support of some people whom I would like to thank here.

Firstly, I want to thank my promotor and copromotor Prof. Dr. Ir. Johan Driesen and Prof. Dr. Ir. Wilmar Martinez and my daily supervisor Ir. Mohammed Yasko. Their guidance during all stages of this project has helped me discover and rediscover the directions to give to this thesis. Thanks to their guidance and opportunities for self reflection, I was able to present this thesis in its most interesting, challenging and relevant form. In this regard, I would like to offer my supervisor Ir. Mohammed Yasko my special thanks for his guidance in our many personal meetings in which he challenged me and helped me figure out and achieve the goals that I set in this project.

My thanks also go out to my assessors Prof. Dr. Ir. Ruth V. Sabariego and Dipl.-Phys. Jens D. Moschner, in addition to my promotor and copromotor, for taking the time to read and evaluate this thesis and my final presentation. I highly value their input from the intermediate presentation and look forward to discussing their professional and critical opinion on this thesis during the final presentation.

I would like to extend my special thanks to my family. My parents and siblings' unwavering interest and support for what I was doing has kept me motivated and energized throughout the year. Finally, I would sincerely like to thank my girlfriend Eveline, who deserves enormous praise for listening to me talk about this thesis every day and whose experience, guidance and support have been essential realising this project.

Thank you to everyone who has helped make this thesis a reality.

Contents

Preface	i
Contents	i
Abstract	iv
Samenvatting	v
List of Figures	v
List of Tables	vii
1 Introduction	1
1.1 Positioning of the Research	1
1.2 Contribution to Existing Research	2
1.3 Research Goals	2
1.4 Thesis Outline	3
2 Literature Study	5
2.1 Introduction	5
2.2 Applications for Green Hydrogen	5
2.3 Electrolyzer Technology	11
2.4 Energy Consumption	14
2.5 Use Case Analysis	17
2.6 DC/DC Converter Technology	19
2.7 Conclusion	24
3 Electrolyzer Modeling	27
3.1 Introduction	27
3.2 Voltage Calculation	27
3.3 Transport Mechanisms	33
3.4 Commercial Electrolyzer Model	38
3.5 Electrical Model	39
3.6 Conclusion	41
4 Converter Design	43
4.1 Introduction	43
4.2 Input Conditions	43
4.3 Design Methodology	45
4.4 Basic Topology	46

4.5	Interleaved Buck Converter Design	50
4.6	Losses	55
4.7	Alternative designs	57
4.8	Conclusion	62
5	Simulation Results	65
5.1	Introduction	65
5.2	Capacitor Losses	66
5.3	Nominal Converter Efficiency	67
5.4	Solar Farm Operation Efficiency	67
5.5	Modular Implementation Results	70
5.6	Conclusion	72
6	Results Discussion	75
6.1	Introduction	75
6.2	Final Topology Design	75
6.3	Total System Efficiency	77
6.4	Conclusion	80
7	Conclusion	81
7.1	Contribution to Existing Research	81
7.2	Evaluation of the Research Questions	81
7.3	Further Research	83
	Bibliography	85
A	Electrolyzer Model Code	99
A.1	Anode Function	99
A.2	Cathode Function	99
A.3	Membrane Function	100
A.4	Voltage Function	102
B	Component Datasheets	105
B.1	HCS-201M-600A	105
B.2	Semitrans 3 IGBT	106
B.3	DSEI-120-12A	111
B.4	C44P-R	114
B.5	IHXL-1500VZ-5A	115
B.6	IXYH85N120A4	120
B.7	FGH40T120SQDNL4	128
C	Detailed Plecs Models	139
C.1	Electrolyzer Model	139
C.2	700 V IBC Model	140
C.3	1000 V IBC Model	141
D	PV Case Study Scripts	143
D.1	Solar Generation Data Processing	143
D.2	Approximate IU-Setpoint Calculation	144
D.3	Detailed IU-Setpoint Calculation	145

Abstract

The energy transition towards a decarbonized system has caused the rise of many new technologies to replace traditional carbon-emitting energy sources. Today, hydrogen is already widely used as a resource in the chemical industry. However, it is also expected that this substance will play an important role as an energy carrier, to offer potential for decarbonization where this is not possible through electrification. Contrary to how hydrogen is currently mostly produced from natural gas, clean hydrogen requires renewable electricity through a process known as electrolysis. Efficiently executing this process is a prerequisite to hydrogen becoming a viable part of the energy system of the future.

The electrolyzer considered in this thesis is based on a commercial PEM electrolyzer by an unnamed company (**Company**). By means of an AC/DC rectifier, this electrolyzer can be powered by a connection to the AC electricity grid. It is however considered in literature that in systems with high local renewable generation and DC loads, the use of a LVDC grid leads to significant efficiency improvements. The value of hydrogen in the energy transition can only be achieved if renewable energy is used for the electrolysis process. The goal of this thesis is therefore to study the possible efficiency gains made by operating the commercial electrolyzer system from a DC input voltage, such as a LVDC grid or a direct connection to a solar farm. Literature concerning converters for electrolyzers mostly focuses on small scale systems considering the low input voltage of a single electrolyzer cell. However, the 1.7 MW scale commercial electrolyzer has different characteristics, such as the higher voltage and current requirement.

Consequently, in this thesis an interleaved buck converter (IBC) is developed with commercially available components. The requirements for this converter design are defined based on a literature review on the working principles of electrolyzers and DC/DC converters. The IBC is modeled based on realistic components that can be considered in simulations with which the achieved efficiency improvements are calculated. An efficiency of 99.13% is achieved for the converter design, compared to the original rectifier efficiency of 97%. Furthermore, the connection to a LVDC grid using this converter proves more efficient if at least 28.38% of the power is directly injected into the grid by local PV generation.

Finally, a case study concerning a direct connection to a solar farm in Belgium or Morocco is conducted. This shows that, on a yearly basis, an increased hydrogen output of 17370 Nm³ and 27220 Nm³ respectively can be generated by utilizing the developed IBC instead of an inverter-rectifier implementation.

Samenvatting

De energietransitie naar een gedecarboniseerd energiesysteem leidt tot nieuwe technologieën bedoeld om energiebronnen met een hoge CO₂ uitstoot te vervangen. Vandaag de dag is waterstof een veelgebruikte grondstof in de chemische industrie. Er wordt echter verwacht dat deze substantie een belangrijke rol zal spelen als energiedrager om sectoren te decarboniseren waar dit niet mogelijk is via electrificatie. In tegenstelling tot de huidige productiemethode van waterstof, op basis van aardgas, moet *schone* waterstof gegenereerd worden door elektrolyse met hernieuwbare elektriciteit. Het is noodzakelijk om dit proces efficiënt uit te voeren om waterstof een duurzaam onderdeel te maken van het energiesysteem van de toekomst.

De electrolyzer in deze thesis is gebaseerd op de commerciële PEM electrolyzer van een anoniem bedrijf (**Company**). Via een AC/DC gelijkrichter wordt deze electrolyzer aangedreven door het AC elektriciteitsnet. In wetenschappelijke literatuur wordt gesteld dat in systemen met veel lokale hernieuwbare generatie en DC afname, een LVDC net leidt tot significante efficiëntieverhogingen. De waarde van waterstof in de energietransitie kan enkel gerealiseerd worden door het gebruik van hernieuwbare energie voor de elektrolyse. Het doel van deze thesis is daarom om te onderzoeken welke toenames in efficiëntie gerealiseerd kunnen worden door het aandrijven van de electrolyzer met LVDC net of een directe connectie met een PV-generatievoorziening. De wetenschappelijke literatuur betreffende convertoren voor electrolyzers focust voornamelijk op kleinschalige systemen waarin de lage spanning van een enkele electrolyzer cel overwogen worden. De commerciële electrolyzer op een schaal van 1.7 MW heeft echter andere vereisten zoals een hogere ingangsspanning en -stroom.

Bijgevolg wordt er in deze thesis een *interleaved buck converter* (IBC) ontwikkeld met commercieel beschikbare componenten. De vereisten voor het ontwerp van deze converter worden gedefinieerd gebaseerd op een literatuurstudie over de werkingsprincipes van electrolyzers en DC/DC converters. De IBC wordt gemodelleerd met realistische componenten die gesimuleerd worden zodat de toename in efficiëntie berekend kan worden. Het converter-ontwerp bereikt een efficiëntie van 99.13%, vergeleken met de 97% van de originele gelijkrichter. Bovendien is het gebruik van een LVDC net met deze converter efficiënter als minstens 28.38% van het vermogen direct geïnjecteerd wordt door lokale PV generatie.

Ten slotte blijkt uit een case study dat, voor een directe aansluiting met een PV-generatievoorziening in België en in Marokko, op jaarbasis respectievelijk 17370 Nm³ en 27220 Nm³ extra waterstof gegenereerd kan worden, door het gebruiken van de ontwikkelde IBC in plaats van een inverter-gelijkrichter implementatie.

List of Figures

1.1	Graphical representation of the research positioning compared to existing literature and commercial implementations	3
2.1	Belgian natural gas consumption statistics	9
2.2	Representation of the main benefits and disadvantages of the different applications for renewable hydrogen	12
2.3	Schematic representation of alkaline and PEM electrolysis and their governing reactions [51]	13
2.4	Polarization curve of electrolyzer cell	16
2.5	Basic buck converter circuit	19
2.6	Buck converter output current behavior for a single cycle	20
2.7	Basic circuit model of a 6-phase IBC	21
2.8	Improved IBC proposed in [93]	22
2.9	Loss analysis for the improved IBC from [93] for $D < 0.5$ at switching frequency of 300 kHz and 240 W output power	23
2.10	Isolated DC/DC converter topologies	23
2.11	Three phase FBC proposed in [100] for high power applications	24
3.1	Resistance model of the electrode and plate	29
3.2	Simplified resistive circuit model for electrode and bipolar flow plate	30
3.3	Representation of the bipolar plate consisting of channels and support structures, n_{ch} is chosen based on this figure and H is set equal to the average channel length [103]	32
3.4	Simulink model calculating the voltage of the electrolyzer based on the mass transport mechanisms in the anode, cathode and membrane, dependent on the input current and pressures	33
3.5	Stack model of the serialized electrolyzer cells	39
3.6	Dynamic electrical equivalent model of a PEM electrolyzer	40
3.7	Electrical equivalent electrolyzer model used in power electronic simulations	41
4.1	IU-curves of a monocrystalline PV modules for varying irradiance levels	45
4.2	Voltage waveforms relative to the input voltage at different points in the FBC	47
4.3	Three-phase FBC with a Yd connection	47
4.4	Output current ripple characteristic for an IBC with up to six phases	50

4.5	Inductance of the output inductors in depending on the applied DC current	51
4.6	Semitrans IGBT used in the DC/DC converter design	52
4.7	Current ripple at the output of the converter for different sizes of output capacitor	54
4.8	Resistive voltage drops in a single converter leg	57
4.9	Buck converter with a ZCS and ZVS resonant circuit	62
5.1	DC/DC converter efficiency for variable output power setpoints at the solar farm input voltage	70
5.2	Total output current and ripple of the modular systems going into the the electrolyzer	72
6.1	Final six-phase IBC design	76

List of Tables

3.1	Assumed values for unknown parameters in the electrolyzer model	34
3.2	Operating data of the Commercial Electrolyzer	38
4.1	Operating characteristics of the Sunpower Maxeon 3 module used in the solar farm case study	44
4.2	Maximum current ripple for different output capacitor sizes	55
4.3	Price list for the designed interleaved converter	55
4.4	Loss characteristics of the components in the DC/DC converter	56
4.5	Components used in modular converter design using 12 or 24 phases	59
4.6	Minimum inductance to avoid DCM in modular converter implementations	60
4.7	Costs for the modular converter topologies	61
5.1	Efficiency and ripple comparison for converters modeled with or without the non-ideal output capacitor	67
5.2	Efficiency results for the two main IBC designs operating the electrolyzer at nominal power	67
5.3	Electrolyzer current and voltage setpoints demanded at the output of the DC/DC converter for varying power setpoints	68
5.4	Electrolyzer current and voltage setpoints demanded at the output of the DC/DC converter for varying power setpoints	69
5.5	Input conditions and output results for the six-phase IBC operated at minimal phase requirement	71
5.6	Results for the different modular implementations	71
5.7	Required ideal capacitors to reduce the ripple to 1% for a purely resistive load	72
6.1	Input voltage, efficiency and ripple factor for the converter topologies, operating at the optimal duty cycle at nominal capacity	76
6.2	System results for PV hydrogen	78
6.3	Total hydrogen output and energy efficiency for PV based hydrogen production in different locations	79
6.4	Electrolyzer setpoints and efficiency for inverter-rectifier PV farm connection	79
6.5	Total hydrogen output and energy efficiency for PV based hydrogen production in different locations	80

Nomenclature

Physics Constants

F	Faraday constant
R	Universal gas constant

Symbols

η	Efficiency	t	Time
P	Power	T_s	Period duration
I	Current	f	Frequency
U	Voltage	N	Number of phases
x	Volumetric fraction	N_t	Transformer winding ratio
\dot{V}	Volumetric flow	R	Converter voltage ratio
E	Energy	i	Current density
ΔG	Gibbs free energy	α	Charge transfer coefficient
ΔH	Gibbs free enthalpy	R_{ohm}	Ohmic resistance of the electrolyzer
ΔS	Entropy difference	ρ	Resistivity
T	Temperature	δ_{el}	Electrode thickness
p	Pressure	h_c	Channel height
D	Duty cycle	h_p	Plate thickness
S	Switch	w_c	Channel width
L	Inductor	w_s	Channel support width
C	Capacitor	W	MEA width
$D1$	Diode	H	MEA height
		A	Surface area of the MEA
		σ	Conductivity
		λ	Water content of the membrane
		ϵ	Porosity
		r	Radius

C_x^y	Concentration of substance x at location y	<i>SME</i>	Small and medium-sized enterprise
$C_{x,0}^y$	Reference concentration of substance x at location y	<i>CHP</i>	Combined heat and power
X	Molar fraction	<i>HHV</i>	Higher heating value
n	Molar flux	<i>LHV</i>	Lower heating value
D_{eff}	Effective diffusion coefficient	<i>DRI</i>	Direct reduced iron
J	Diffusion flux	<i>RMS</i>	Root mean square
ξ	tortuosity	<i>MV</i>	Medium voltage
M_i	Molar mass of i	<i>CCM</i>	Continuous conduction mode
Ω_D	Diffusion collision integral	<i>IBC</i>	Interleaved buck converter
σ_{x-y}	Average molecular radius of x and y	<i>HBC</i>	Half-bridge converter
τ	Dimensionless temperature	<i>FBC</i>	Full-bridge converter
\dot{N}	Molar flow rate	<i>AC</i>	Alternating current
ρ_{H_2O}	Density of water	<i>Com.El.</i>	Commercial Electrolyzer
μ_{H_2O}	Viscosity of water	<i>RES</i>	Renewable energy sources
n_d	Electro-osmotic drag coefficient	<i>an</i>	Anode
K_{darcy}	Membrane permeability	<i>cat</i>	Cathode
Other Abbreviations		<i>MEA</i>	Membrane electrode assembly
<i>DC</i>	Direct current	<i>MPPT</i>	Maximum power point tracking
<i>LVDC</i>	Low voltage DC	<i>D</i>	Delta connection of a transformer
<i>PEM</i>	Proton exchange membrane	<i>Y</i>	Star connection of a transformer
<i>PV</i>	Photovoltaic	<i>IGBT</i>	Insulated gate bipolar transistor
<i>BEV</i>	Battery electric vehicle	<i>RF</i>	Ripple factor
<i>CAES</i>	Compressed air energy storage	<i>ZCS</i>	Zero current switching
<i>FCEV</i>	Fuel cell electric vehicle	<i>ZVS</i>	Zero voltage switching
<i>GHG</i>	Greenhouse gas	<i>BE</i>	Belgium
		<i>MA</i>	Morocco

Chapter 1

Introduction

1.1 Positioning of the Research

In the ongoing transition towards a decarbonized energy system, hydrogen is expected to have an increasingly large role. Its potential to be used as an energy carrier, a chemical feedstock or a resource to produce *synthetic natural gas* makes hydrogen an essential product to decarbonize sectors with a large carbon footprint. The European Union has the ambition to develop 40 GW of electrolyzer capacity within its borders and additionally import a hydrogen capacity of 40 GW from electrolyzers in other, nearby countries by 2030. Furthermore, by 2050 the EU plans to invest between €180-470 billion in renewable hydrogen technology [1]. According to scenarios from IRENA, 8% of the total energy consumption in 2050 would be in the form of hydrogen (of which 6% would be green hydrogen) [2]. BloombergNEF poses that at least 7% of global energy consumption in the form of clean hydrogen would be required in scenarios where total global warming is kept at 1.5°C. With strong supportive policy this could increase up to 24% requiring 11 trillion USD of global investments [3]. Regardless if these scenarios turn out to come true in the future, it is clear that the ambitions of governments and investors are high to make hydrogen an ever increasing part of the European and global energy system.

Today, hydrogen production accounts for 2% of the global primary energy demand. However, around 98% of this production is based on natural gas and coal as the primary resource [4]. Thus, it is clear that if hydrogen is to play a role in mitigating climate change, it will be essential that it is produced in an emission-free way. Therefore, hydrogen policies and scenarios put a clear focus on what is known as *green*, *clean* or *renewable* hydrogen, all meaning hydrogen produced through water electrolysis with electricity from renewable energy sources (RES) [1]. Consequently, water electrolysis will in the coming years have to evolve from being only a minor hydrogen source. Becoming the main production method and a large portion of the global demand for renewable electricity. It is therefore imperative that clean hydrogen can be generated efficiently and cost competitively, as an alternative to fossil-based hydrogen to decrease the overall energy cost of the future energy system.

The efficiency of electrolyzer systems can be defined as the energy contained in

the produced hydrogen compared to the supplied electrical energy. This electrical energy has to be supplied as a DC current, since the electrical charge must be steadily applied at the anode side of the electrolyzer. A certain voltage is required to ensure that the right amount of energy is supplied to the electrolyzer. Since the hydrogen output is solely dependent on the input current¹, the efficiency of an electrolyzer can be increased by keeping the input voltage, and thus the electrical power, as low to the required minimum as possible. As a result, the efficiency of hydrogen production through electrolysis is linked to the way the energy is supplied. For this reason, power electronic converters are used to deliver electrical power in the way most suited for the operation of the electrolyzer. In this thesis, the design of a step-down DC/DC converter is considered to efficiently power a commercial PEM electrolyzer from a low-voltage DC (LVDC) grid. At the request of the producer of this electrolyzer, referred to as **Company**, the specific name of the considered electrolyzer model is not included. The commercial electrolyzer, modeled in this thesis and informing the design of a DC/DC converter is referred to as **Commercial Electrolyzer**.

Research has proven that local DC grids offer significant efficiency and reliability advantages in many cases, especially in systems with high PV generation, battery storage and many DC loads [5–7]. Therefore, it is aspired that by connecting the electrolyzer to a DC grid, the efficiency of hydrogen production can be maximized.

1.2 Contribution to Existing Research

This thesis aims to contribute to existing research on DC/DC converters for electrolyzer systems by developing solutions for a commercial electrolyzer based on off-the-shelf components. Due to the scale difference in commercial electrolyzers and scientific models or prototypes, the principles defined in literature are not always directly transferable to industrial applications. Thus it is the goal of this thesis to build upon the existing research by providing concrete converter options that producers of commercial electrolyzers may implement to improve the efficiency of their hydrogen production process. Figure 1.1 illustrates how this thesis attempts to fill the gap between the commercial implementation of electrolyzers and existing research concerning small scale prototypes.

1.3 Research Goals

The aim of this thesis is to develop a DC/DC converter that is able to efficiently supply an electrolyzer with DC power at its optimal voltage setpoint. The purpose is to have this converter operate at a high efficiency to maximize the total system efficiency from the power supply to the hydrogen output of the electrolyzer. To this end, the research is conducted based on the following research questions:

¹Other factors such as the surrounding temperature and pressure affect the required voltage.

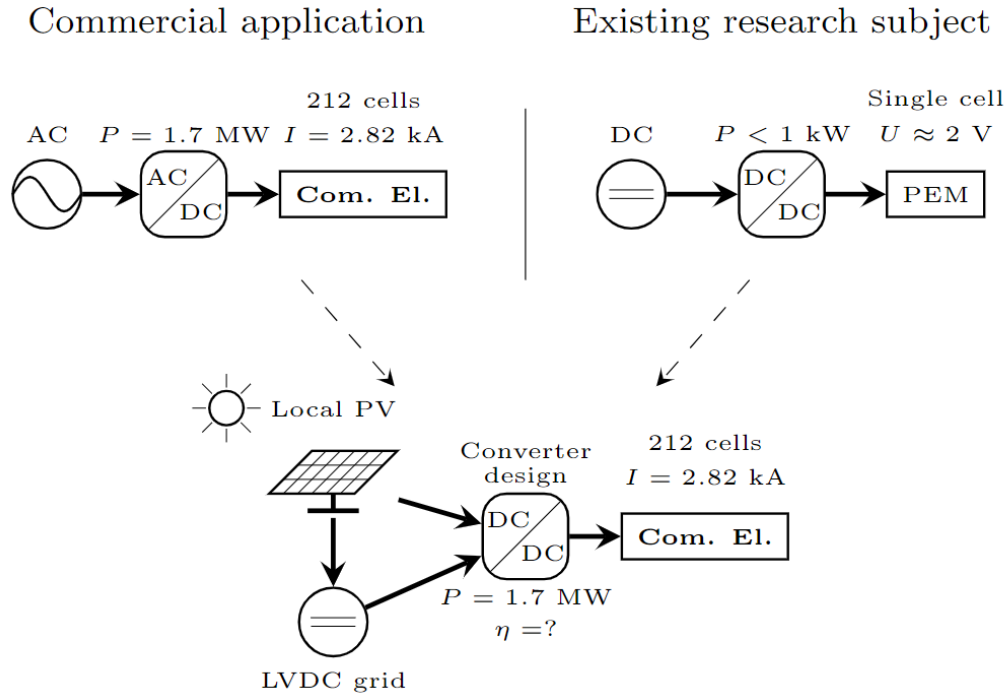


FIGURE 1.1: Graphical representation of the research positioning compared to existing literature and commercial implementations

- **Q1:** How to efficiently operate an electrolyzer? Which internal mechanisms govern the power losses and how can they be modeled to find the most efficient operating point?
- **Q2:** Which DC/DC converter topologies are suitable to operate an electrolyzer connected to a LVDC grid?
- **Q3:** How does the selected DC/DC converter perform in several relevant operating conditions compared to a commercial reference solution?
- **Q4:** Can further improvements to the system efficiency be made by adjusting the design and/or the control principles of the DC/DC converter?

1.4 Thesis Outline

To provide an answer to these research questions, a literature review is conducted in Chapter 2. This study provides a more detailed overview of the applications of hydrogen, as well as the principles of LVDC grids, in order to provide a clear justification of the research intent. Additionally, the literature review provides an overview of the working principles of electrolyzers and DC/DC converters so that sufficient knowledge can be acquired to accurately model, design, simulate and analyze the considered systems.

In Chapter 3 the construction of a model describing the functioning of an electrolyzer cell is discussed. The working principles of the electrolyzer, upon which this model is based, are explained. Then the selected electrolyzer model used in the analyses is described. The model is used to determine the most efficient power setpoint for the electrolyzer and provide the current and voltage specifications at the output side of the DC/DC converter.

Chapter 4 treats the design methodology of a suitable DC/DC converter, outlining the input and output conditions and setting the design criteria. Suitable basic topologies are considered in the literature review and further investigated in Chapter 4. Consequently, the selected topology is modeled using realistic off-the-shelf components. It is then further considered if any improvements can be made to the design, taking into account the basic working principles of the DC/DC converter and the limits of the components.

The designs proposed in Chapter 4 are modeled in PLECS. Chapter 5 presents the results of these simulations, listing the converter efficiency and output ripple for the different considered operating conditions. Based on these simulation results, a conclusion on the final design and total system efficiency is made in Chapter 6. The resulting system is compared to the standard configuration used by **Company** to achieve insight on the value and potential energy or cost savings of the design developed in this thesis.

Chapter 2

Literature Study

2.1 Introduction

This chapter aims to provide insight into the different fields relevant to this thesis by providing an overview of existing scientific literature. First, an analysis of the applications for hydrogen generated by electrolysis is made. The advantages and disadvantages, relevant for different application cases are considered to demonstrate the importance of improving the overall conversion efficiency. Thereafter the electrolyzer technology and working principles are described. Based on the characteristics of the different existing technologies, a specific technology is selected to be further considered in this work. The electrical behavior of this electrolyzer type is examined to provide insight in the output requirements of the designed DC/DC converter.

A study is also conducted into the supply cases of the electrolyzer, highlighting the benefits of directly integrating renewable sources and battery systems. Finally the DC/DC converter systems that most fit the considered applications are researched. Based on the findings in the previous sections, the requirements for the converter are outlined with and a basic topology for this application is selected.

2.2 Applications for Green Hydrogen

As stated in the introduction, the European Union plans to greatly increase the existing electrolyzer capacity, in order to make green hydrogen an essential element of the energy system [1]. The EU's hydrogen energy roadmap [8] defines five sectors in which hydrogen could play an essential role in facilitating Europe's energy transition. These sectors consist of:

- *Renewables and power*: The EU foresees that as a storage and transport medium, hydrogen has the opportunity improve the value of renewable electricity and make it less dependent on the time and location of generation, thus allowing more stability to systems relying mainly on renewable energy.
- *Transport*: Fuel cell electric vehicles are considered by the EU to be the most prominent option for decarbonizing heavy transport vehicles due to the large

energy and power density and fast refueling potential. It is also stated that it might be beneficial to develop large scale hydrogen fueling infrastructure to avoid upgrading the power grid to withstand the strain caused by charging BEVs.

- *Building heating*: For old buildings where it is not feasible to install a heat pump, gas boilers can still provide heat in a carbon-neutral way by integrating hydrogen into the gas grid, either by upgrading the gas infrastructure to transport pure hydrogen or by using synthetic gas made from hydrogen and CO₂.
- *Industry heat*: Whereas electrification is the most efficient substitute for fossil fuels for low- and medium-grade heat. Hydrogen fueled heating systems would be more efficient for high temperature industrial heat. Furthermore, hydrogen as a replacement for conventional fuels allows current heating infrastructure to be retained and avoids upgrades to the electrical transmission system that high temperature electrical heating might require.
- *Industry feedstock*: While most of the current hydrogen demand is used as feedstock in the chemical industry, other sectors may have additional decarbonization opportunities by adjusting their industrial process to rely on clean hydrogen as a feedstock. The largest potential for decarbonization in this way is in the steel industry.

As stated in [8] these points represent the vision of the European Union on the prospects of hydrogen in different energy sectors. In the following subsections, the potential of hydrogen in these sectors is further examined based on scientific literature to generate a clear overview in which applications hydrogen is most important as a means to decarbonization.

2.2.1 Energy storage and transportation

With the increase in variable RES in the electricity system, the demand for electrical storage to compensate over- and underproduction increases. Common storage technologies include batteries for short-term storage with cycle frequencies of once per day or more, while for long-term or seasonal storage pumped hydro plants are most commonly used [9]. To use hydrogen as a medium for electrical storage, electrical power needs to undergo a cycle of electrolysis conversion to hydrogen, compression of the hydrogen and conversion back into electricity by a fuel cell. The cycle efficiency of this process amounts to 33.75% [10]. Compared to battery round trip efficiencies of 90 % [10, 11] and pumped storage efficiency of 75-85%, depending on the reservoir levels [12], hydrogen performs the worst of these storage techniques. It should thus not be a first choice as a technology to store energy. However, pumped hydro storage is constrained by geographical limitations and consequently limited in its further potential [13], as is the same case for CAES as a long term storage technology [14]. Furthermore, although they are very efficient for short-term storage, batteries are

not fit for seasonal storage due to their lifetime degradation, temperature sensitivity, limited energy density and self discharge [14, 15].

Due to these limits in conventional energy storage technologies, hydrogen can in certain cases be considered as a viable technology for long term energy storage. Additional benefits to storing energy in the form of hydrogen include its geographical flexibility, the high power density of electrolyzers and fuel cells and the possibility to use existing gas infrastructure as a storage facility [15–17].

It has been found in [18] that a supply chain based on solar powered hydrogen production in Chile which is then exported to Japan by means of the existing shipping infrastructure can be economically viable. In this way, renewable energy generated in a region with beneficial conditions for solar power is transferred over a large distance which would not be possible with electrical transmission lines. Since the hydrogen is transported by ship, there are CO₂ emissions associated with this form of energy transport. Furthermore, the energy required for shipping might outweigh the benefit of generating the hydrogen in a region with high RES capacity. The viability of this techno-economic case is dependent on the price of hydrogen. It is most likely to succeed if demand for hydrogen is high across different applications and not only as an energy storage medium. For shorter distances relying on hydrogen as a transport medium for energy would not be economically viable as it remains more efficient to transport power in the form of electricity [19]. Therefore, gas infrastructure upgrades for hydrogen transport or international shipping of hydrogen should only be carried out if the end use is other than converting it to electrical power and the value of hydrogen is sufficiently high.

It can thus be concluded that there is potential for hydrogen as a long-term energy storage technology, but due to its limited cycle efficiency, it is less viable for short term storage and energy transport, unless it is in high demand for more valuable applications.

2.2.2 Hydrogen as transport fuel

As an energy source for regular short-distance transport, hydrogen suffers many of the same drawbacks as in its application as a storage technology, namely the low cycle efficiency making it an inferior storage medium to batteries. Furthermore, hydrogen is a very flammable substance, making it very dangerous to carry this around in a vehicle. Fuel cell electric vehicles (FCEVs) therefore need to be subject to strict safety standards, further limiting their economic viability as an alternative to BEVs [10, 20]. Battery electric trucks are becoming more cost competitive, based on the total cost of ownership, due to declining battery costs, but they remain restricted in payload volume and range because of the limited energy density of batteries [21, 22]. FCEVs may be an alternative in this regard, as they provide a higher energy density than batteries [23]. Furthermore, although FCEVs are not cost competitive at this time [10, 24], declining costs provide potential for hydrogen transport to become economically viable [23, 25]. However, the fuel cost for hydrogen vehicles will remain higher than that of BEVs due to the low well-to-wheel efficiency of green hydrogen. Electrification of heavy-duty transport will require considerable charging

infrastructure, both for fuel cell and battery electric trucks. Charging battery electric trucks on the electricity grid is likely to cause issues on the transmission system [22] and thus would require infrastructure upgrades. However, if FCEVs become commonly used, hydrogen fueling infrastructure would have to become widespread, requiring high capital investments as well [10].

It can be concluded that for heavy road transport both battery electrification and FCEVs have their potential and barriers. As battery costs keep declining, battery powered trucks may become more economically viable. However hydrogen powered vehicles may need to be used if the payload or distance becomes too large for a battery vehicle, in which case the required hydrogen fueling infrastructure needs to be available.

Finally, for long distance shipping and aircraft transportation research has been conducted into using hydrogen or hydrogen-based fuels such as ammonia as alternatives to heavy fuel oil and kerosene respectively. Utilization of these fuels can drastically lower the GHG-emissions for these modes of transport but would require significant renewable capacity and increase the fuel cost compared to conventional oil-based fuels [26, 27].

In conclusion, hydrogen can be a valuable resource for transportation, in cases which are not easily operated by a battery system, due to the higher energy and power density of fuel cell systems. The high cost and low cycle efficiency, however, make it an expensive fuel if produced with renewable power. Moving to hydrogen powered vehicles should therefore be carefully considered, as it also comes with high capital infrastructure investments, but it might in some cases be the most viable option for decarbonization.

2.2.3 Heating for buildings

Belgian natural gas consumption amounted to 190.7 TWh in 2020 of which 46.8% was consumed by households and SMEs via the gas distribution grid, as illustrated by Figure 2.1 [28, 29]. Most commonly electrical heat pumps, solar thermal energy and biogas are considered as promising technologies to provide heat to residential and commercial buildings in a carbon free way [30, 31]. The Flemish government supports this view, providing citizens the possibility to receive subsidies from distribution system operator Fluvius for the installation of heat pumps in homes and prohibiting new large residential buildings from connecting to the gas distribution grid, unless the gas is used to supplement a renewable heat source or is used in a CHP application [32]. Plans to further restrict connections to the gas distribution grid are also being discussed, possibly disallowing all new gas connections to residential buildings from 2026 [33].

However, the implementation of heat pumps in existing homes often requires significant renovations, including a change in the heat distribution system [29]. The natural gas system can therefore remain a valuable resource to provide heating in combination with heat pumps to minimize the renovation costs and allow the use of classic radiators [34]. In this way, the gas distribution grid still has an important role

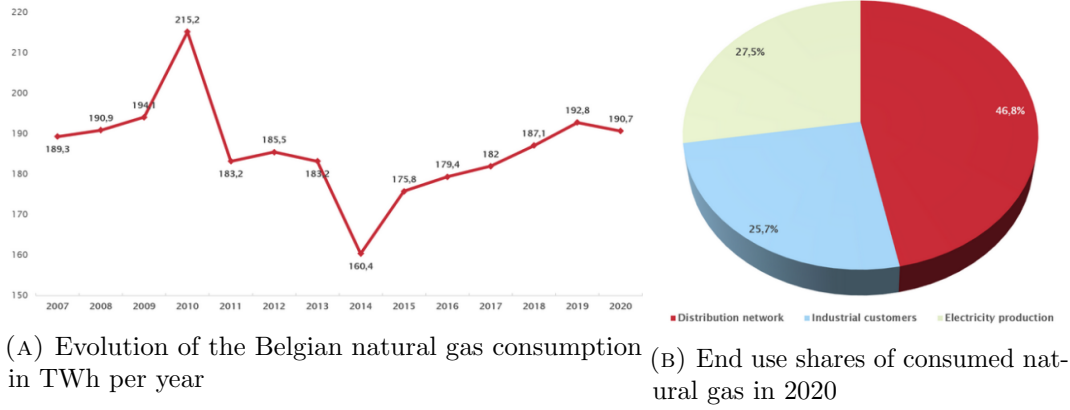


FIGURE 2.1: Belgian natural gas consumption statistics

to play in the foreseeable future, by means of low carbon gasses such as bio-methane, green hydrogen or hydrogen based synthetic methane [29, 35].

To serve as a replacement for natural gas in the gas transmission and distribution grid, an increased flow of hydrogen is required to deliver the same amount of energy, since the HHV of hydrogen is 13 MJ/Nm³ while the HHV of natural gas is approximately 40 MJ/Nm³ [36], meaning that hydrogen molecules contain less energy than natural gas. However, the lower density and viscosity of hydrogen causes it to travel at a higher volumetric flow rate than natural gas at the same pressure. Depending on the flow type (laminar or turbulent) hydrogen thus delivers approximately 40% to 85% of the energy delivered by natural gas at the same pressure [37]. To use hydrogen as the main replacement for natural gas, the existing gas infrastructure and appliances will have to be upgraded to work at a higher pressure and volumetric flow [36, 37].

Alternatively, integrating hydrogen into the gas infrastructure can be done by blending it with natural gas or by using synthetic natural gas based on hydrogen and captured CO₂. A hydrogen concentration of up to 10 vol% can be integrated in the gas supply without needing to upgrade the transport infrastructure. This lowers the heating value and density of the gas supply, thus requiring more compressor power to deliver the same amount of energy by between 8.7% and 13.5%. However, adding hydrogen to the gas supply does lead to a decrease in GHG-emissions at consumption as is shown by Equations 2.1-2.3, demonstrating that less natural gas is used even though the total flow of gas increases [38].

$$(x_{H_2} \cdot LHV_{H_2} + x_{NG}) \cdot LHV_{NG} \cdot \dot{V}_{tot} = LHV_{NG} \cdot \dot{V}_{ref} \quad (2.1)$$

$$\frac{\dot{V}_{tot}}{\dot{V}_{ref}} = \frac{LHV_{NG}}{x_{H_2} \cdot LHV_{H_2} + x_{NG}} = 1.0751 \quad (2.2)$$

$$\frac{\dot{V}_{NG}}{\dot{V}_{ref}} = x_{NG} \cdot 1.0751 = 0.9676 \quad (2.3)$$

With the LHV of H₂ and natural gas taken as 10.8 MJ/Nm³ and 35.8 MJ/Nm³

respectively [39] and a maximum hydrogen fraction of 10%. Through power to gas technologies, the carbon emissions caused by gas consumption can be further reduced. Rising gas prizes increase the economic viability of this technology, which has high capital investment costs for the electrolyzer and methanisation unit. However, since electricity is used as an energy source and the total process has a maximum efficiency of approximately 59% (74% for the electrolyzer and 80% for methanisation) the cost of electricity plays a large role in the final methane price and so, this method is only viable if the value of methane is significantly higher than that of electricity [40, 41].

2.2.4 Hydrogen as industrial heat

In industrial applications high temperature heat demand is a large consumer of fossil fuels. As discussed in the previous subsection, hydrogen and hydrogen-based synthetic methane can provide low-carbon heat. Hydrogen-based ammonia can also be used. The wide range in required temperatures and high temperature applications limit the direct electrification potential such as heating by heat pumps, resistive elements or induction. Although the same efficiency considerations for hydrogen-based energy apply, based on the application hydrogen may be a viable contender to replace fossil fuels to provide industrial heat [42].

2.2.5 Hydrogen as an industry feedstock

In 2020, almost all hydrogen demand was directed towards oil refineries and industrial feedstocks. Of the 90 Mt H₂ consumed in 2020, refineries consumed 40 Mt while 45 Mt was used as a chemical resource for the production of ammonia and methanol. The final 5 Mt were used in the steel industry in DRI processes. Almost all of this hydrogen demand was produced from fossil fuels, resulting in approximately 900 Mt of CO₂ emissions [43]. Consequently, there is a large potential to reduce these emissions by producing more clean hydrogen. The steel industry is responsible for 8% of the global energy use and 7% of global energy related CO₂ emissions [44]. With most of these emissions coming from coal and coke in blast furnaces to reduce oxygen from iron ore, new methods of steel production will be required to lower the industry's carbon footprint. Today, shaft furnace direct reduction electric arc furnaces use natural gas to reduce the ore to direct reduced iron (DRI). Although this is capital intensive, replacing blast furnace ovens with these types of furnaces, which can also be operated with hydrogen instead of natural gas, is a promising way to produce carbon-neutral steel [45, 46]. For this a sufficient supply of clean hydrogen is required. Steel producer ArcelorMittal has integrated DRI steel production as a core element of their goal to be climate neutral by 2050 [43, 45]. As a result, decarbonization of the steel industry and supporting policy may become a main driver in the further development and deployment of electrolyzer based hydrogen production.

The chemical company BASF is focusing its efforts on the development methane pyrolysis technology to produce low-carbon hydrogen. Simultaneously, they are collaborating with Siemens Energy to construct a 50 MW PEM electrolyzer system

[47]. It is clear that, for this industry branch too, producing hydrogen in a clean way is an important step on the path to carbon neutrality.

2.2.6 Conclusion on the applications of hydrogen

Based on the evaluation of the sectors in which the EU's fuel cell and hydrogen joint undertaking sees potential, it should be noted that, although there are many applications in which hydrogen has potential as an energy carrier, it is always a product of electricity if it is produced by electrolysis. Therefore, because of the efficiency losses, the cost of clean hydrogen will always be higher than that of electricity. It can consequently be assumed that hydrogen production is most appropriate when electricity prices are low due to excessive RES production. However, considerations if hydrogen is truly the best energy carrier for a specific application should always be made.

As an industrial feedstock in the steel and chemical industry clean hydrogen is most likely to be in highest demand as it is a necessary resource for chemistry and the only alternative to natural gas in DRI steel production. However, supportive policy and strict emission reduction requirements will be required to make hydrogen based on electrolysis cost competitive. Similarly, if emission restrictions become so strict, that it is no longer possible to use natural gas, and the potential for electrical heating is saturated, hydrogen can become an important medium to provide heat to households and industry. Finally, if in the future the amount of RES will be so high that the cost for flexibility, storage and transmission outweighs the cost of energy itself, hydrogen could serve as a means to provide stability to the system as a means of energy storage.

In conclusion, although its potential is not limitless and depends on many factors such as the availability and cost of renewable electricity, it is clear that clean hydrogen will surely play a role in the future of the energy system and in industry. Its usefulness can be increased by improving the conversion efficiency. This provides the basis for this thesis, which focuses on improving one link in the electrolysis efficiency chain. This conclusion on the viability of the different applications of hydrogen is graphically represented in Figure 2.2.

2.3 Electrolyzer Technology

In an electrolyzer hydrogen is produced by adding electrical energy to water, as represented by Equation 2.4.



This energy is added in the form of a DC current. Protons from the water bond with the supplied electrons to form hydrogen. In room temperature conditions with no additional reactants, the occurrence rate of this process is very small due to the low conductivity of water (10^{-7} mol./l). In electrolyzers, the conductivity is increased

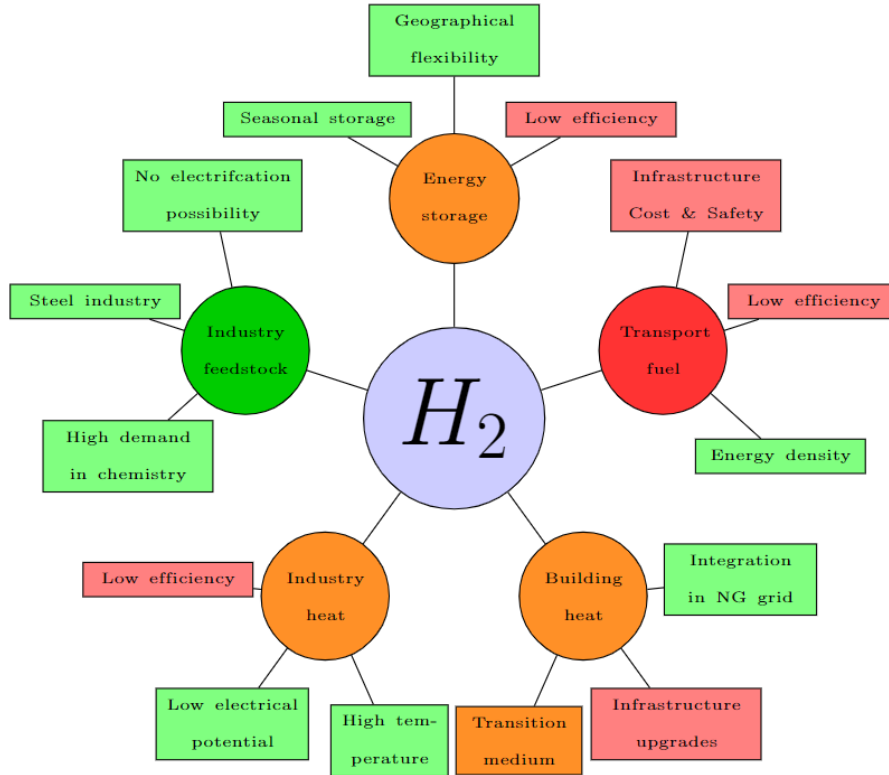


FIGURE 2.2: Representation of the main benefits and disadvantages of the different applications for renewable hydrogen

by adding an electrolyte, which makes the solution split up into ions and improves the reaction rate [48].

Three methods for electrolysis exist. Maturest is the alkaline electrolyzer technology. This type of electrolyzer uses a liquid electrolyte such as KOH, NaOH or less commonly H_2SO_4 . Since this is the most established technology type, alkaline electrolyzers are the cheapest form of electrolyzer. Furthermore, they are already highly commercialized for high power applications and have the longest lifetime out of the current existing electrolyzer types. However, these types of electrolyzers have a slow dynamic response and are not fit to operate at low partial loads. In an electrical system with high generation by RES, this would be an issue since, as discussed in the previous subsection, it would be most beneficial to generate hydrogen at peak generation moments, which might strongly vary throughout the day. Furthermore, long restarting times of 30-60 minutes further limit the flexibility of alkaline electrolyzers in RES based systems [48, 49].

PEM electrolyzers are a newer technology, originating from General Electric's design first published in 1973 [50], making use of a solid sulfonated electrolyte membrane. The electrodes are directly connected to the membrane which has a high permeability for protons. In order to resist the corrosive acidic membrane, the electrodes in a PEM electrolyzer consist of noble metals such as platinum, iridium

and rhodium and their oxides [48, 51]. These materials drive up the cost of PEM electrolyzer cells. Additionally, PEM electrolyzers have a shorter lifetime of 5 to 20 years compared to the expected 15 to 30 years of alkaline electrolyzers [49]. Even though PEM electrolyzers are consequently a more expensive investment choice than their traditional counterpart, their advantages make the technology a viable competitor to alkaline electrolysis [52]. PEM electrolyzers are flexible due to their fast dynamic response and good partial load range, being able to operate at 5% of the nominal load [48]. Furthermore, PEM membranes allow current densities up to 2 A/cm², which makes them compacter than alkaline electrolyzers which are limited to 0.4 A/cm². Finally, PEM electrolyzers are able to operate at lower cell voltages, thus making them more efficient than alkaline electrolyzers [48, 51]. Figure 2.3 depicts a schematic representation of an alkaline electrolyzer and a PEM electrolyzer from [51]. The reactions taking place at either side of the membrane differ as either a hydroxide ion or a proton are used as a charge carrier but they result in the same final reaction to come to the production of hydrogen.

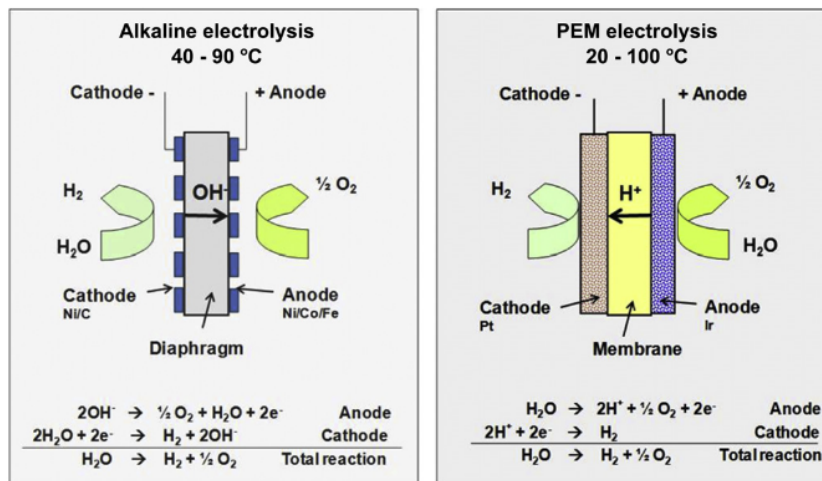


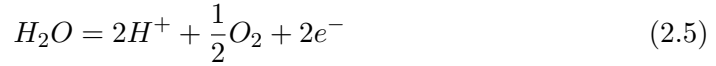
FIGURE 2.3: Schematic representation of alkaline and PEM electrolysis and their governing reactions [51]

The third electrolysis technology is known as solid oxide electrolysis or high temperature electrolysis. This type of electrolyzer operates at temperatures of 500-1000°C [48, 52]. Solid oxide electrolysis uses O²⁻ ions as charge carriers and produces hydrogen from steam. At these high temperatures, a large part of the required energy can be provided by thermal energy, resulting in a high electrical efficiency if the heat is sufficiently available, for example, in the form of waste heat [48, 53]. However, development on solid oxide electrolysis has only started in the late 1970s and was first reported on in [54] in 1980. Technical challenges such as materials degradation form the main remaining barrier to commercialization for this electrolysis technology. Further research into microstructural improvements or the development of new materials is required before solid oxide electrolyzers can be put on the market as an eligible means of producing clean hydrogen [55].

As a result of these considerations, for the remainder of this thesis a PEM electrolyzer is considered. The advantages of PEM technology with regards to dynamic flexibility and partial load range make it the most fit to generate hydrogen in a RES-based electricity system. Furthermore, contrary to high temperature solid oxide electrolyzers, PEM electrolyzers are available on the market. In fact, the **Commercial Electrolyzer** by **Company** is used as a baseline for considerations on the converter design. In that way, any beneficial findings within this thesis are easily transferable to commercial markets.

2.4 Energy Consumption

This thesis aims to improve the process efficiency of generating hydrogen with PEM electrolysis. Therefore, it is important to consider the energy this process requires. As described by Equation 2.4, the reaction of splitting water into hydrogen and oxygen molecules requires the addition of energy in the form of a DC current. The energy required to facilitate a chemical reaction such as this is known as the Gibbs free energy. At standard conditions of temperature and pressure of 298K and 1 atm. respectively, the Gibbs free energy for this reaction amounts to 237.2 kJ/mol [56]. Since this is the minimum energy required to produce one mole of hydrogen it can be converted into a minimum electrolyzer voltage. The anode and cathode equations 2.5-2.6 show that 2 electrons are transferred by the electrical current to produce one hydrogen molecule. Therefore, the hydrogen production rate is dependent on the magnitude of the supplied DC current.



To generate one mole of hydrogen per second, consequently a current magnitude of $2 \cdot F$ is required. Since ΔG represents the minimum energy for this reaction, the minimum cell voltage can be calculated as [48, 51, 52, 56]

$$\begin{aligned} U_{rev} &= \frac{\Delta G}{2F} \\ &= 1.229V \end{aligned} \quad (2.7)$$

However the Gibbs free energy is used to denote the required energy if the reaction occurs reversibly. This is not the case in electrolyzer systems, thus leading to a minimum cell voltage, or open-circuit voltage, dependent on the total enthalpy difference of the reaction as shown in Equation 2.8 [52].

$$\begin{aligned} U_{oc} &= \frac{\Delta H}{2F} \\ &= \frac{\Delta G + T\Delta S}{2F} \end{aligned} \quad (2.8)$$

To avoid reliance on thermodynamic lookup tables, this relation can be empirically represented by the Nernst equation 2.9, with Equation 2.10 accounting for the

temperature dependence of the Gibbs free energy influencing the reversible voltage [51].

$$U_{oc} = U_{rev} + \frac{RT}{2F} \ln \left(\frac{p_{H_2} \cdot p_{O_2}^{1/2}}{p_{H_2O}} \right) \quad (2.9)$$

$$U_{rev} = 1.229 - 0.9 \cdot 10^{-3}(T - 298) \quad (2.10)$$

The open-circuit voltage thus serves as the minimum voltage that must be applied to an electrolyzer to produce hydrogen. Any additional energy supplied to the electrolyzer is not converted into hydrogen molecules and can thus be seen as losses resulting in voltage drops in the electrolyzer. Consequently, the efficiency of an electrolyzer can be expressed by Equation 2.11 [48, 52].

$$\eta_U = \frac{U_{oc}}{U_{tot}} \quad (2.11)$$

The losses occurring in the electrolyzer cause the current to be supplied at a higher voltage than the minimum U_{oc} . These losses consist of ohmic losses due to the membrane and electrode resistance, activation overpotential due to the electrochemical kinetic behavior of the reactants and a diffusion overpotential as a result of the change in concentration of the reactants [51, 57]. The extent of these losses is dependent on the current magnitude and the dimensions of the electrolyzer. Without changing the fundamental principles of the electrolysis technology, these losses can not be avoided. Consequently, the overvoltages dictate the total electrolyzer voltage along with the theoretical open-circuit voltage. The voltage efficiency of the electrolyzer is given by Equation 2.12.

$$\eta_U = \frac{U_{oc}}{U_{oc} + U_{ohm} + U_{act} + U_{con}} \quad (2.12)$$

An increase of the electrolyzer current increases the overvoltages in the cell, resulting in the polarization curve shown in Figure 2.4. The calculation and modeling of this IU-curve is done in Chapter 3. It follows from the IU-characteristics of the electrolyzer cell that operation at a high current density leads to a lower efficiency. However, the hydrogen output is directly proportional to this current. To mitigate the low efficiency at high currents and increase the hydrogen production, multiple cells can be put in series in commercial electrolyzer. This way, the total voltage over a single cell is limited, while all cells are able to produce hydrogen at the same current density. The **Commercial Electrolyzer** has a stack of many cells in series, resulting in a lower voltage per cell while providing significant hydrogen output.

In the calculation of the voltage efficiency it is implicitly assumed that all electrons provided by the DC current bond with protons to form hydrogen atoms, forming 1 mole of hydrogen molecules for every $2F$ or $1.9297 \cdot 10^5$ C of charge applied, according to Faraday's law of decomposition. However, due to gas diffusion and leakage, as well as current behavior, the actual hydrogen production rate is lower than would be expected by this assumption. Thus, this additional leakage of charge causes additional losses since an increased current is required to obtain the desired hydrogen

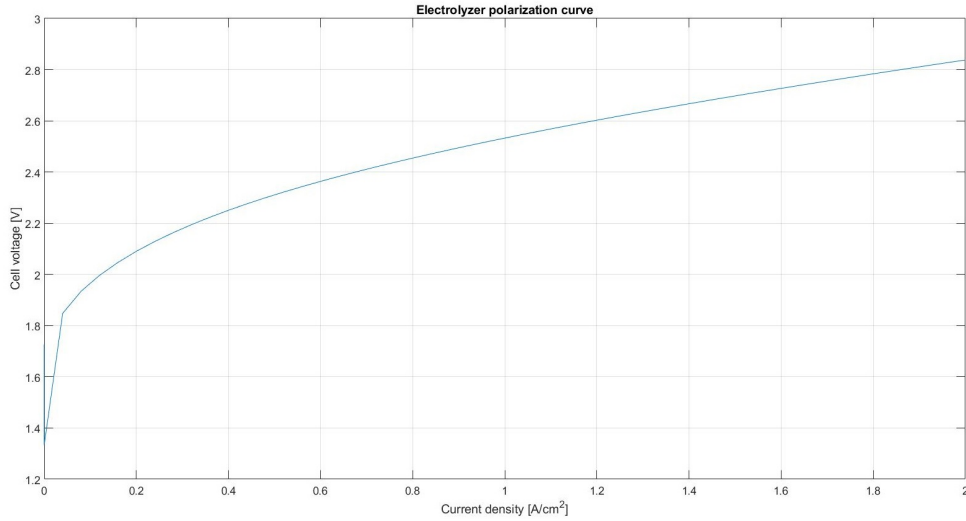


FIGURE 2.4: Polarization curve of electrolyzer cell

output. This current efficiency or faradaic efficiency can be described by Equation 2.13.

$$\eta_F = \frac{2F}{I} \quad (2.13)$$

Resulting in a total electrolyzer efficiency represented by Equation 2.14 [48].

$$\eta_{el} = \eta_U \cdot \eta_F \quad (2.14)$$

For PEM electrolyzers, the faradaic efficiency can be considered to be more than 99% [58–61]. Therefore, it can be neglected in the steady-state modeling of the electrolyzer, as is further done in this thesis.

Research has shown that the waveform of the current has an impact on the efficiency of the electrolyzer. The addition of an AC or triangular ripple to the DC current increases the resistive losses in the electrolyzer, due to an additional RMS current value and deterioration of the electrolyzer materials [62, 63]. Furthermore, it is reported in [64] that the faradaic efficiency of a PEM electrolyzer decreases for an increasing amplitude of the current ripple. These phenomena indicate a decreasing efficiency and lifetime for PEM electrolyzers as an effect of ripple currents, especially at low frequencies [65], as is known to be the case for PEM fuel cells [66, 67]. From this research, it can be concluded that the ripple current amplitude has the highest influence on the electrolyzer efficiency. The ripple frequency shows a less clear effect on the lifetime and performance [62, 64]. Consequently, in this thesis, an effort is made to minimize the amplitude of the ripple current at the output side of the DC/DC converter to increase the total efficiency. Less attention is paid to the effects of the frequency of the current ripple.

2.5 Use Case Analysis

2.5.1 DC grid applications

The purpose of this thesis is to design a converter suited for powering electrolyzers connected to a low voltage DC system. These systems offer significant advantages due to an increase in DC loads and generators in buildings as well as in industry. A direct DC link can be used to draw power from PV generation as well as to provide it to DC loads such as batteries, electronics, LED lighting or variable drive motors. This offers the potential to save energy by reducing power conversion losses [5]. The use of DC microgrids in data centers has been researched in [6], resulting in efficiency improvements between 7% and 28% depending on the original AC voltage. Additionally, advantages such as an increase in safety, reliability and lifetime, as well as decreases in cost, material use and floor space have been reported. In [7] a study into the overall technical and economic benefits of DC microgrids is conducted. This results in the conclusion that the main benefits of DC grids are an increased efficiency, better power quality and a more universal design, leading to lower engineering costs. Aspects such as reliability, protection and resilience are deemed to be case specific and not inherently better for AC or DC grids, although clear advantages can be seen for DC grids in the application in data centers.

The potential to improve the energy efficiency in residential and commercial buildings has been researched in many studies [5, 68–74]. The potential efficiency improvements reported in these studies vary and are often within the range of 2% to 9%. However an increase in PV and battery usage can significantly drive up the efficiency improvements to around 14%-15% as more energy can be directly consumed without undergoing an AC conversion step [5, 69, 70, 75]. Additionally, many loads can still be adapted to more easily allow DC input power and not rely on rectification of AC power within the application itself. An increase in the *DC readiness* of loads has the potential to further significantly increase the energy savings provided by the use of a DC system [69, 70, 76].

DC grids also offer efficiency improvements in industrial applications, allowing more efficient use of renewable generation and storage technologies, necessary to provide a stable power supply [77]. Industrial machines such as CNC machines, production robots or variable drive motors have the potential to work at an increased efficiency, due to the elimination of conversion steps and the possibility to recuperate braking energy by sending it back to the DC bus [78]. The cost effectiveness of using a DC grid in industrial applications is dependent on the scale of the system: the integration of many loads on the DC system further decreases the need for rectifiers but also increases the complexity of the grid and the need for sufficient supply capacity.

2.5.2 Considered modeling cases

The efficiency aspects of local low voltage DC grids offer the potential to efficiently supply electrolyzers of an industrial scale. A converter is therefore designed to

facilitate the connection of the considered **Commercial Electrolyzer** to a DC grid. The operational efficiency of this system is compared to the reference case of an AC supply with an individual rectifier for the electrolyzer, as it is currently produced.

AC reference case

Currently, **Commercial Electrolyzer** models are powered by AC systems at medium voltage (MV). The supplied AC voltage thus needs to be transformed down, after which it is rectified by standard off the shelf rectifier technology. The peak efficiency of this process is reported at 97% by **Company**. Since the exact efficiency characteristic of the transformer and rectifier is not known, this 97% is used as the reference baseline for the performance of the developed DC/DC solutions.

DC microgrid connection

The use of a low voltage DC microgrid is used as the basic power supply option for which a DC/DC converter is designed. The voltage level of this grid is modeled after the EnergyVille Bipolar low-voltage DC lab which contains a bipolar DC grid that can be regulated up to ± 500 V [79]. Therefore, converter tests are conducted at a medium voltage setting of 700 V and the maximum supply voltage of 1000 V. The DC grid is assumed to be a sufficiently strong energy source to power the electrolyzer at its rated power without encountering voltage or power quality problems at the input side. Therefore it is assumed to be connected to a sufficient renewable energy supply and storage facility to support the operation of the considered electrolyzer. Thus in this setup, the only additional losses that need to be considered are the DC/DC converters connected to the solar generation and battery storage modules.

Although a direct coupling to PV and battery systems would be the most efficient implementation, powering the electrolyzer consistently at rated power would require a significant capacity of generation and storage. As long as renewable generation is not overly abundant, it might be more realistic to consider a DC grid which is still (partially) powered from the MV AC grid. This would decrease the efficiency gain since a transformer and rectifier still need to be used. In [80] two rectifiers for DC microgrids are proposed with efficiencies of 96.5%-97%. It is thus unlikely that the use of a DC grid implementation yields significant efficiency improvements compared to the standard operation mode, without the integration of RES to directly provide DC power.

The integration of PV generation provides a clear benefit to the operation of an electrolyzer on a DC grid. For this reason, the application relying on a DC grid powered by the AC system can be considered as a hybrid system, partially powered by local PV generation and by traditional AC power. The amount of power provided by the PV generation influences the total system efficiency. In Chapter 6 the total efficiency as a function of the installed solar capacity is discussed.

Direct solar farm connection

Finally, the application of an electrolyzer fully powered by a 1.7 MW PV farm is considered. In this operation mode, the electrolyzer is only able to provide hydrogen, according to the available PV power. The efficiency of the designed conversion link at varying power setpoints is studied in this way.

The operating conditions set by the PV modules are taken into account through PV generation data from renewables.ninja, an open source platform that collects weather data and converts this into hourly generation data for renewable sources [81–83]. This way, the total efficiency for PV-based hydrogen production in locations with differing solar conditions can be investigated as is done in Chapter 6.

2.6 DC/DC Converter Technology

An electrolyzer cell is operated at a low voltage to minimize the losses. In commercial electrolyzers, many cells are stacked in series to increase the hydrogen output, thus multiplying the total electrolyzer voltage by the amount of serialized cells. However, the final voltages are still lower than the supplying DC networks, resulting in the need for efficient step-down DC/DC conversion at the input side of the electrolyzer.

2.6.1 Operation principle

The standard power electronic circuit for conversion to a lower DC voltage is known as a buck converter [84]. The basic circuit consists of a switch, a diode, an inductor and a capacitor, as depicted in Figure 2.5. The output voltage of this basic converter

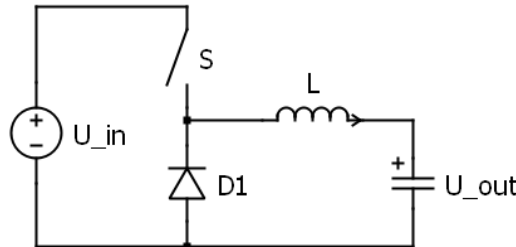


FIGURE 2.5: Basic buck converter circuit

is determined by the switching duty cycle. During the on-state of the switch a positive voltage $U_{in} - U_o$ is applied over the inductor, causing the output current to linearly increase. During the off-state, the voltage over the inductor becomes negative. The current is discharged from the inductor and cycled through the diode. This results in a triangular current which is filtered by output capacitor, resulting in an output DC voltage given by Equation 2.15 [84].

$$U_o = D \cdot U_{in} \quad (2.15)$$

To reach low output voltages with a standard buck converter, a low switching duty cycle is required. However too long off-times may lead to the inductor fully discharging

and the output current temporarily reaching zero every cycle. This operational mode is known as discontinuous conduction mode (DCM) and is undesirable in many applications where a steady DC current is required [84]. The output current of a buck converter in continuous conduction mode (CCM) and DCM is shown in Figures 2.6a and 2.6b respectively.

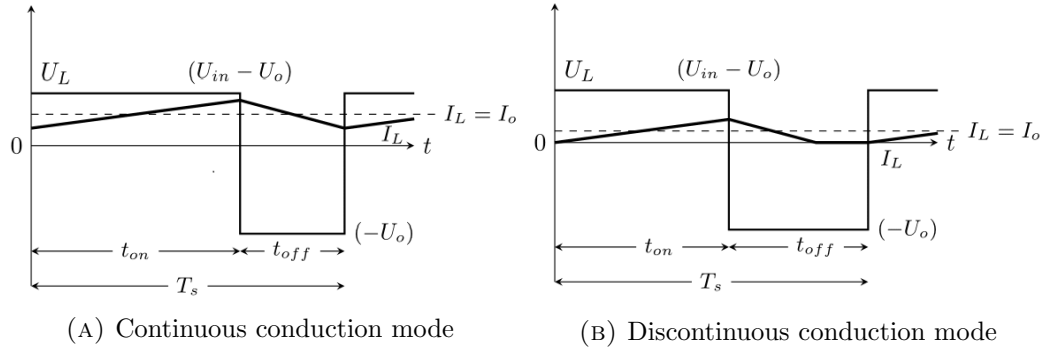


FIGURE 2.6: Buck converter output current behavior for a single cycle

The efficiency of a standard buck converter is dependent on the performance of the used components. Losses resulting from the non-ideal behavior of the components cause power to be dissipated within the converter. Conduction losses due to parasitic resistances occur in every component. Additionally, switching and reverse conduction losses occur in the switch and diode. The switching losses occur due to increased dissipation in the transistor during switching. The diode experiences reverse recovery losses, every time it is switched back into blocking mode. These losses are dependent on the switching frequency of the converter and the inherent switching time characteristics of the components [84]. Additionally, the transistor switching losses can be mitigated by implementing a soft switching circuit that switches either at zero voltage or current. Limiting the losses at the cost of requiring additional components to be integrated increasing the total cost and complexity of the control [85]. Wide-bandgap semiconductors based on silicon carbide and gallium nitride offer a way to further increase the efficiency of a converter. Semiconductors based on these materials achieve lower losses than traditional Silicon based materials [86, 87]. Due to the lower inherent switching and reverse recovery losses, integration of these wide-bandgap semiconductors reduces the need for soft switching circuits in converters [88].

2.6.2 Converter requirements

The standard buck converter offers a simple way to convert DC power to a lower voltage. However, its DCM behavior makes it unfit to work at low output voltages. Additionally, the small amount of components in the topology experience significant voltage and current stress. Several alternate converter topologies improve upon the basic buck converter circuit, by improving the performance at low duty cycles, decreasing the component stress or increasing the efficiency. In [88] an overview is

made of converter topologies fit for electrolyzer systems. The key features considered essential for electrolysis are energy and power density, low interference, cost and ripple, a high conversion ratio, thus being able to reach low output voltages, and a high reliability. In the choice of the specific electrolyzer, these requirements can be further defined: the choice to work with an electrolyzer consisting of many¹ serialized cells limits the importance of the conversion ratio. It becomes more important that the converter is able to supply the required power, thus putting more emphasis on the power density and reliability of the converter. In this thesis mainly the power capacity of the converter is considered. Requirements on reliability and safety, for example by using redundant components or galvanic isolation, are left for further research.

2.6.3 Interleaved converters

A topology with good prospects for high power density operation is the interleaved buck converter (IBC) as depicted in Figure 2.7. This converter consists of N parallel buck converters, with N between 2 and 6. The current through the components is therefore divided by N , reducing the current stress on the components and making it possible to supply the converter at high power. Furthermore, this converter topology offers the benefit that it is able to partially operate in case of a component failure in one of the phases [88]. The controlling signals are shifted by $\frac{1}{f \cdot N}$ seconds between the different legs. This leads to a reduction of the total output current ripple but at an increased frequency. Research has shown that interleaved converter topologies are highly attractive for fuel cell applications, in this case being used in boost mode [86, 89–91]. The aspects that make interleaved converter popular for fuel cell research, such as the power density and the low current ripple, also make it interesting technology for electrolyzer applications.

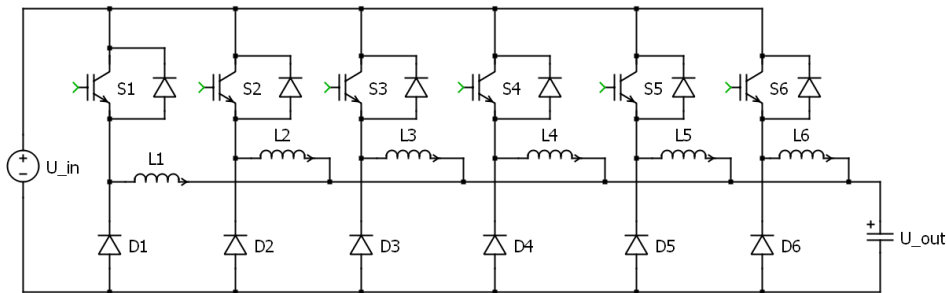


FIGURE 2.7: Basic circuit model of a 6-phase IBC

Since an IBC consists of several basic buck topologies connected in parallel to a common input and output DC bus, the conversion ratio behaves the same as for a single buck converter, being equal to the duty cycle. Consequently, issues with DCM equally limit the conversion ratio of interleaved converters and may even be increased as each inductor bears a lower current compared to a standard buck operation.

¹The exact number is not disclosed at the request of **Company**

However, adjustments can be made to the basic circuit to improve the range of the conversion ratio, possibly also leading to efficiency improvements [92–96]. For example, [93] proposes an improved version of a standard 2-phase IBC by connecting two active switches in series and adding a coupling capacitor as shown in Figure 2.8.

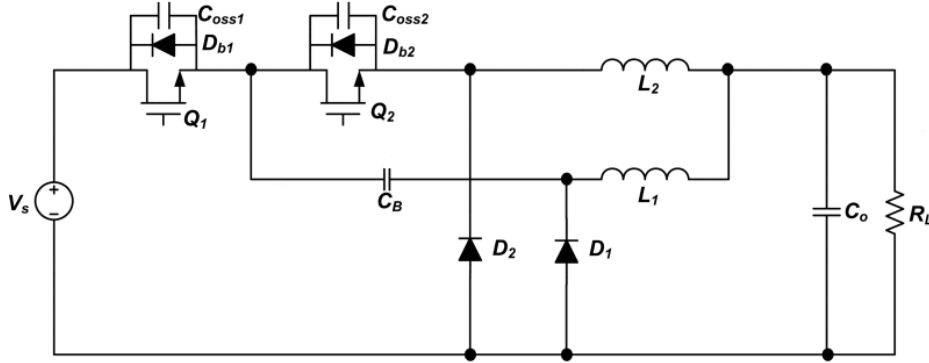


FIGURE 2.8: Improved IBC proposed in [93]

The conversion ratio behavior for this converter is given by Equations 2.16 and 2.17 for $D < 0.5$ and $D > 0.5$ respectively.

$$R = \frac{D}{2} \quad (2.16)$$

$$R = D^2 \quad (2.17)$$

This converter is thus able to reach lower output voltages with relatively higher duty cycles, compared to a normal IBC, especially in the range below duty cycles of 0.5. Furthermore, due to the improved voltage waveform in this converter, the switching and capacitor losses are significantly reduced, compensating for the increase in switch conduction losses due to the operation at a higher duty cycle. The loss analysis from [93], which is shown in Figure 2.9, indicates that this converter offers significant efficiency improvements compared to the standard IBC.

2.6.4 Isolated converters

Aside from the IBC, other converter topologies have the potential to be useful for PEM electrolysis. Isolated topologies utilize a transformer at high frequency. This transformer can be used to achieve a step-up or step-down ratio, independent of the switching duty cycle. The converter consists of an inverter circuit, the isolated transformer, a rectifying circuit and an output filter. Due to the ability to use a transformer, the voltage ratio is less dependent on the duty cycle, allowing the components to be dimensioned for an optimal duty cycle with low current or voltage stress. Furthermore, there is no risk of operating in DCM since a low output voltage can be achieved without operating at very low duty cycles. However, the voltage ratio of the transformer is limited by the leakage inductance that increases along with the turn ratio, leading to additional losses [88].

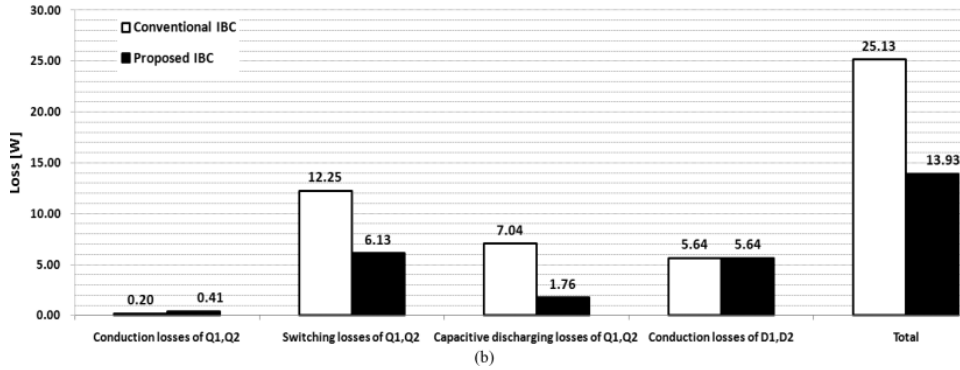


FIGURE 2.9: Loss analysis for the improved IBC from [93] for $D < 0.5$ at switching frequency of 300 kHz and 240 W output power

Isolated converters can be realized with half-bridge and full-bridge topologies. A basic circuit for these topologies is depicted in Figure 2.10. In [97] a half-bridge converter (HBC) for electrolysis is introduced. This converter uses a phase-shifted synchronous active rectifier at the output side, controlled to minimize circulating currents to minimize the losses. It is reported that this type of converter is promising for electrolysis applications due to a high conversion ratio and low switching and conduction losses, resulting in a high efficiency. However, the use of only few components limits the potential for use at high power and lowers the reliability.

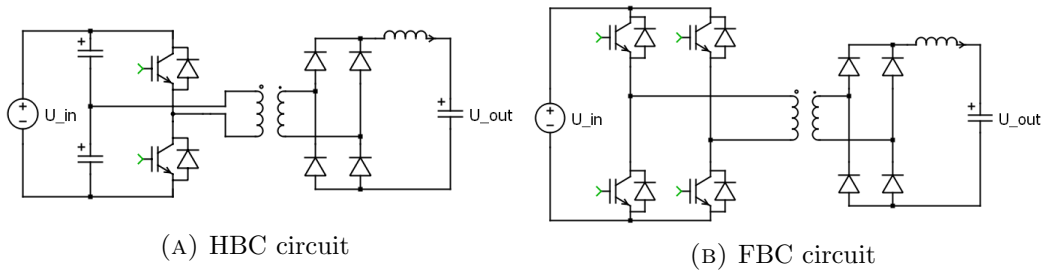


FIGURE 2.10: Isolated DC/DC converter topologies

Full-bridge topologies are also proposed for electrolysis applications [98, 99]. A higher amount of components on the inverter side leads to additional switching and conduction losses and increased cost but offers a higher power capacity than a HBC. [100] introduces a three-phase full-bridge converter (FBC) using three parallel single-phase AC transformer, thus further improving the power capacity of the converter. The design is depicted in Figure 2.11.

The voltage conversion ratios of a standard FBC and HBC are given by Equation 2.18 and 2.19 respectively [84], with the transformer ratio N_t defined by the number of input windings divided by the output windings.

$$R_{FB} = 2 \cdot \frac{D}{N_t} \quad (2.18)$$

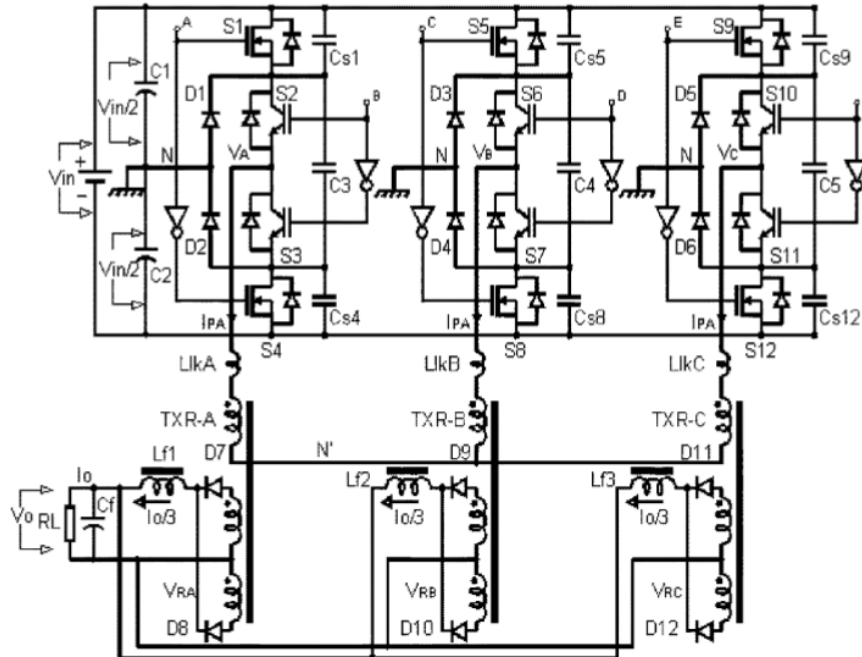


FIGURE 2.11: Three phase FBC proposed in [100] for high power applications

$$R_{HB} = \frac{D}{N_t} \quad (2.19)$$

Due to the ability of the HBC to operate at the midpoint of the DC input voltage, it is able to reach lower voltages than FBC implementations. This leads to the conclusion that, of the two isolated topologies, HBCs are most suitable for small electrolyzer stacks operating at low power and voltage, while FBCs are more fit to deal with the high power required by large electrolyzers with many cells in series.

2.6.5 Other topologies

The IBCs and isolated converters described above are promising converter topologies. However, they are not the only possible converter implementations that can be used for electrolyzer operation. Converters such as the quadratic converter, tapped-inductor converter or the switched capacitor/inductor converter are described in [88] and are able to reach lower voltages than the standard buck converter. However, many of these converters use few components limiting their reliability and power capacity.

2.7 Conclusion

In this literature study, the main motivations and concerns for the considered application are given, as well as an overview of the principles that need to be understood to provide an answer to the research questions. Section 2.2 provides a

critical overview of the future applications for hydrogen and its role in the energy system. This section demonstrates that hydrogen is inevitably going to play a role in the future energy system, although it is not without its drawbacks depending on the application. These drawbacks underline the importance of being able to produce hydrogen in a clean and efficient way.

The electrolyzer producing the hydrogen is described in Section 2.3. Although improving the principles governing this process is out of the scope of this thesis, understanding them is essential to know what is required of the converter transferring the energy at the correct voltage. Sections 2.3 and 2.4 provide the basic principles and energetic behavior required to model the electrolyzer in Chapter 3, which can then be used to model the output side when designing the DC/DC converter.

Section 2.5 outlines the different applications for which it would be beneficial to implement an efficient DC/DC converter. This provides the basis for the different input-side conditions for which the designed electrolyzer model is evaluated in later chapters. Furthermore, it provides a reference in the form of the conventional rectifier case from the **Commercial Electrolyzer**, which serves as a baseline upon which this thesis aims to improve. It is found that DC grids with a direct connection to PV and battery systems offer the potential for significant efficiency improvements. Case studies taking the behavior of the solar generation into account will quantify these benefits in later chapters.

Finally, Section 2.6 gives an overview of the converter technologies that are most optimal for the considered applications. The IBC and isolated FBCs show the best prospects for the considered high power electrolyzers. These topologies will be considered in Chapter 4 as a starting point for the design of an efficient DC/DC converter.

Chapter 3

Electrolyzer Modeling

3.1 Introduction

This Chapter discusses the models and calculations used to represent the electrolyzer in this thesis. The polarization curve of an electrolyzer is nonlinear. Therefore, it is important to know the correct voltage to supply in order to get the right amount of hydrogen output. The mechanisms that determine the IU-curve of the electrolyzer are the open-circuit voltage and the overvoltages resulting from the losses in the electrolyzer. These voltages are dependent on many factors, including environmental factors, dimensions of the electrolyzer and the supplied power. Sections 3.2-3.3 describe the calculation of these losses, as well as the governing internal mechanisms, and handle the construction of a Simulink model to calculate the voltage-current behavior across the operating range.

In Section 3.4, the investigated models are applied to the considered commercial electrolyzer. The specific data of the electrolyzer required to achieve accurate IU-setpoints is integrated in the model to achieve a system that represents the behavior of the electrolyzer at the output-side of the DC/DC converter.

Section 3.5 then considers how this behavior can be modeled with simple electrical components, to simulate its characteristics in PLECS, where the DC/DC converter is modeled. The applied models are only considered for steady-state operation of the electrolyzer. Section 3.5 discusses models from [101, 102] that are constructed based on tested dynamic behavior, but since these dynamics are out of the scope of this thesis, the models are simplified and applied for steady-state.

3.2 Voltage Calculation

The required supply voltage of a PEM electrolyzer consists of four components: the open-circuit, activation, ohmic and concentration voltages.

$$U_{el} = U_{oc} + U_{act} + U_{ohm} + U_{con} \quad (3.1)$$

The losses causing these overpotentials, as well as the minimum open-circuit voltage, are dependent on physical interactions occurring within the electrolyzer. Therefore,

the magnitude of the voltages can be calculated by means of the physical equations describing these electrochemical interactions. The approach and equations described in this section are often used in literature, functioning as the main way of calculating the voltage characteristic of a PEM electrolyzer. The model used in this thesis is mainly based on [57] with a similar approach described in [61, 103–108].

3.2.1 Open-circuit voltage

As discussed in Section 2.4 the open-circuit voltage is dependent on the total enthalpy of the electrolysis reaction. It is empirically described by the Nernst equation. The Nernst equation and the temperature dependence are given in Equations 2.9 and 2.10 but are repeated here for convenience.

$$U_{oc} = U_{rev} + \frac{RT}{2F} \ln \left(\frac{p_{H_2} \cdot p_{O_2}^{1/2}}{p_{H_2O}} \right) \quad (3.2)$$

$$U_{rev} = 1.229 - 0.9 \cdot 10^{-3} (T - 298) \quad (3.3)$$

The open-circuit voltage is thus only dependent on the operating temperature and the partial pressures of hydrogen, oxygen and water. These pressures are determined by the transport phenomena in the anode, cathode and membrane described in Section 3.3.

3.2.2 Activation voltage

The electrochemical kinetic behavior of the charge transfer reaction at the electrodes causes an activation overpotential, which can be described by the Butler-Volmer equation [57, 104]. Equation 3.4 shows the Butler-Volmer equation resulting in an activation overvoltage for both the anode and cathode side of the electrolyzer.

$$U_{act} = \frac{RT}{\alpha_{an}F} \operatorname{arcsinh} \left(\frac{i}{2i_{o,an}} \right) + \frac{RT}{\alpha_{cat}F} \operatorname{arcsinh} \left(\frac{i}{2i_{o,cat}} \right) \quad (3.4)$$

With α and i_o the charge transfer coefficient and the exchange current density respectively. These parameters are fitted to the model in [57]. The assumed values for these parameters, as well as the other estimated quantities in this thesis, are listed in Table 3.1. Equation 3.4 shows that if these values are known, the activation voltage is only dependent on the temperature and the applied current density. These parameters are known and assumed to be uniform and constant for the considered model,

3.2.3 Ohmic voltage

The ohmic voltage drop is a result of the resistive losses in the electrolyzer, According to Ohm's law, this resistive voltage drop amounts to

$$U_{ohm} = R_{ohm} \cdot I \quad (3.5)$$

To know this voltage drop, the total resistance of the electrolyzer needs to be modeled. This resistance can be separated into a resistance for the anode, the cathode and the membrane [103]. The anode and cathode resistance can be further split up into the resistance of the electrode and the bipolar plates. These plates are located between the electrode and the membrane and contain channels through which the reactants are brought into contact with the applied electrical charge [57, 103]. These components can be modeled together as a network of resistances as is done in [103], resulting in the network depicted in Figure 3.1. This network can then be simplified to a resistive model around each channel, as shown in the network in Figure 3.2 [57].

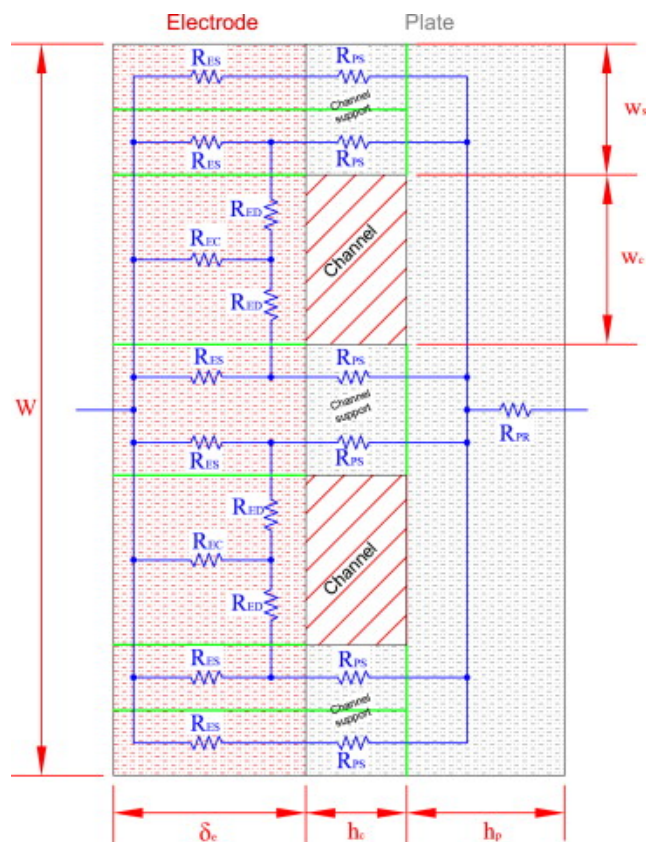


FIGURE 3.1: Resistance model of the electrode and plate

The simplified resistances in the network from Figure 3.2 can be calculated by multiplying the material resistivity of the electrode and the plate with the length of the resistive path and dividing by the cross section area through which the current passes, resulting in Equations 3.6-3.8 representing the total electrode, channel and

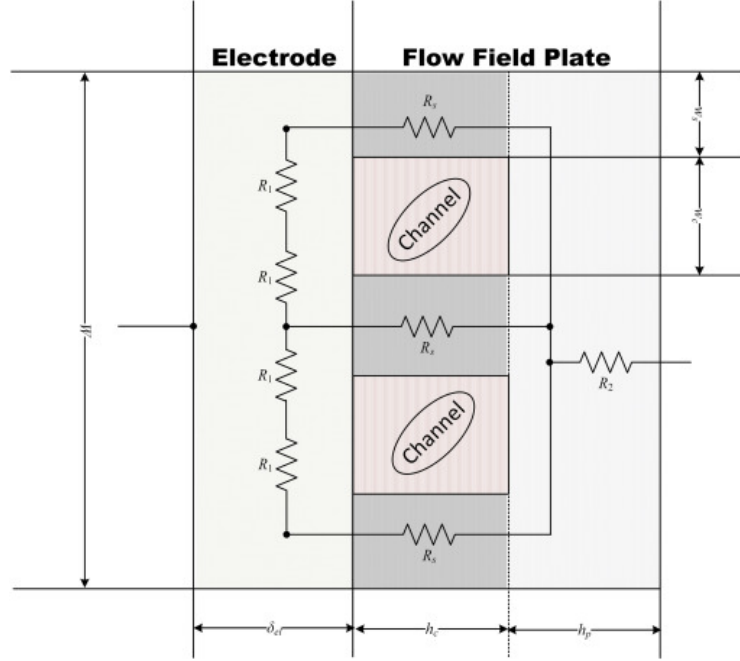


FIGURE 3.2: Simplified resistive circuit model for electrode and bipolar flow plate resistance.

$$R_{el} = \frac{\rho_{eff} \cdot (w_c + w_s)}{8H \cdot n_{ch} \cdot \delta_{el}} \quad (3.6)$$

$$R_{s,tot} = \frac{\rho_p \cdot h_c}{n_{ch}^s \cdot w_s^{an} \cdot H} \quad (3.7)$$

$$R_2 = \frac{\rho_p \cdot h_p}{W \cdot H} \quad (3.8)$$

The number of channels and channel support structures n_{ch} and n_{ch}^s determine the amount of parallel resistances. δ_{el} , h_c , h_p , w_s and w_c denote the internal sizes and lengths of the current paths within the anode or the cathode, while W and H represent the total width and length of the MEA, as is shown by Figures 3.1 and 3.2 [57, 103].

The electrode and plate resistances occur at either side of the membrane. The resistance of the membrane itself is given by Equation 3.9

$$R_{mem} = \frac{\delta_{mem}}{A \cdot \sigma_{mem}} \quad (3.9)$$

The conductivity σ_{mem} is given by Equation 3.10, with λ a measure for the humidity of the membrane, being expressed as the ratio of water molecules to H_2SO_4 molecules [57, 103].

$$\sigma_{mem} = (0.005139\lambda - 0.00326) \cdot \exp\left(1268 \left(\frac{1}{303} - \frac{1}{T}\right)\right) \quad (3.10)$$

Equations 3.6-3.10 allow the total electrolyzer resistance to be described as

$$R_{ohm} = R_{el}^{an} + R_{el}^{cat} + R_s^{an} + R_s^{cat} + R_p^{an} + R_p^{cat} + R_{mem} \quad (3.11)$$

These equations show that the resistive voltage drop is highly dependent on many structural and geometrical properties of the MEA. It is firstly assumed that for the anode and cathode side, the geometrical parameters are equal. Secondly, the effective resistivity of the electrodes ρ_{eff} can be further expressed as Equation 3.12, where ϵ is the electrode porosity [57].

$$\rho_{eff} = \frac{\rho_{el}}{(1 - \epsilon)^{1.5}} \quad (3.12)$$

The values in this equation, as well as the internal dimensions of the electrolyzer cell are estimated based on values given in [57] as well as figures provided in [103]. W can be derived from the known cell area A , if H is set as the average channel length, as discussed in [103] and shown by Figure 3.3, which results in H being given by Equation 3.13. The cell radius r also depends on the known surface area A .

$$H = H_{av} = \frac{2}{n_{ch}} \sum_{j=1}^{n_{ch}/2} \sqrt{r_{MEA}^2 - \left(j - \frac{1}{2}\right)^2 \cdot (w_c + w_s)^2} \quad (3.13)$$

Furthermore, Figure 3.3 shows that if the number of channels is chosen, the widths of the channels and the supports can be determined. In this case it was chosen to assume w_s and w_{ch} to be equal. The remaining values that must be assumed to come to a result for the electrolyzer resistance are listed in Table 3.1.

3.2.4 Concentration voltage

The final voltage component contributing to the total electrolyzer voltage is the concentration overpotential. This voltage component is the result of the changing concentration of the reactants within the electrolyzer. It increases with high currents, when the reaction rate is hindered by a high concentration of oxygen and hydrogen at the membrane surface [57, 109]. The magnitude of the concentration voltage is based on the concentration hydrogen and oxygen compared to a reference working point¹, as shown in Equations 3.14-3.16.

$$U_{con} = U_{con}^{an} + U_{con}^{cat} \quad (3.14)$$

$$U_{con}^{an} = \frac{RT}{4F} \ln \left(\frac{C_{O_2}^{mem}}{C_{O_2,0}^{mem}} \right) \quad (3.15)$$

$$U_{con}^{cat} = \frac{RT}{2F} \ln \left(\frac{C_{H_2}^{mem}}{C_{H_2,0}^{mem}} \right) \quad (3.16)$$

¹This reference is taken as the nominal operating point, leading to a U_{con} of zero at nominal power. Since the concentration of the reactants causing this overvoltage is decreasing for lower currents, U_{con} will be negative for operating points below the nominal operation. The variations in efficiency based on the selected working point of the electrolyzer are unchanged by this decision.

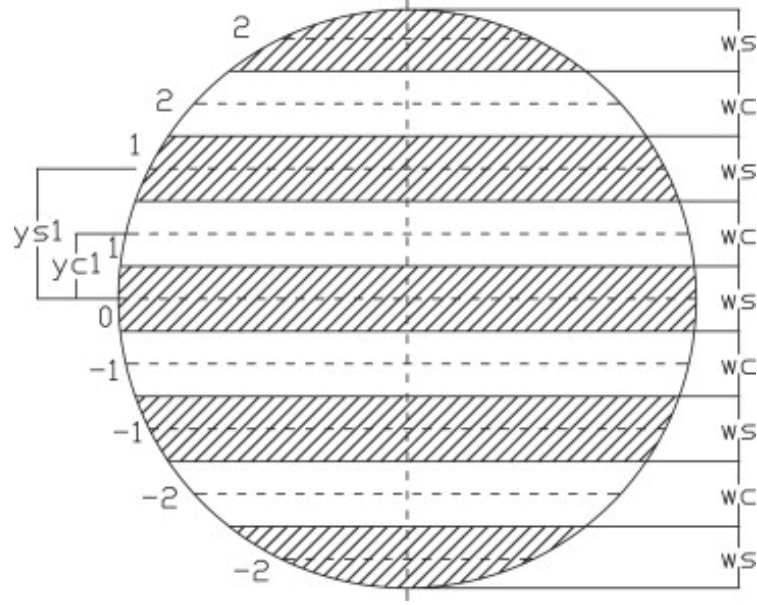


FIGURE 3.3: Representation of the bipolar plate consisting of channels and support structures, n_{ch} is chosen based on this figure and H is set equal to the average channel length [103]

Similarly to the partial pressures required in the calculation of the open-circuit voltage, the concentration values are determined by the transport phenomena taking place in the electrolyzer cell. In this case, diffusion of the reactants plays a large role relating the concentration at the membrane to the channel concentration by Equations 3.17 and 3.18, wherein the molar concentration of hydrogen and oxygen in the plate channels can be written as Equations 3.19 and 3.20 according to the ideal gas law [57].

$$C_{O_2}^{mem} = C_{O_2}^{ch} + \frac{\delta_{el}^{an} \cdot n_{O_2}}{D_{eff}^{an}} \quad (3.17)$$

$$C_{H_2}^{mem} = C_{H_2}^{ch} + \frac{\delta_{el}^{cat} \cdot n_{H_2}}{D_{eff}^{cat}} \quad (3.18)$$

$$C_{O_2}^{ch} = \frac{p_{an} \cdot X_{O_2}}{RT} \quad (3.19)$$

$$C_{H_2}^{ch} = \frac{p_{cat} \cdot X_{H_2}}{RT} \quad (3.20)$$

The molar fractions X_{H_2} and X_{O_2} and molar flux n_{H_2} and n_{O_2} can be calculated by further studying the transport mechanisms in the anode, cathode and membrane. These can be seen as subsystems influencing each other and determining the calculation of the final electrolyzer voltage. The electrolyzer can therefore be described as a Simulink model consisting of these four subsystems. Consequently, the applied current, as well as several other parameters related to the ambient conditions and electrolyzer size, can be used as inputs to calculate the required electrolyzer voltage,

coming to the construction of IU-curves. The developed Simulink model is based on [57, 104] and is depicted in Figure 3.4.

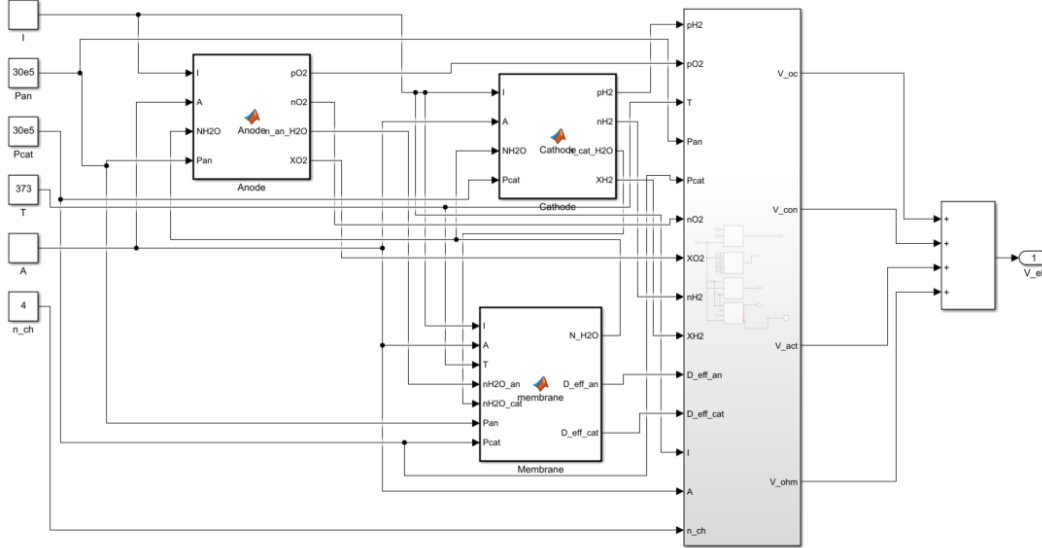


FIGURE 3.4: Simulink model calculating the voltage of the electrolyzer based on the mass transport mechanisms in the anode, cathode and membrane, dependent on the input current and pressures

3.3 Transport Mechanisms

This section elaborates on the Anode, cathode and membrane mass transport phenomena, which have an impact on the magnitude of U_{oc} and U_{con} . The open-circuit voltage is determined by the partial pressures at the anode and cathode. The concentration voltage is dependent on the molar fraction and flux of hydrogen and oxygen, as well as the effective diffusion coefficient at both sides of the electrolyzer.

3.3.1 Diffusion coefficient

The effective diffusion coefficient D_{eff} stems from Fick's law of diffusion, given by Equation 3.21. This coefficient determines the rate in which substances are transported along the concentration gradient to the area with a lower concentration [57, 110].

$$J = -D_{eff} \left(\frac{\partial C_i}{\partial x} \right) \quad (3.21)$$

The diffusion coefficient varies for the different reactants in different media. In porous materials such as the anode and cathode structures, the diffusion is dependent on the molecule-molecule interaction for structures with large pores and on the molecule-wall interaction for small-pored structures. These diffusion mechanisms are known as the

TABLE 3.1: Assumed values for unknown parameters in the electrolyzer model

Parameter	Value
α_{an}	0.8
α_{cat}	0.25
$i_{0,an}$	$1 \cdot 10^{-7}$ A/cm ²
$i_{0,cat}$	0.1 A/cm ²
δ_{el}	0.008 cm
δ_{mem}	0.0254 cm
n_{ch}	4
ρ_p^{an}	$43.1 \cdot 10^{-6}$ Ω cm
ρ_p^{cat}	$16.0 \cdot 10^{-3}$ Ω cm
ρ_{el}	$10.6 \cdot 10^{-6}$ Ω cm
ϵ	0.3
λ	21
ξ	4
r_p	1 μ m
ρ_{H_2O}	1000 kg/m ³
D_w	$1.28 \cdot 10^{-6}$ cm ² /s
n_d	7
K_{darcy}	$1.58 \cdot 10^{-14}$ cm ²
μ_{H_2O}	1.1 g/m s

molecular and Knudsen diffusion respectively. The diffusion coefficient for these two mechanisms is calculated differently and can be combined into the effective diffusion constant as given by Equations 3.22-3.23. ξ represents the ratio of the tortuosity² to the porosity³ [57, 112, 113].

$$D_{eff}^{an} = \frac{\xi}{\epsilon} \left(\frac{1}{D_{eff}^{O_2-H_2O}} + \frac{1}{D_{eff}^{H_2O,K}} \right) \quad (3.22)$$

$$D_{eff}^{cat} = \frac{\xi}{\epsilon} \left(\frac{1}{D_{eff}^{H_2-H_2O}} + \frac{1}{D_{eff}^{H_2O,K}} \right) \quad (3.23)$$

The Knudsen diffusion coefficient can be calculated by Equation 3.24 [57, 112–114], with r_p the average pore radius.

$$D_{eff}^{H_2O,K} = \frac{4}{3} r_p \sqrt{\frac{8RT}{\pi \cdot M_{H_2O}}} \quad (3.24)$$

²“Tortuosity is defined as the ratio of the lengths of the preferential tortuous fluid pathways and the porous media” [111], thus representing the actual traveled distance within a porous medium, compared to the minimum path length

³“Porosity is a scalar measure of the pore volume defined as the volume fraction of the pore space in the bulk of porous media” [111]

The diffusivity for molecular interactions is given by Equations 3.25- 3.26 [57, 113].

$$D_{eff}^{O_2-H_2O} = 0.00133 \left(\frac{1}{M_{O_2}} + \frac{1}{M_{H_2O}} \right)^{1/2} \cdot \frac{T^{3/2}}{p_{an} \cdot \sigma_{O_2-H_2O}^2 \cdot \Omega_D} \quad (3.25)$$

$$D_{eff}^{H_2-H_2O} = 0.00133 \left(\frac{1}{M_{H_2}} + \frac{1}{M_{H_2O}} \right)^{1/2} \cdot \frac{T^{3/2}}{p_{cat} \cdot \sigma_{H_2-H_2O}^2 \cdot \Omega_D} \quad (3.26)$$

With Ω_D and σ respectively the diffusion collision integral and the molecular radii. Based on [113], the molecular radii are calculated to be

$$\sigma_{O_2-H_2O} = 3.054 \cdot 10^{-10} \text{ m} \quad (3.27)$$

$$\sigma_{H_2-H_2O} = 2.734 \cdot 10^{-10} \text{ m} \quad (3.28)$$

Ω_D is calculated as [113]

$$\Omega_D = \frac{1.06}{\tau^{0.156}} + \frac{0.193}{\exp(0.476\tau)} + \frac{1.036}{\exp(1.53\tau)} + \frac{1.765}{3.894\tau} \quad (3.29)$$

with τ the dimensionless temperature given by Equations 3.30-3.31 in which the Lennard-Jones potentials ϵ_{O_2} , ϵ_{H_2} and ϵ_{H_2O} amount to 106.7 K, 59.7 K and 809.1 K respectively [57, 113].

$$\tau_{O_2-H_2O} = \frac{T}{\sqrt{\epsilon_{O_2} \cdot \epsilon_{H_2O}}} \quad (3.30)$$

$$\tau_{H_2-H_2O} = \frac{T}{\sqrt{\epsilon_{H_2} \cdot \epsilon_{H_2O}}} \quad (3.31)$$

With these consideration to the diffusion behavior of the reactants in the electrolyzer, it can be concluded that the effective diffusion constant remains only dependent on the temperature and pressure at the anode and cathode, which are assumed as uniform input parameters. For the porosity ϵ and tortuosity ξ the values provided in [57] are assumed. The average pore radius of the electrolyzer materials is estimated to be 1 μm .

3.3.2 Molecular concentration

With the diffusion coefficient known, it is still necessary to know the concentration gradient and partial pressures to calculate the required voltages. From Equations 3.17-3.20 it can be seen that the concentrations of O_2 and H_2 at the membrane are dependent on the molar fraction and flux of these reactants at the anode and cathode respectively.

The molar fluxes of hydrogen, oxygen and water are related to the molar flow rates by Equation 3.32.

$$n_i = \frac{\dot{N}_i}{A} \quad (3.32)$$

These flow rates can be derived from the material balances at the anode and cathode, given by Equations 3.33-3.34 for the cathode and Equations 3.35-3.36 at the anode [57].

$$\frac{dN_{O_2}}{dt} = \dot{N}_{O_2}^{in} - \dot{N}_{O_2}^{out} + \dot{N}_{O_2}^{gen} \quad (3.33)$$

$$\frac{dN_{H_2O}^{cat}}{dt} = \dot{N}_{H_2O}^{in} - \dot{N}_{H_2O}^{out} - \dot{N}_{H_2O}^{mem} - \dot{N}_{H_2O}^{cons} \quad (3.34)$$

$$\frac{dN_{H_2}}{dt} = \dot{N}_{H_2}^{in} - \dot{N}_{H_2}^{out} + \dot{N}_{H_2}^{gen} \quad (3.35)$$

$$\frac{dN_{H_2O}^{an}}{dt} = \dot{N}_{H_2O}^{in} - \dot{N}_{H_2O}^{out} + \dot{N}_{H_2O}^{mem} \quad (3.36)$$

Since the electrolyzer is modeled in steady-state, the derivatives in these equations become zero, meaning that the in- and outflow of water, oxygen and hydrogen in the electrolyzer, exactly matches the generation, consumption and internal flows in the electrolyzer. This leads to the molar fluxes at the anode and cathode being expressed as

$$n_{O_2} = \frac{\dot{N}_{O_2}^{gen}}{A} \quad (3.37)$$

$$n_{H_2O}^{an} = \frac{\dot{N}_{H_2O}^{mem} + \dot{N}_{H_2O}^{cons}}{A} \quad (3.38)$$

$$n_{H_2} = \frac{\dot{N}_{H_2}^{gen}}{A} \quad (3.39)$$

$$n_{H_2O}^{cat} = \frac{\dot{N}_{H_2O}^{mem}}{A} \quad (3.40)$$

Since disruptions from input and output flows can be neglected, these molar flows determine the molar fractions at the anode and cathode side. By multiplying these fractions with the anode and cathode pressure, the partial pressures of the reactants can also be calculated [57].

$$X_{O_2} = \frac{n_{O_2}}{n_{O_2} + n_{H_2O}^{an}} \quad (3.41)$$

$$X_{H_2} = \frac{n_{H_2}}{n_{H_2} + n_{H_2O}^{cat}} \quad (3.42)$$

$$p_{O_2} = X_{O_2} \cdot p_{an} \quad (3.43)$$

$$p_{H_2} = X_{H_2} \cdot p_{cat} \quad (3.44)$$

The molar generation rates of oxygen and hydrogen and the consumption rate of water can be given by Faraday's law assuming a perfect faradaic efficiency:

$$\dot{N}_{O_2}^{gen} = \frac{I}{4F} \quad (3.45)$$

$$\dot{N}_{H_2}^{gen} = \frac{I}{2F} \quad (3.46)$$

$$\dot{N}_{H_2O}^{cons} = \frac{I}{2F} \quad (3.47)$$

To know the molar fluxes, it now only remains to calculate the molar flow rate of water through the membrane. This flow is governed by three mechanisms: diffusion, electro-osmotic drag and the hydraulic pressure effect [57]. The diffusion through the membrane can be calculated by Fick's law, given by Equation 3.48 for this case, with the diffusion coefficient for water $D_w = 1.28 \cdot 10^{-6} \text{cm}^2/\text{s}$ [57].

$$\dot{N}_{H_2O}^{diff} = \frac{A \cdot D_w}{\delta_{mem}} (C_{H_2O,mem}^{cat} - C_{H_2O,mem}^{an}) \quad (3.48)$$

As first represented by Equations 3.17-3.18, the concentration at the membrane surface can be related to the concentration within the plate channels by the molar flux, electrode thickness and effective diffusion. Consequently, the water concentration at both sides of the membrane is given by Equations 3.49-3.50.

$$C_{H_2O,mem}^{an} = C_{H_2O,ch}^{an} - \frac{\delta_{el}^{an} \cdot n_{H_2O}^{an}}{D_{eff}^{an}} \quad (3.49)$$

$$C_{H_2O,mem}^{cat} = C_{H_2O,ch}^{cat} - \frac{\delta_{el}^{cat} \cdot n_{H_2O}^{cat}}{D_{eff}^{cat}} \quad (3.50)$$

The channel concentration for water is given by Equation 3.51 [57], being the same at the anode and cathode side if the temperature is uniform. However, dependence on the molar water flux makes this problem recursive, requiring a starting value to be included in the model calculating this concentration.

$$C_{H_2O,ch} = \frac{\rho_{H_2O} \cdot T}{M_{H_2O}} \quad (3.51)$$

The molar flow due to the electro-osmotic drag and hydraulic pressure are given by Equations 3.52 and 3.53 respectively.

$$\dot{N}_{H_2O}^{eod} = \frac{n_d \cdot I}{F} \quad (3.52)$$

$$\dot{N}_{H_2O}^{hp} = \frac{K_{Darcy} \cdot A \cdot \rho_{H_2O} \cdot \Delta p}{\delta_{mem} \cdot \mu_{H_2O} \cdot M_{H_2O}} \quad (3.53)$$

In Equation 3.52 n_d is the electro-osmotic drag coefficient. There is no consensus on the value of this parameter. In [108] n_d is estimated at 0.27 based on experimental data. It is also reported in [115] that the electro-osmotic drag coefficient is linked to the humidification λ in the membrane, reaching values between 1 and 2.5. In [104] n_d is used as a fitting parameter, resulting in a value of 5. Finally, [103] reports a value of 7, as a result the observed large water flow to the cathode. In this thesis $n_d = 7$ is further used to model the electro-osmotic drag, based on [57] and [103].

The hydraulic pressure component of the membrane flow, given by Equation 3.53, is represented by Darcy's law. However, due to the assumption of a uniform pressure at the anode and cathode side, this flow does not take place in the considered electrolyzer.

With all parameters determining the electrolyzer voltage fully described in this and the previous section, it is now possible to integrate these equations into the

Simulink model shown in Figure 3.4. With the inclusion of a starting value for the membrane water concentration, this model can calculate the electrolyzer voltage for any input current, temperature and pressure of the electrolyzer. The Matlab functions used for the anode, cathode membrane and voltage subsystems are given in Appendix A. The polarization curve shown in Figure 2.4 is the result of this model for a current density increasing from 0 to 2 A/cm². This model is essential for calculating the output-side operating points for the modeled DC/DC converter in later chapters.

3.4 Commercial Electrolyzer Model

The constructed Simulink model describes the IU-behavior of a single PEM cell. However, the **Commercial Electrolyzer** considered in this thesis consists of several cells in series. This allows the hydrogen output of the electrolyzer to be increased while increasing the total voltage, limiting the required step-down ratio of the DC/DC converter. At the request of **Company**, the exact amount of cells is not given exactly. The undisclosed amount of cells considered in the calculations and models in this thesis is referred to as **M**.

Table 3.2 lists the relevant data necessary to use the **Commercial Electrolyzer** in the developed model⁴. Further operating specifications, such as the current and voltage setpoint can be calculated by this mathematical model.

TABLE 3.2: Operating data of the **Commercial Electrolyzer**

Operating characteristics	
Cell stack layout	M in series
Nominal hydrogen output	250Nm ³ /h
Pressure	30 bar
Nominal power	1.7 MW

Further data was not communicated, due to commercial sensitivity. However, the given characteristics from Table 3.2 in combination with the modeling assumptions made in Sections 3.2 and 3.3 allow the calculation of a polarization curve by the Simulink model as shown in Figure 2.4. Furthermore, the nominal hydrogen output and stack structure lead to the derivation of a nominal IU-setpoint. Figure 3.5 shows how the input current and voltage interact with the cell stack. Since the cells are serialized, the current I_{el} passes through each cell at the same magnitude with each cell causing a voltage drop of U_c . However, each cell simultaneously produces

⁴The cell stack layout is provided by **Company**, the other characteristics can be found online on the datasheet of the **Commercial Electrolyzer**, which is not referenced here for the sake of anonymity

hydrogen, resulting in a cell output of

$$\dot{V}_{H_2,c} = \frac{250 \text{ Nm}^3/\text{h}}{\mathbf{M}} = 1.1792 \text{ Nm}^3/\text{h} \quad (3.54)$$

$$\dot{V}_{H_2,c,s} = \frac{\dot{V}_{H_2,c}}{3600} = 3.2757 \cdot 10^{-4} \text{ Nm}^3/\text{s} \quad (3.55)$$

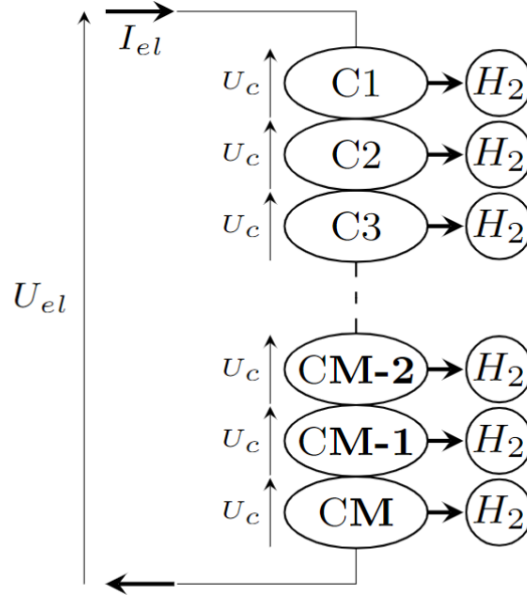


FIGURE 3.5: Stack model of the serialized electrolyzer cells

Equation 3.55 gives the hydrogen output of a single cell per second, allowing the calculation of a cell current with Faraday's law by converting the output from a normalized volume to a molar flow with the ideal gas law:

$$\dot{N}_{H_2} = \frac{p \cdot \dot{V}_{H_2,c,s}}{RT} \quad (3.56)$$

$$I_{el} = \dot{N}_{H_2} \cdot 2 \cdot F \quad (3.57)$$

Since the volumetric output flow is measured at standard conditions, p and T in Equation 3.56 are taken as $p = 1.01325 \cdot 10^5$ Pa and $T = 273.15$ K. With the stack current, pressure and cell area known, the cell voltage can be calculated with the Simulink model and multiplied by \mathbf{M} resulting in the nominal IU-setpoint:

$$I_{el} = 2820.2 \text{ A} \quad (3.58)$$

$$U_{el} = 594.768 \text{ V} \quad (3.59)$$

3.5 Electrical Model

Since the electrolyzer is considered a DC load, it could be expected that it is electrically modeled as a resistance, corresponding to the IU-setpoints calculated

by the Simulink model. However, there are some dynamic aspects that need to be taken into account even when the steady-state connection to a DC/DC converter is considered, particularly, the PEM electrolyzer's stack capacitance. The total electrolyzer stack is reported by **Company** to have a capacitance of around 500 mF. The large size of this capacitance has an impact on the output current ripple of the DC/DC converter and can not be neglected. Consequently, an electrical equivalent model taking this capacitance into account must be constructed. This model can then be integrated into the DC/DC converter model in Plescs at the output side of the converter.

An electrical equivalent model for a PEM electrolyzer is developed in [101, 102]. The resulting model is depicted in Figure 3.6. The resistances and voltage source represent the overvoltages, while the capacitors are fitted to accurately represent the transient time constants reported in [101], measured by applying voltage steps to study the dynamic behavior of a PEM electrolyzer.

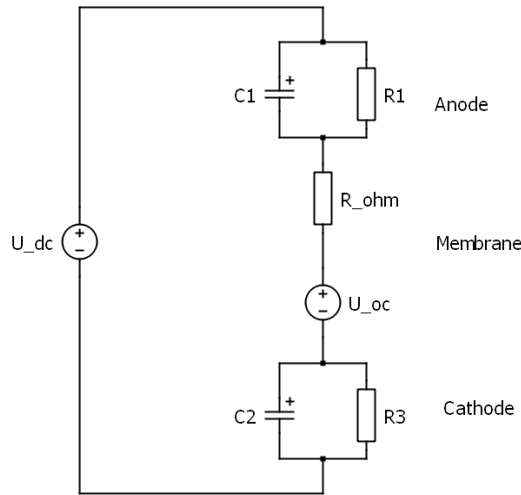


FIGURE 3.6: Dynamic electrical equivalent model of a PEM electrolyzer

However, these fitted parameters are specific to the studied operating points. Therefore, in [102] the model is improved to consist of variable parameters, adjusting to a change in power setpoints. The tests in these papers are done with a 400 W PEM electrolyzer, so it is unlikely that any of the calculated parameters could be transferred to a model of the **Commercial Electrolyzer**. The same equivalent electrolyzer circuit is studied in [116] for DC/DC converter modeling applications. It is concluded there that this model can be used at the output side of a converter model with relative accuracy, reaching the highest errors at low currents.

Thus, the model shown in Figure 3.6 poses a promising equivalent electrical scheme to model electrolyzer cells in an electrical application. However, a further simplification is made in this thesis. Since all M cells of the considered electrolyzer are connected in series, the Ohmic resistance and open-circuit voltages can be summed. This results in an equivalent resistance and voltage drop equal to M times that of a single cell. This leaves M anode circuits and M cathode circuits consisting of a

parallel resistance and capacitor. Only the total capacitance of the electrolyzer is known and no dynamic data is available to calculate the required time constants, Therefore, these 2M remaining circuits are lumped into one parallel circuit of a resistor and a capacitor, resulting in the circuit model depicted in Figure 3.7. The capacitance is kept constant at 500 mF while the resistances and open-circuit voltage are adapted to accurately represent the losses at different operating points, as can be calculated by the transport-based Simulink model.

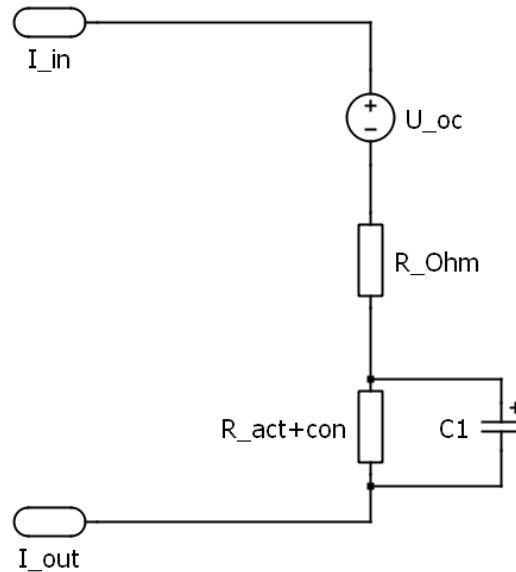


FIGURE 3.7: Electrical equivalent electrolyzer model used in power electronic simulations

3.6 Conclusion

This chapter closely considered the inner working principles of a PEM electrolyzer, analyzing the governing principles leading to losses and determining the voltage-current characteristics. Two models are constructed: the Simulink model is able to calculate the different voltage components of the electrolyzer for any current input, ambient conditions or electrolyzer dimensions. The calculated values for the voltage drops and resistances within the electrolyzer are then modeled in the simplified electrical circuit given in Figure 3.7, accurately representing the steady-state behavior of the **Commercial Electrolyzer** in the electrical simulations in Plects.

Chapter 4

Converter Design

4.1 Introduction

This chapter treats the design and modeling of a step-down DC/DC converter meant to power the **Commercial Electrolyzer**, which has been modeled in the previous chapter. Firstly, the different operating parameters at the input-side of the converter are discussed in Section 4.2. These input conditions determine the required conversion ratio and play a large role in determining the requirements of the DC/DC converter, such as the current and voltage capacity. Section 4.3 briefly discusses the decision-making methodology that influences the design of the DC/DC converter. Giving an overview of which aspects are the most limiting to the design and where the main focus is put.

In Section 4.4 a comparison is made between the suitable topologies that were found in Section 2.6 of the literature study. The feasibility of the different basic topologies is investigated and a single basic topology is selected. This topology is then fully modeled and dimensioned in Section 4.5, after which a basic assessment of the performance and losses is presented in Section 4.6.

Finally, Section 4.7 discusses alternatives and improvements to the basic converter topologies that might lead to cost reductions or efficiency improvements. These alternative implementations are compared to the basic topology in Chapter 5.

4.2 Input Conditions

This thesis considers an electrolyzer, powered by a DC network. The specifications of this network play an important role in the design requirements of the step-down DC/DC converter. Section 2.5 outlines the efficiency benefits of powering DC sources with a direct connection to a DC grid with a high integration of PV and battery systems. As discussed, this thesis considers a LVDC grid that can be regulated between 700 V and 1000 V to power the electrolyzer at its rated capacity. It is assumed that the DC grid is sufficiently strong to withstand the currents drawn by the converter in this application. Consequently, for the modeling and design of the converter, the power source for the network is considered a steady DC source.

However, the amount of PV directly integrated into the DC network does have an impact on the total system efficiency and is therefore taken into account the discussion of the results.

In addition to a LVDC microgrid, the designed DC/DC converter is also tested with a direct connection to a utility scale PV farm, underscoring the importance of using renewable power to generate hydrogen. Corresponding to the electrolyzer’s rated power, a 1.7 MW solar farm is considered. Efficient Sunpower Maxeon 3 modules [117] are assumed¹. The relevant data for this solar module is listed in Table 4.1.

TABLE 4.1: Operating characteristics of the Sunpower Maxeon 3 module used in the solar farm case study

Sunpower Maxeon 3	
P_{nom}	400 W
I_{nom}	6.08 A
U_{nom}	65.8 V
η_{nom}	22.5 %

The PV modules are connected in strings of 10, reaching a nominal voltage of 658 V for the solar farm, consisting of 425 parallel strings. Losses and efficiency issues are not considered for the solar farm. It is simply considered as a variable power source for the electrolyzer at a constant voltage.

Hourly solar farm output data can be acquired from renewables.ninja [81–83]. It would however not be tractable to perform a calculation with the designed converter for every different power setpoint. Therefore, the electrical power generated by the PV farm is only considered in steps of 100 kW within the electrolyzer’s operating range of 85 kW-1678 kW. The performance of the DC/DC converter is then evaluated at these power setpoints. The total amount of hydrogen produced can be calculated based on the amount of hours the solar farm reaches the set power levels.

As a final approximation for the PV farm case study, it is assumed that the output voltage of the PV strings remains constant. This assumption is made based on [119], where it is illustrated with Figure 4.1 that the MPPT-voltage of a monocrystalline PV module remains almost constant for varying irradiance levels.

Thus the different input conditions considered in the modeling of the DC/DC converter are described. During the design of the converter, the main focus is put on optimising the efficiency for operation with the DC grid. The solar farm case serves mainly as a case study into the possible efficiency gains compared to the reference implementation while also highlighting the operational qualities of the converter, such as efficiency and output ripple size, over its entire operating range.

¹The choice for the specific PV module is of little importance, since they are only considered to model the constant input DC source of the DC/DC converter. The Maxeon 3 was chosen here because it is a highly efficient module, with a high power density, even though it is typically used for residential applications [118].

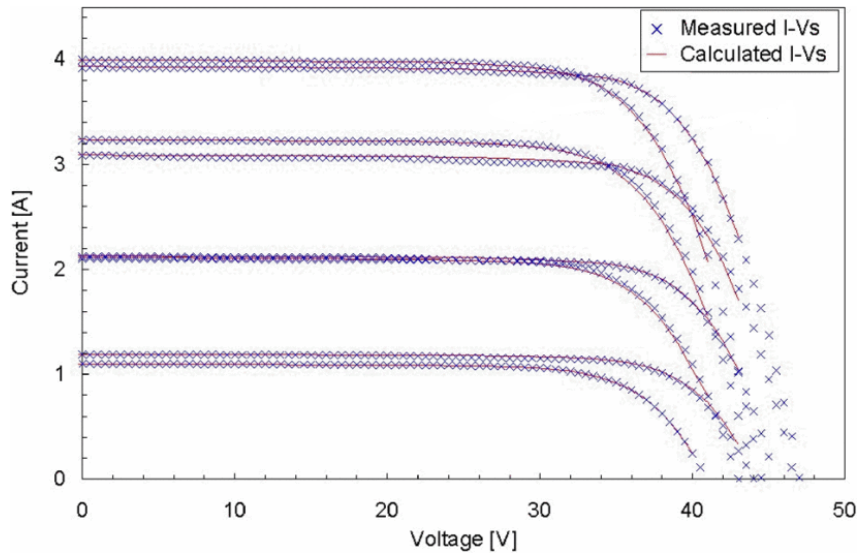


FIGURE 4.1: IU-curves of a monocrystalline PV modules for varying irradiance levels

4.3 Design Methodology

The aim of this thesis is to design a DC/DC step-down converter that can efficiently power the electrolyzer system. The main design parameter for the converter topology is consequently the total system efficiency. However, certain limits accompany the topology design. Particularly, the component ratings may pose a significant limit on the potential of many converter topology types. Therefore, the selection of the components is essential when considering the converter design. The choice is made here to work with off-the-shelf power electronic components, leading to a converter that can easily be constructed if it is viable to use in commercial applications.

The Belgian and UK Farnell online stores are used as the main source for components [120, 121]. These stores have thousands of components of any type and easy filtering functionality, allowing the selection of components based on specific functional requirements and ratings. If no adequate components are found here, additional online searches are conducted to find the required materials.

The design of the step-down DC/DC converter topology is carried out based on the following design principles:

1. **Capacity to operate at optimal conditions:** operate well at the required duty cycle, as well as withstanding the applied current and voltage stress in nominal operation
2. **Operate at a high efficiency:** maximize output power over input power and limit losses inside the converter
3. **Limit current ripple:** although the influence is not directly quantifiable, large ripples negatively affect the electrolyzer, making a low output current ripple by the converter a beneficial characteristic

4. **Minimize cost:** choose components and topology designs that limit the total cost of the converter

The ranking of these principles provides a general view of their respective priority within the design, although not purely strict. For example, satisfying the required capacity or improving the efficiency is generally prioritized over minimizing the cost, but it is possible that certain trade-offs are made to improve a certain aspect if the impact on the more prioritized design parameters remains limited.

4.4 Basic Topology

It is clear from Section 4.2 that the high nominal current of the electrolyzer applies a significant load to the components used in the DC/DC converter. Therefore, the basic topology for the design must be fit to allow high currents without overloading the internal components. In Chapter 2, two topology types are designated as the main contenders for the considered application: the *interleaved buck converter* (IBC) and *full-bridge converter* (FBC). These basic converter types are further examined in this section in order to settle on a basic converter model to use in conjunction with the electrolyzer and upon which further improvements are considered.

4.4.1 Full-bridge converter

The FBC, as described in Chapter 2 and depicted in Figure 2.10b, is an isolated DC/DC converter consisting of a full-bridge inverter, an AC transformer and an output rectifier and filter. As given by Equation 2.18 the DC voltage conversion ratio is given by $R_{FB} = 2 \cdot \frac{D}{N_t}$. In this subsection a more detailed analysis of this converter's characteristics is provided.

A FBC generates an alternating voltage at a high frequency by alternating the opening switches at the input-side. The upper and lower switches of an inverter leg are phase-shifted by one half of a period, limiting the duty cycle to 0.5 to avoid short-circuiting the source [84]. The two legs are also phase-shifted by this half period to provide the alternating voltage shown in Figure 4.2. This figure shows the voltage waveforms relative to the input voltage measured at the primary and secondary of the transformer, at the output-side of the diode rectifier and behind the output filter of the converter. A duty cycle and transformer ratio of $D = 0.4$ and $N_t = 2$ are used to generate these waveforms resulting in an average DC output voltage of $\frac{U_o}{U_{in}} = 0.4$ as predicted by Equation 2.18.

A three-phase transformer can be used to increase the power density of a FBC, using the advantage of a smaller magnetic core of a single transformer compared to three parallel single-phase units [122]. Depending on the the winding connection, additional voltage or current gains can be acquired by making use of either the line or phase voltage [123]. Figure 4.3 depicts a three-phase FBC with a star-delta connected transformer, used to lower the output voltage and increase the output current of the converter [123].

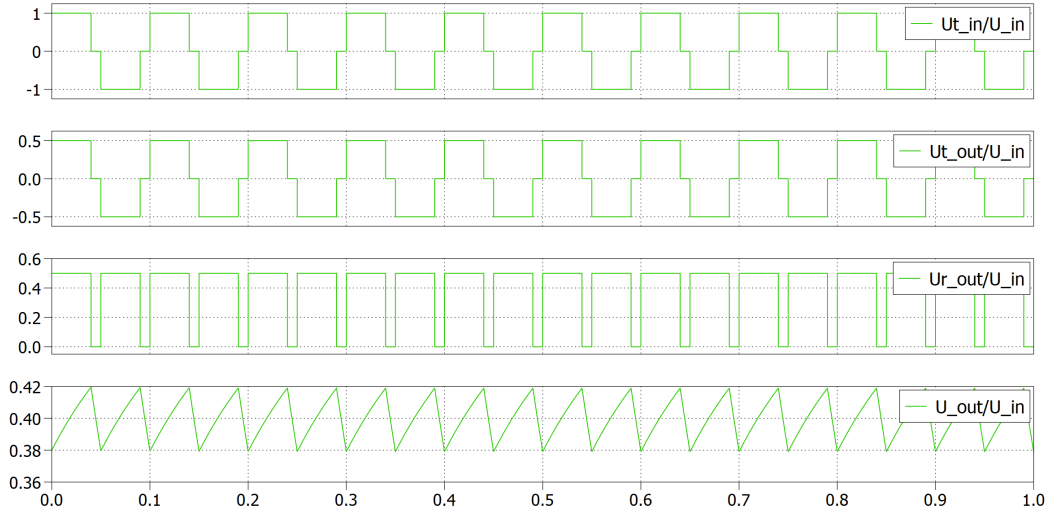


FIGURE 4.2: Voltage waveforms relative to the input voltage at different points in the FBC

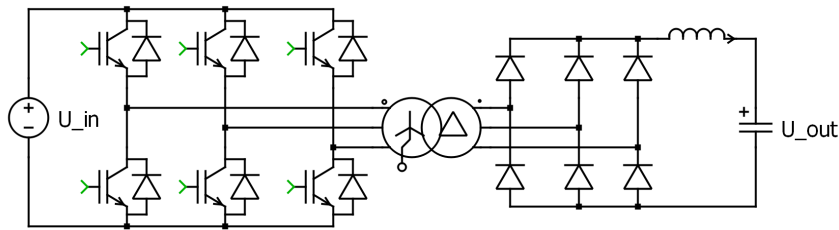


FIGURE 4.3: Three-phase FBC with a Yd connection

The conversion ratio for this converter with the considered connection is given by Equation 4.1 [123]. Changing the transformer connection to a Dy connection would simply yield the inverse of this conversion ratio. Using a Yy or Dd transformer results in a conversion ratio given by Equation 4.2 with D limited to $\frac{1}{3}$.

$$\frac{U_o}{U_{in}} = \begin{cases} \frac{D}{N_t}, & 0 < D \leq \frac{1}{3} \\ \frac{1}{3N_t}, & \frac{1}{3} < D < \frac{2}{3} \\ \frac{(1-D)}{N_t}, & \frac{2}{3} < D < 1 \end{cases} \quad (4.1)$$

$$\frac{V_o}{V_{in}} = \frac{3D}{N_t} \quad (4.2)$$

Having outlined the basic working principles of a single-phase and three-phase FBC, it is now considered whether this topology type is suitable to use for powering the **Commercial Electrolyzer**. For a single-phase converter, the output current waveform is comparable to a standard buck converter. On the other hand, the division of the current over multiple legs improves the power capacity compared to a standard buck converter. The three-phase FBC further increases the power density of this converter type.

However, these converters have a disadvantage for the specific considered use case, regarding the conversion ratio. As stated previously, the voltage ratio of a single-phase FBC is given by $\frac{U_o}{U_{in}} = \frac{2D}{N_t}$, with the duty cycle limited to 0.5. Consequently, to work at nominal power, connected to a 700 V DC grid requiring a conversion ratio of 0.84967, the transformer winding ratio is limited to $N_t = 1.1769$. In practice, this leads to a 1:1 ratio being used in the converter design. Thus any advantages in reducing the input-side current that could be gained by using a transformer with a high winding ratio are eliminated. Furthermore, a single-phase coupled inductor winding is an expensive component and not readily available for high current applications. The same issue occurs for three phase converters where, according to Equation 4.1 a step-up transformer is required to reach the required voltage. For transformers with a Yy or Dy connection, represented by Equation 4.2 the same issues as with a single-phase FBC occur. A Dy connection is more suited for step-up conversions [122], thus also proving inefficient for the considered application.

4.4.2 Interleaved buck converter

The other converter type that is considered suitable to provide the link between an electrolyzer and a DC grid is an interleaved topology. As discussed in Chapter 2, this converter consists of up to six parallel buck converter legs. Thus multiplying the power capacity while retaining the conversion behavior and simple layout of a standard buck converter. The conversion ratio is equal to the duty cycle of the applied pulse signal, which is shifted over the different legs by $\frac{1}{N \cdot f}$ seconds. The biggest disadvantage of this topology is that, like the standard buck converter, it risks operating in DCM at low duty cycles. Whether or not this occurs also depends on the inductance of the output inductors, which also dictate the amplitude of the ripple current.

DCM occurs if the average inductor current I_L becomes smaller than the boundary current I_{LB} , thus becoming zero during the off interval of the switch as shown by Figure 2.6b. I_{LB} is given by Equation 4.3 [84].

$$\begin{aligned} I_{LB} &= \frac{1}{2} I_{L,M} \\ &= \frac{1}{2} \cdot \frac{t_{on}}{L} (U_{in} - U_o) \\ &= \frac{D \cdot T_s}{2L} (U_{in} - U_o) \end{aligned} \quad (4.3)$$

From these equations, it follows that DCM can be avoided by designing the converter to have a high output inductance or switching frequency, since the input and output voltages and average current are set by the application. For interleaved converters the risk for DCM increases since the average inductor current is divided over the different legs. For the considered application a worst-case calculation can be made check whether DCM operation invalidates the possibility of using an IBC. Consider an IBC with six legs operating the electrolyzer at its rated power setpoint, which

is calculated in Section 3.4. To maximize the considered current ripple the input voltage case of $U_{in} = 1000$ V is considered. The average inductor current for a six-phase IBC becomes

$$\begin{aligned} I_L &= \frac{I_o}{6} \\ &= \frac{2820.2 \text{ A}}{6} \\ &= 470.033 \text{ A} \end{aligned} \quad (4.4)$$

The boundary inductor current given by Equation 4.3 in this case amounts to

$$\begin{aligned} I_{LB} &= \frac{0.595 \cdot T_s}{2L} \cdot (1000 \text{ V} - 594.768 \text{ V}) \\ &= 120.509 \cdot \frac{T_s}{L} \end{aligned} \quad (4.5)$$

Consequently, a six-phase IBC used to power the electrolyzer from a 1000 V DC grid does not enter DCM as long as

$$\frac{1}{f \cdot L} \leq \frac{470.03}{120.509} = 3.900 \quad (4.6)$$

This design parameter for the inductor and the switching frequency can be taken into account in the selection of the components during the converter design.

Aside from the risk of DCM, the use of multiple phase-shifted legs has a positive effect on the ripple current. The output currents of the separate legs come together at the common output-side DC bus. Consequently, the different current ripples, each at the switching frequency but mutually shifted, are summed together, creating a ripple current at N times the switching frequency with a reduced amplitude. Figure 4.4 shows a triangular waveform as might be expected at the output of an IBC with up to six legs, with a duty cycle of 0.85. The amplitude of the base ripple is taken as 1. By summing up multiple phase-shifted instances of this identical ripple a frequency increase as well as an amplitude decrease can be observed.

The displayed output ripple behavior is in contrast to that of the FBC where the single filter inductor placed after the rectifier bridge results in a single output ripple.

4.4.3 Conclusion

The two converter types discussed in this section both show promise for powering an electrolyzer. However, for the remainder of this thesis, the preference is given to the IBC, due to the simplicity of its topology and its ability to easily achieve the required conversion ratio, without entering DCM. This is contrasted by the FBC topologies that are more fit to operate at lower output voltages for which the IBC is limited. The inefficiency of using an AC transformer in conjunction with a limited switching duty cycle, causing step-up transformers to be required in some cases, eliminates the full-bridge topology as a contender in the specific application. Therefore, the design and analysis of a six-phase IBC is considered in the remaining chapters and sections of this thesis.

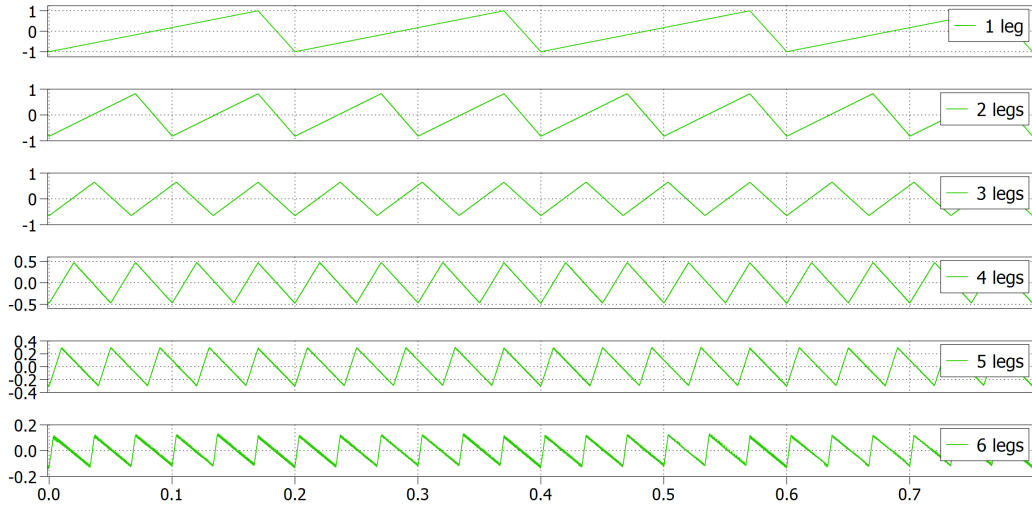


FIGURE 4.4: Output current ripple characteristic for an IBC with up to six phases

4.5 Interleaved Buck Converter Design

With the basic converter topology determined in the previous section, a concrete design can now be made for the IBC. To minimize the current stress on the components a 6-phase implementation is selected. This is considered the practical limit of the amount of parallel phases that can be implemented in this way [88]². The six-phase IBC topology, for which the components are dimensioned in this section, is depicted in Figure 2.7.

As outlined in Section 4.3, the converter is designed with off-the-shelf components. The ability to power the electrolyzer in nominal operation is prioritized with the second focus put on minimizing the component losses.

4.5.1 Inductor dimensioning

The requirements for the inductor rating are given by the nominal electrolyzer current, calculated by the model constructed in Chapter 3. Furthermore, the risk of DCM and the requirement of a low current ripple puts a restraint on the inductance of this component, linked to the switching frequency as is calculated in Section 4.4.

The required DC current capacity is calculated in Equation 4.4 to be 470.033 A. Although the total electrolyzer current is divided over six output inductors, the resulting inductor current still poses a significant limit on the components suited for this converter design. As outlined in Section 4.3 the UK and Belgian Farnell online stores function as a source for components. However, at the time of writing, no inductors rated for this current level are listed on these stores. Therefore a suitable component is found from another source, specialized in designing high power

²It is observed that further increasing the amount of phases causes modeling difficulties in Plecs and leads to very long calculation times and unstable results.

inductors. The HCS-201M-600A High Current Inductor by Coil Winding Specialist Inc. [124] is used. This inductor has a current rating of up to 600 A. The inductance varies with the applied DC current. Figure 4.5 shows the variation of the inductance for different DC currents, that allows the calculation of the inductance at different converter setpoints. Based on this data, an inductance of $56 \mu\text{H}$ is modeled at nominal operation.

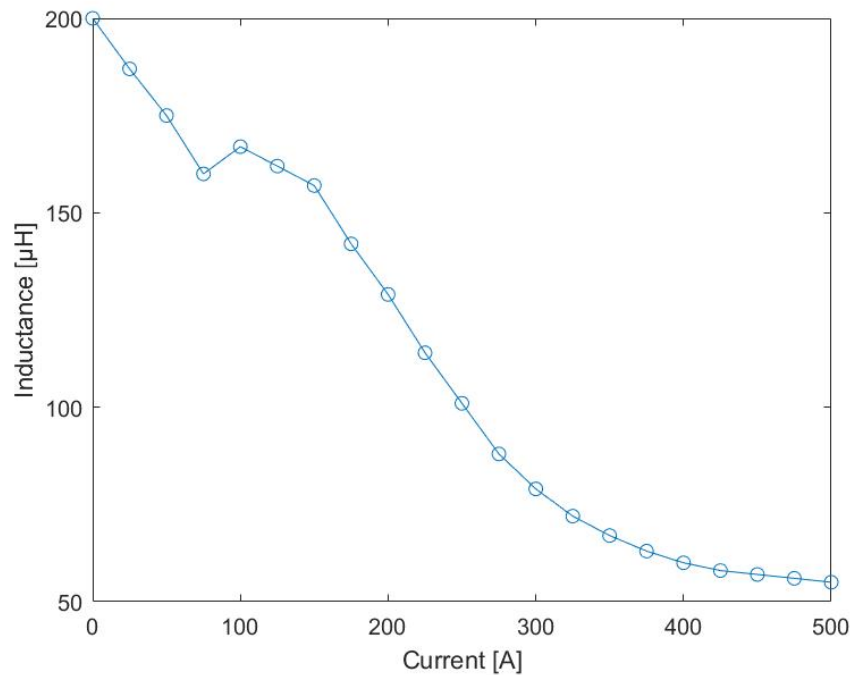


FIGURE 4.5: Inductance of the output inductors in depending on the applied DC current

4.5.2 IGBT dimensioning

The IGBTs must be able to withstand the current and voltage at the input-side of the converter. Furthermore, they determine the allowed switching frequency of the converter. The choice is made to use IGBTs for this converter design, based on their low switching losses and high switching frequency [84]. The selected IGBT is the Semitran 3 module by Semikron [125], as depicted in Figure 4.6. This figure shows that the module can be used bidirectionally but this functionality is not used in the basic design of the converter.

The considered IGBT has a nominal collector emitter current of 400 A and a maximum current rating of 616 A. The switch current in nominal operation is highest for a lower voltage DC network, so for a connection to a 700 V network, the IGBT

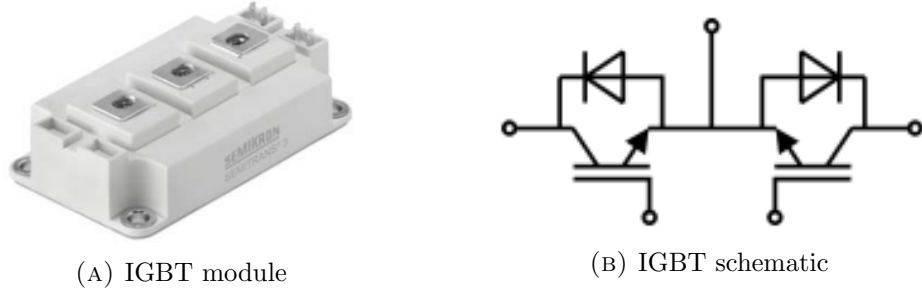


FIGURE 4.6: Semitrans IGBT used in the DC/DC converter design

current becomes:

$$\begin{aligned}
 I_S &= D \cdot \frac{I_o}{6} \\
 &= 0.85 \cdot 470 \text{ A} \\
 &= 399.5 \text{ A}
 \end{aligned} \tag{4.7}$$

In the solar farm use case where the input voltage amounts to 658 V, the current can rise up to 425 A, since the operation mode where the solar farm is generating at maximum capacity is expected to be rare and this current is still within the maximum current rating of the module, this module is deemed appropriate to withstand the required currents of the six-phase IBC.

The nominal blocking collector-emitter voltage amounts to $U_{CE} = 1200 \text{ V}$ meaning that the considered IGBT can power the electrolyzer in nominal operation for every considered input voltage. The maximum switching frequency for this model is 20 kHz. Operating at maximum frequency with the considered HCS-201M-600A inductor at nominal power results in

$$\frac{1}{f \cdot L} = \frac{1}{20 \cdot 10^3 \cdot 55 \cdot 10^{-6}} = 0.9091 \tag{4.8}$$

According to Equation 4.6 this means that no DCM occurs at nominal conditions in the designed converter.

4.5.3 Diode dimensioning

The freewheeling diode needs to support the inductor current during time intervals when the switch is off. Furthermore, it must be able to block the total input-side DC voltage during the IGBT's on-state. The average current for this component is given by Equation 4.9.

$$I_D = (1 - D) \cdot I_L \tag{4.9}$$

Consequently, this component is strongly dependent on the applied input voltage. If the LVDC voltage is regulated up to 1000 V, the diode current becomes $I_D = 190.458 \text{ A}$, while at an input voltage of 700 V this current remains limited to $I_D =$

70.07 A. No suitable diode, is found on the Farnell stores or other web pages to allow the large currents in the 1000 V operating case. However, the inverse diode included in the Semitrans IGBT module is able to withstand both this current and voltage. The disadvantage is that this module comes at a higher cost than a standard diode and showcases slightly increased losses compared to a diode that can be used for a 700 V input case, as is outlined in Section 4.6 and simulated in Section 5.3.

For the 700 V application, the Fast Recovery Epitaxial Diode by IXYS is selected [126]. This diode has a nominal current of 77 A³. However, the diode experiences this current in short intervals of 470 A during 7.5 μ s per period of 50 μ s. For pulses shorter than 10 μ s, the diode is able to sustain currents up to 1200 A, so this does not form a problem for this component. The maximum blocking voltage for this component is 1200 V, meaning that it has no issue blocking the input voltage during the on-state of the converter.

The efficiencies for the 1000 V and 700 V input cases are considered in Section 5.3. Both designs are considered there to ensure that the most efficient implementation is selected .

4.5.4 Capacitor dimensioning

The main purpose of the output capacitor is to reduce the output current ripple by functioning as a low-pass filter together with the output inductors on the legs. It can be calculated that in worst-case ripple conditions, $U_{in} = 1000$ V, the total current ripple for a single phase with no output capacitance is given by Equation 4.10 This results in a ripple amplitude of 219.07 A or 46.61% of the total inductor current.

$$\Delta I_L = \frac{U_{in} - U_o}{L} \cdot \frac{D}{f} = 219.07 \text{ A} \quad (4.10)$$

Summing the different ripples drastically reduces the output ripple to $\Delta I = 36$ A, or a ripple factor (RF) of 1.277% of the total converter output-current. If the polarization curve of the electrolyzer is assumed linear within this range, this results in a voltage ripple of $\Delta U_o = 7.592$ V, similarly representing 1.277% of the total electrolyzer voltage.

According to [127], the magnitude of the output voltage ripple is given by Equation 4.11 for an interleaved converter, with the equivalent inductance given by Equation 4.12.

$$\Delta U_o = \frac{U_{in}}{C \cdot L_{eq}} \cdot \frac{1}{N^3} \cdot \frac{1}{32 \cdot f^2} \quad (4.11)$$

$$L_{eq} = \frac{L}{N} \quad (4.12)$$

For the calculated ripple of $\Delta U_o = 7.592$ V this formula results in a small capacitor of 0.866 μ F. By increasing the size of the output capacitor, the ripple voltage can

³It is stated in the datasheet [126] that the nominal current is limited by 70 A by the leads in the diode. Since the required capacity is 0.5 A above this value and the semiconductor itself is rated above this current limit, this diode is deemed suitable for this application.

therefore further be reduced. For example, if a ripple factor of less than 0.1% is desired, a capacitor of at least $11.06 \mu\text{F}$ would be required, according to this formula.

However, these calculations consider a purely resistive load. As discussed in Section 3.5, the electrolyzer itself has a large capacitance of 500 mF . This means that if no output capacitor is included in the DC/DC converter, the output ripple is filtered by the electrolyzer itself, thus *consuming* the ripple provided by the output inductors. Adding an additional output capacitor can decrease the ripple consumed by the electrolyzer. However, due to the large capacitance of the electrolyzer, very large capacitors are required to significantly reduce the current ripple in the electrolyzer. Figure 4.7 shows the ripple current going into the electrolyzer and filtered out by output capacitors of different sizes.

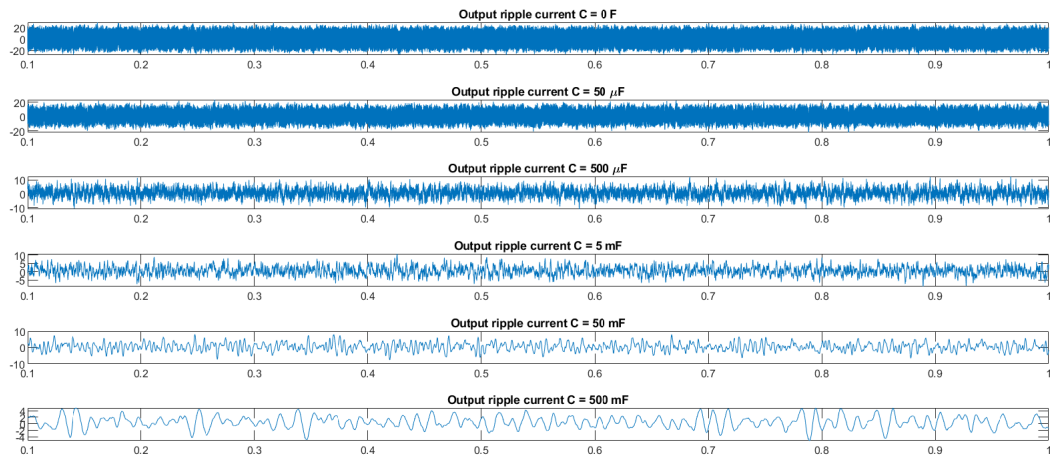


FIGURE 4.7: Current ripple at the output of the converter for different sizes of output capacitor

It can be seen from this Figure that large capacitors are able to reduce the current ripple's amplitude but also reduce the frequency of the voltage and current ripple going into the electrolyzer. The maximum current values showcased by the ripples shown in Figure 4.7 are listed in Table 4.2. When simulating the operation of the converter with these different capacitor sizes, no efficiency difference is found between the different cases. Since it is found in Chapter 2 that the current ripple is most detrimental to the electrolyzer efficiency at lower frequencies, a capacitor that significantly reduces the ripple amplitude without strongly influencing the frequency is required.

Based on the values shown in Table 4.2 and the simulated ripple waveforms, a capacitor of $500 \mu\text{F}$ is chosen. This component is used to reduce the ripple factor to less than 1% in the worst-case scenario. However, this capacitor size can be reduced if less importance is put on the ripple amplitude.

Thus, the C44P-R capacitor by Kemet [128] is selected as the output filter capacitor for the six-phase IBC. For the input case of 700 V , this capacitor leads to a more significant ripple reduction resulting in a maximum current ripple of 20.85 A or 0.74% of the total current. It should however be noted that the calculations in

TABLE 4.2: Maximum current ripple for different output capacitor sizes

Capacitor size	0 F	50 μ F	500 μ F	5 mF	50 mF	500 mF	1 F
ΔI_{max} [A]	57.60	45.58	23.75	19.64	15.69	10.02	6.72
RF [%]	2.04	1.62	0.842	0.696	0.556	0.355	0.238

this subsection consider an ideal capacitor. The selected capacitor has a parasitic resistance and inductance that influences its practical operation in the converter-electrolyzer system. Therefore, the actual value of including this capacitor in the converter design is further considered in Section 5.2, where the converter is modeled with a realistic capacitor to study the influence of these parasitic components.

4.5.5 Converter cost

Since off-the-shelf components from online web stores are used, it is possible to consider the cost of the designed converter [120, 129]. The different component costs are listed in Table 4.3, resulting in a total price of €11092.85 for the converter designed for a 700 V input voltage, while the 1000 V converter costs up to €12051.59. The inductor is the main driver for the cost due to its high current capacity requirement, resulting in either 89.79% or 82.645% of the total converter cost.

TABLE 4.3: Price list for the designed interleaved converter

Component type	Name	Price per part [€]	Total cost [€]
IGBT	SKM400GM12T4	167.98	1007.88
Diode	DSEI120-12A	8.19	49.14
Inductor	HCS-201M-600A	1610	9960
Capacitor	C44PLGR6500RBSK	75.83	75.83
Total	700 V		11092.85
	1000 V		12051.59

4.6 Losses

The goal of the converter design in this thesis is to power the electrolyzer at a high efficiency. To calculate the efficiency of the DC/DC converter with the selected components, the losses are included in the Plecs model. These losses are calculated based on parameters included in the datasheets of these components⁴. Table 4.4 lists the losses considered for each component in the DC/DC converter, as well as the relevant parameters provided in the respective datasheets [124–126, 128]. In Section 4.5 the components showcasing the most efficient values regarding the parameters in Table 4.4 are selected if they satisfy the required capacity characteristics.

⁴The full datasheets for the considered power electronic components are included in Appendix B

TABLE 4.4: Loss characteristics of the components in the DC/DC converter

Component	Loss type	Datasheet parameter
Inductor	Resistive losses	$R_{DC} = 2.7 \text{ m}\Omega$
IGBT	Forward voltage drop	$U_{ce0} = 0.8 \text{ V}$
	Conducting losses	$R_{ce} = 2.5 \text{ m}\Omega$
	Leakage losses	$R_{off} = 240 \text{ k}\Omega$
	Switching losses	$t_{rise} = 47 \text{ ns}$ $t_{fall} = 78 \text{ ns}$
Diode	Forward voltage drop	$U_0 = 1.2 \text{ V}$ $R_0 = 4.5 \text{ m}\Omega$
	Leakage losses	$R_{off} = 200 \text{ k}\Omega$
	Reverse recovery loss	$t_{rr} = 40 \text{ ns}$ $-\frac{dI_r}{dt} = 200 \text{ A}/\mu\text{s}$
Capacitor	Series parasitic resistance	$R_C = 1.2 \text{ m}\Omega$
	Series inductance	$L_C = 160 \text{ nH}$
Inverse IGBT diode	Forward voltage drop	$U_0 = 1.5 \text{ V}$ $R_0 = 2.5 \text{ m}\Omega$
	Leakage losses	$R_{off} = 240 \text{ k}\Omega$
	Reverse recovery loss	$t_{rr} = 151.1 \text{ ns}$ $-\frac{dI_r}{dt} = 8800 \text{ A}/\mu\text{s}$

The losses inside the DC/DC converter have an impact on the control of the switches. The voltage drops caused by the different components must be taken into account when calculating the applied duty cycle to reach the desired electrolyzer voltage. For a lossless DC/DC buck converter operating in CCM, it is considered that

$$\left. \frac{dI_L}{dt} \right|_{on} = - \left. \frac{dI_L}{dt} \right|_{off} \quad (4.13)$$

$$\Rightarrow D \cdot (U_{in} - U_o) = (1 - D) \cdot U_o \quad (4.14)$$

By adapting Equation 4.14 to consider the voltage over the inductor taking into account the losses as in Equation 4.15, the adapted duty cycle for the converter can be calculated by Equation 4.16.

$$D \cdot (U_{in} - U_S - U_L - U_o) = (1 - D) \cdot (U_o - U_L + U_D) \quad (4.15)$$

$$D = \frac{U_o + U_L + U_D}{U_{in} - U_S - U_D} \quad (4.16)$$

These voltage drops influencing the duty cycle of the converter are represented for one converter leg in Figure 4.8, but are equal for all parallel legs of the converter.

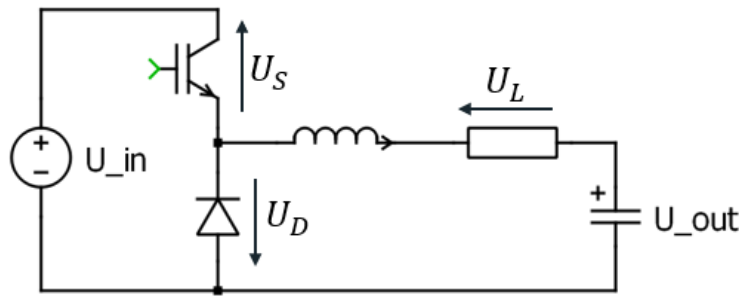


FIGURE 4.8: Resistive voltage drops in a single converter leg

Since these voltage drops are either purely resistive or have a resistive component, they are dependent on the applied duty cycle of the control signal. Calculating the exact duty cycle thus needs to be done iteratively, adjusting the losses according to the duty cycle until Equation 4.16 converges. Furthermore, losses such as the switching losses, reverse recovery losses, leakage losses and capacitor losses are not modeled as voltage drops. Therefore, to exactly match the required output current and voltage level, the duty cycle must be calculated as

$$U_{in} \cdot I_{in} = U_o \cdot I_o + P_{loss} \quad (4.17)$$

$$\Rightarrow D = \frac{U_o}{U_{in}} + \frac{P_{loss}}{I_o} \quad (4.18)$$

Since the magnitude of the losses is not known beforehand, Equation 4.18 can not be used to set the duty cycle in the simulation of the converter, unless this too is adjusted iteratively. In Chapter 5, where the converter is simulated in PLECS for many operating points, Equation 4.16 is used to gain a starting point for the duty cycle, after which the simulation can be repeated to acquire the correct voltage and current at the output-side. However, due to the long simulation for each calculation, the number of iterations that can be conducted is limited, leading to a certain error on the output voltage and current that is accepted in the simulation results.

4.7 Alternative designs

The six-phase IBC designed in this chapter is a basic converter circuit that is able to power the electrolyzer in the required operational circumstances. In this section it is considered whether further improvements to this basic topology can be made to improve the total efficiency or cost of this converter for one or more operating conditions.

4.7.1 Modular design

The high power of the electrolyzer places a significant capacity requirement on the possible components. The current strain can be lowered by increasing the number of

conducting legs. However, for interleaved converters the maximum amount of phases is limited to six due to the practical limitations of the control signals. Therefore, it is possible to utilize a modular design allowing multiple interleaved or single-phase buck converters to be connected in parallel to reduce the current stress on the components. Furthermore, a series modular design can be used to also limit the voltage stress across the components. Since the inductor, which is constrained by the current magnitude, amounts up to 89.79% of the total converter cost, using a parallel modular design to allow different lower rated inductors allows for significant cost reductions. Six modular designs are considered:

- Twelve single-phase buck converters
- Six two-phase IBCs
- Two six-phase IBCs
- 24 single-phase buck converters
- Twelve two-phase IBCs
- Four six-phase IBCs

Using modular topologies with twelve total parallel conducting legs results in an inductor current of 235.02 A. The IHXL-1500VZ-5A inductor by Vishay [130] is selected for this application. The maximum current passing through the IGBTs amounts to 212.43 A in solar farm operating case. Therefore, a cheaper transistor: the IXYH85N120A4 IGBT by IXYS [131] can be used. The diode is mainly constrained by the magnitude of the electrolyzer voltage and has a low cost compared to the inductor and switches, no replacement is sought for this component. In the 1000 V LVDC case the Semitrans bidirectional IGBT is also kept to fulfill the diode's functionality, since this component still endures high currents for periods of approximately 20 μ s every cycle. Parallel modules have as the main difference that they do not share a common output capacitor. The selected capacitor from the previous section is retained in the basic parallel design, since the output ripple is expected to increase in modular designs using less than six phases. However, the capacitor size is not increased, since it already makes up a significant portion of the price of the modular converters.

A modular design concerning 24 parallel single-phase buck converters is also considered. The switch and inductor currents are therefore halved once again. However, the most suited inductor found on the farnell store [120, 121], based on the component ratings, is the same inductor as used in the twelve-phase implementation. A lower rated and cheaper IGBT can yet be found in the Ultra Field Stop IGBT by ON Semiconductor [132]. The ratings and cost of the newly selected components are listed in Table 4.5. With these new components, due to the lower inductance, switching frequency and average inductor current, these modular converter designs must be checked for DCM operation by means of Equation 4.8. The average inductor currents for the 12- and 24-phase implementations need to exceed the limit current

TABLE 4.5: Components used in modular converter design using 12 or 24 phases

Component	Specifications	Cost [€] [120]
IHXL-1500VZ-5A [130]	Inductor	27.16
	I_{max}	235 A
	$L_{@235A}$	0.68 μ H
	$R_{DC,@235A}$	0.12 m Ω
	$L_{@117.5A}$	3.3 μ H
	$R_{DC,@235A}$	0.4 m Ω
IXYH85N120A4[131]	IGBT	14.46
	U_{CES}	1200 V
	I_{CE}	300 A
	U_{CEon}	1.8 V
	f_{max}	5 kHz
	t_{rise}	40 ns
	t_{fall}	280 ns
	R_{off}	120 M Ω
FGH40T120SQDNL4[132]	IGBT	7.39
	U_{CES}	1200 V
	I_{CE}	160 A
	U_{CEon}	1.7 V
	f_{max}	20 kHz
	t_{rise}	33 ns
	t_{fall}	56 ns
	R_{off}	3 M Ω

I_{LB} which is given by Equations 4.19-4.20 respectively for the 1000 V case and Equations 4.21-4.22 for the input voltage of 700 V.

$$\begin{aligned}
 I_{LB} &= \frac{0.59477}{2 \cdot 0.68\mu\text{H} \cdot 5\text{kHz}} \cdot (1000\text{V} - 594.77\text{V}) \\
 &= 35.44 \text{ kA}
 \end{aligned} \tag{4.19}$$

$$\begin{aligned}
 I_{LB} &= \frac{0.59477}{2 \cdot 3.3\mu\text{H} \cdot 20\text{kHz}} \cdot (1000\text{V} - 594.77\text{V}) \\
 &= 1.826\text{kA}
 \end{aligned} \tag{4.20}$$

$$\begin{aligned}
 I_{LB} &= \frac{0.85}{2 \cdot 0.68\mu\text{H} \cdot 5\text{kHz}} \cdot (700\text{V} - 594.77\text{V}) \\
 &= 13.154 \text{ kA}
 \end{aligned} \tag{4.21}$$

$$\begin{aligned}
 I_{LB} &= \frac{0.85}{2 \cdot 3.3\mu\text{H} \cdot 20\text{kHz}} \cdot (700\text{V} - 594.77\text{V}) \\
 &= 677.62 \text{ A}
 \end{aligned} \tag{4.22}$$

These equations show that the current minimum for avoiding DCM vastly exceeds the

average inductor currents. The choice of components for the modular implementations should thus be adjusted to lower I_{LB} for the considered applications. The main drivers for the high I_{LB} are the low inductance of the inductor for both implementations and the lower switching frequency for the 12 leg case. The required inductances to drive the limit current below the actual average inductor currents are listed in table 4.6.

TABLE 4.6: Minimum inductance to avoid DCM in modular converter implementations

Modular case	Input voltage	L_{min} μH
12 phases	1000	102.42
	700	38.06
24 phases	1000	51.21
	700	19.03

Components with these required inductances, able to withstand the average current of the 12- and 24-leg implementations can be found on the CWS store [129]. These inductors do not showcase any cost benefit compared to the inductor used in the standard six-phase design. Therefore, the selected inductors in the considered modular designs are not replaced.

However, as shown in Section 5.5, modular topologies using interleaved modules have a lower risk of entering DCM due to the phase-shift in the output waveform. Therefore, in Chapter 5 only the two-phase and six-phase implementations are simulated to study the performance of a modular converter design.

To avoid DCM in a modular implementation, an topology layout using even more parallel converter legs can be considered. This way, higher switching frequencies could be used and inductors with higher inductances at the cost of a lower current rating could be utilized. However, further decreasing the average leg current also limits the maximum value of I_{LB} thus posing additional constraints to avoid DCM. Solving this problem by optimizing the amount of parallel legs, based on all the available components, is left out of the scope of this thesis. It is estimated that many parallel phases operating at a very high frequency would be required. However due to the time constraints on component selection and modeling this implementation is not developed here.

Table 4.7 lists the total converter and implementation costs of the different considered modular designs for the 700 V case⁵. It can be seen that these modular designs are very cheap compared to the single six-phase IBC using the high current inductor. The output capacitor makes up the biggest share of the total cost for the converters with less parallel phases. In the next chapter, the performance of these

⁵In the 24-leg implementation, the diode functionality can be fulfilled by the same diode for the 1000 V and 700 V cases, resulting in no cost difference between the 1000 V and 700 V cases. In the 12-phase cases, the cost difference between the two input voltage designs amounts to €159.78 per leg for a total additional cost of €191748 for the 1000 V case.

different modular designs is compared to the standard six-phase IBC to see which converter type achieves a better efficiency.

TABLE 4.7: Costs for the modular converter topologies

Modular layout	Converter cost [€]	Total cost [€]
12 Single-phase buck converters	125.64	1507.68
6 Two-phase IBCs	175.45	1052.7
2 Six-phase IBCs	374.51	749.02
24 Single-phase buck converters	118.57	284.568
12 Two-phase IBCs	161.21	967.86
4 Six-phase IBCs	332.27	664.54

4.7.2 Topology improvements

In addition to adding components to reduce the overall cost of the converter, extra components can also be added with the goal of improving the converter efficiency. Most commonly, research into improved IBCs concerns improving the conversion ratio range, allowing the converter to reach lower output voltages without lowering the duty cycle enough to risk DCM. [93, 95, 133, 134]. An example of such an improved topology from [93] is shown in Figure 2.8 with its loss characteristics for $D < 0.5$ depicted in Figure 2.9. These loss characteristics show significant efficiency improvements for this simple improved topology.

However, due to the focus on low output voltages in these improved IBC designs, the efficiency improvements are mainly reported for duty cycles of $D < 0.5$. Due to an increased amount of switches and higher duty cycles for conversion ratios above 0.5, the conduction losses in these improved converters increase, especially when operated at duty cycles of more than 50% [93, 133].

The calculation of different operating setpoints for different input powers conducted in Chapter 5 shows that electrolyzer voltage only reaches below 500 V if the input power is less than 500 kW, as shown in Table 5.3. Consequently, in the considered **Commercial Electrolyzer** application, the conversion ratio only reaches below 0.5 if the electrolyzer is operated at less than 24% of the rated power while connected to the 1000 V LVDC grid. Therefore, these converter designs with extended duty cycles do not offer efficiency improvements in the application of this thesis and are not further considered.

4.7.3 Soft-switching circuits

Finally, the addition of soft-switching circuits to eliminate the switching losses in the proposed IBC is considered. Soft-switching circuits can be achieved in several ways. Resonant LC circuits are used to ensure that the switching operation either occurs at zero current or zero voltage. Figure 4.9 shows two resonant circuits for zero current switching (ZCS) and zero voltage switching (ZVS). Due to the resonating behavior of

these components, either the current or the voltage over the switch is automatically drawn back to zero, allowing the switch to be opened without losses [84].

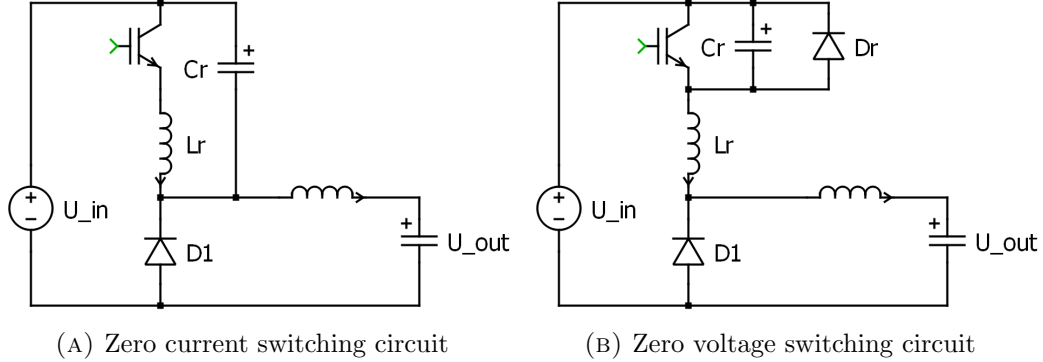


FIGURE 4.9: Buck converter with a ZCS and ZVS resonant circuit

Many different practical implementations of these resonant circuits have been considered in literature [135–138]. However the dimensioning of these circuits is based on a set switching frequency and duty cycle, because the required oscillatory frequency of the components is dependent on these factors [138]. The aim of this thesis is to design a DC/DC converter that can operate an electrolyzer at different power setpoints, and thus at different output voltages, as well as with different input voltage conditions. Therefore, it is not suitable to include resonant circuits in the topology.

4.8 Conclusion

It can be concluded that, for the conditions set by the considered electrolyzer and input voltages, the IBC design is well suited for the power conversion. Since the high current demand of the **Commercial Electrolyzer** poses a significant load on the components, a six-phase topology is selected over the considered FBC topologies. This six-phase implementation has as an additional advantage that the current ripple is strongly reduced. Due to this low output ripple and the high capacitance of the electrolyzer, the need for an output capacitor for the converter is strongly reduced.

A significant drawback of the designed six-phase IBC is that, due to the high current stress on the output inductors, very expensive components are required. This effect can be mediated by using even more parallel phases in a modular system setup. However, the performance of this system layout needs to be carefully considered due to the risk of DCM.

Other than this cost improvement, it is found that traditional efficiency improvements such as extended duty cycles or resonant snubber circuits do not offer a significant advantage to the converter design for the considered application, due to the high output voltage and the required flexibility. Therefore, in the next chapter the six-phase IBC is taken as the standard developed design. It is compared to the rectifier-based implementation that is currently in use by **Company**, as well as the

different modular solutions outlined in this chapter, thereby giving an indication of the value of the designed converter in the considered applications.

Chapter 5

Simulation Results

5.1 Introduction

In this chapter, the converter designs considered in Chapter 4 are modeled and simulated in PLECS. Different input conditions are considered to estimate at which operating point the DC/DC converter can most efficiently power the electrolyzer. The efficiency is calculated based on the component losses included in the simulation as discussed in Section 4.6. A detailed overview of the PLECS models and component parameters used for these simulations is given in Appendix C.

The effect of the converter's output current ripple on the electrolyzer efficiency is only known qualitatively, as outlined based on scientific literature in Section 2.4. For this reason, minimizing this ripple is taken into account in the converter design to optimize the electrolyzer efficiency but given a lower priority than the converter efficiency itself.

In this chapter only the operation of the converter, without the electrolyzer efficiency, is considered. The converter efficiency is defined as the relation of the output power to the supplied input power as represented by Equation 5.1.

$$\eta = \frac{I_o \cdot U_o}{I_{in} \cdot U_{in}} \quad (5.1)$$

The different converter designs and input conditions are each modeled for a duration of one second during which the converter quickly reaches its steady-state. The results of these simulations are presented in this chapter. They are then compared to one another and the current commercial implementations in Chapter 6.

In Section 5.2 the implications on the efficiency of including a non-ideal capacitor in the converter are considered. This component is investigated separately because it is selected based on the requirement to limit the output ripple, which is considered at a lower priority than maximizing the total converter efficiency. Furthermore, in Section 4.5, ideal capacitors were modeled to study the effect and calculate the optimal output capacitance for the converter. Based on the results of simulating the converter with a non-ideal output capacitor, it is now considered whether this capacitor should be included in the final design.

Section 5.3 treats the efficiency of the six-phase IBC for the 1000 V and 700 V input cases. Since there is a difference in the selected components for these two topologies, their efficiencies are compared to conclude which implementation yields the highest best results.

The operation of the DC/DC converter directly connected to a solar farm is modeled and investigated in Section 5.4. As discussed in Section 4.2, this solar farm is modeled as a constant DC source of 658 V with a varying supply power, influencing the operating setpoint of the electrolyzer. In this way, the designed IBC is evaluated at many different power setpoints, allowing a clear efficiency curve to be generated. The yearly irradiance profile of the solar farm then determines how often the converter and electrolyzer operate at these different setpoints as is further considered in Chapter 6.

Finally, in Section 5.5 the implications of using a modular topology are considered. It is examined based on simulation results if, in addition to their beneficial cost, these topologies are able to power the electrolyzer and offer efficiency improvements compared to the single six-phase IBC.

5.2 Capacitor Losses

This section makes a final consideration of the necessity of an output capacitor in the IBC design. As stated in Section 4.5, the capacitor is selected to reduce the output current ripple. If an ideal capacitor is used, this entails a beneficial effect for the electrolyzer operation when connected to the developed DC/DC converter. However, the selected off-the-shelf capacitor is not ideal, containing a parasitic resistance and inductance, as listed in Table 4.4 in Section 4.6.

It is now considered to what degree these capacitor losses influence the total converter efficiency and ripple reduction. In the design methodology in Section 4.3 the total efficiency of the converter is given priority over the reduction of the output ripple, but it is also considered that exceptions to this priority ranking can be made if the benefit of this trade-off is sufficient.

Table 5.1 lists the efficiencies and maximum current ripples for the 1000 V and 700 V converters with and without the output capacitor selected in Section 4.5. It can be seen that the capacitor losses have almost no impact on the converter efficiency. However with the parasitic inductance of the capacitor taken into account, the reduction of the output ripple also becomes very minor.

With the operational characteristics shown in Table 5.1 it can be concluded that the inclusion of a realistic capacitor in the six-phase IBC design has a very minor impact on the performance of the converter in the considered application. Therefore, to lower the simulation time of further simulations and lower the total cost of the design, the output capacitor is omitted from the topology in further simulations considering the final six-phase IBC in this chapter.

TABLE 5.1: Efficiency and ripple comparison for converters modeled with or without the non-ideal output capacitor

Converter	No capacitor	Non-ideal capacitor
1000 V Design	$\eta = 98.57\%$ $\Delta I_{max} = 57.046$ A	$\eta = 98.56\%$ $\Delta I_{max} = 56.692$ A
700 V Design	$\eta = 99.13\%$ $\Delta I_{max} = 38.703$ A	$\eta = 99.13\%$ $\Delta I_{max} = 36.560$ A

5.3 Nominal Converter Efficiency

The nominal operating case for the converter is the LVDC grid connection at either 700 V or 1000 V powering the electrolyzer at its nominal operating point at an output voltage of 594.77 V and current of 2820.2 A. As outlined in Section 4.5, the six-phase IBC is designed slightly differently for these two voltage cases. To operate at the lower duty cycles, caused by the higher input voltage, a different diode is selected for the 1000 V topology. This has an impact on the total efficiency of the converter, as can be seen in Table 5.2.

The inverse diode of the Semitrans bidirectional IGBT module is used instead of the selected diode in the nominal 1000 V case. This IGBT module diode showcases different loss behavior than the Fast Recovery Epitaxial diode used in the 700 V implementation. Both topologies can operate the electrolyzer at the nominal setpoint. Table 5.2 shows the efficiency, the applied duty cycle and the maximum observed current ripple, achieved for these converter topologies.

TABLE 5.2: Efficiency results for the two main IBC designs operating the electrolyzer at nominal power

Converter design	U_{in} [V]	η [%]	D [-]	ΔI_{max} [A]	RF [%]
700 V topology	700	99.13	0.8555	37.023	1.31
1000 V topology	1000	98.57	0.599	56.800	2.01
1000 V topology	700	98.81	0.8552	28.042	0.994

These results show that it is most efficient to operate the electrolyzer at an input voltage of 700 V. When operating at $U_{in} = 700$ V, the topology designed for this voltage slightly outperforms the 1000 V topology, due to lower losses incurred by the smaller diode. Therefore, the 700 V six-phase IBC topology is taken as the nominal converter design for the remainder of this thesis.

5.4 Solar Farm Operation Efficiency

In addition to the nominal LVDC operating case, where the electrolyzer is operated at maximum capacity, a solar farm with a capacity of 1.7 MW is considered as an

input case for the electrolyzer and DC/DC converter. The basic operating conditions for this implementation are described in Section 4.2. As outlined there, a constant input voltage of 658 V is assumed at variable power setpoints, which are considered in steps of 100 kW. As indicated in Chapter 3, the developed electrolyzer model can calculate the required input voltage for a given input current. Consequently, this model is used to calculate the optimal current and voltage setpoints for the electrolyzer at different input powers. These setpoints are listed in Table 5.3 and provide the different output conditions for the DC/DC converter¹.

TABLE 5.3: Electrolyzer current and voltage setpoints demanded at the output of the DC/DC converter for varying power setpoints

P_{el} kW	I_{el} [A]	U_{el} [V]
85	199	426.775
100	231	423.407
200	434	460.198
300	625	479.362
400	809	494.427
500	986	506.942
600	1158	517.820
700	1326	527.545
800	1491	536.430
900	1652	544.592
1000	1810	552.203
1100	1966	559.393
1200	2119	566.178
1300	2270	572.653
1400	2418	578.810
1500	2565	584.764
1600	2709	590.458
1677.37	2820.2	594.77

Due to its lower cost and slightly improved efficiency at lower voltages, the 700 V converter topology is used at the input voltage of 658 V to provide the output power at the required current and voltage as specified in Table 5.3. Table 5.4 lists the applied duty cycle, as calculated by Equation 4.16, the converter efficiency and the normalized ripple factor for every power setpoint. Based on these results, the efficiency curve for the converter shown in Figure 5.1 is generated. The results in Table 5.4 show that the ripple factor does not display a clear increasing or decreasing trend, due to the variable inductor inductance. Additionally, the ripple factor is defined by Equation 5.2. Consequently, the increasing ripple amplitude is compensated by increasing

¹The Matlab scripts used to calculate the different electrolyzer setpoints and describe the considered behavior of the solar farm in this section are given in Appendix D

average output currents, leading to a stable ripple factor for the different setpoints.

$$RF = \frac{\Delta I_{max}}{I_o} \quad (5.2)$$

TABLE 5.4: Electrolyzer current and voltage setpoints demanded at the output of the DC/DC converter for varying power setpoints

P_{el} [kW]	I_o [A]	D [-]	η [%]	RF [%]
85	199	0.6502	99.34	1.78
100	231	0.6588	99.34	1.10
200	434	0.7013	99.37	1.75
300	625	0.7306	99.36	1.67
400	809	0.7537	99.37	1.58
500	986	0.7729	99.35	1.26
600	1158	0.7896	99.33	1.27
700	1326	0.8046	99.30	0.83
800	1491	0.8183	99.28	2.43
900	1652	0.8309	99.27	2.15
1000	1810	0.8426	99.25	0.76
1100	1966	0.8537	99.24	0.78
1200	2119	0.8642	99.21	0.82
1300	2270	0.8743	99.20	1.00
1400	2418	0.8838	99.19	1.29
1500	2565	0.8931	99.17	2.91
1600	2709	0.9019	99.17	1.25
1677.37	2820.2	0.9086	99.17	1.27

5.4.1 Reduced phase operation

At lower power operation, the components inside the converter are subjected to lower currents. It is therefore possible to differently operate the IBC using only the minimally required amount of phases. This can be done to avoid low inductor currents causing the converter to operate in DCM at low power. However, the decreasing inductance for high currents, showcased in Figure 4.5 negates this effect and leads to much higher ripple factors in this operating case. Additionally, using less interleaved phases eliminates the beneficial effect of the ripples reducing one another, further explaining the higher ripple factors presented in Table 5.5, showing the efficiency and ripple currents for minimal leg operation.

Furthermore, Table 5.5 shows that operating at higher currents in less legs leads to a lower efficiency due to increased conduction losses in the utilized phases. It can be concluded that this method of operating only the minimally required amount of phases does not offer any efficiency benefits. Although it does grant the possibility to

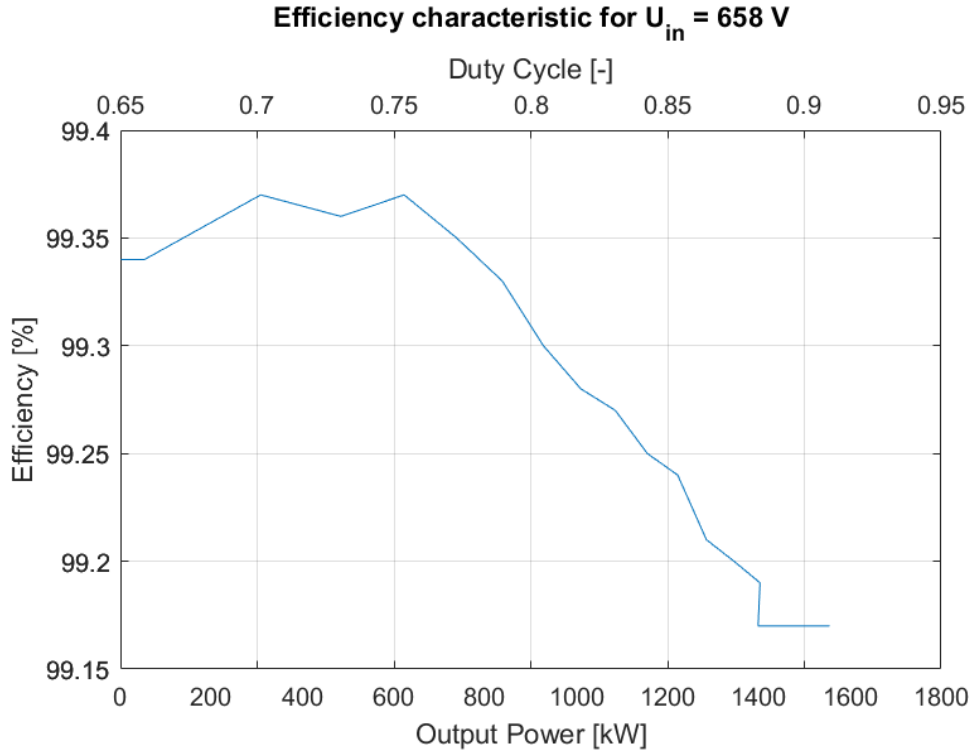


FIGURE 5.1: DC/DC converter efficiency for variable output power setpoints at the solar farm input voltage

include one fewer leg in the converter, thus allowing significant cost reductions. Since efficiency is the main priority of the design, the six-phase implementation remains as the optimal topology and this reduced phase operation is not further considered.

5.5 Modular Implementation Results

As outlined in Section 4.7, several modular designs are considered. These designs show significant cost improvements compared to the standard six-phase IBC discussed in the previous sections. It is assumed that the different parallel converters are controlled by a single signal. Table 5.6 shows the simulation results for the modular designs, operated at a 700 V input voltage. As calculated in Section 4.7, modular designs consisting of single buck converters always operate in DCM. Therefore, only modular designs consisting of two- and six-phase converter modules are simulated. These converter types have the advantage of operating at different phases at shifted frequencies, allowing the different legs in the module to prevent the total current from dropping to 0 A.

The output current waveform for the whole system is shown in Figure 5.2². This

²Due to very slow simulation speeds for these implementations, not every simulation is conducted

TABLE 5.5: Input conditions and output results for the six-phase IBC operated at minimal phase requirement

P_{el} [kW]	N	D [-]	η [%]	RF [%]
85	1	0.6513	99.15	29.87
100	1	0.6601	99.12	29.87
200	1	0.7036	98.95	28.49
300	2	0.7320	99.10	9.90
400	2	0.7555	99.03	9.63
500	2	0.7751	98.95	8.73
600	2	0.7922	98.91	6.99
700	3	0.8061	99.05	4.29
800	3	0.8200	99.01	3.99
900	3	0.8328	98.98	3.70
1000	4	0.8437	99.09	2.49
1100	4	0.8549	99.08	7.20
1200	4	0.8655	99.05	2.24
1300	4	0.8756	99.03	5.52
1400	5	0.8844	99.12	1.64
1500	5	0.8937	99.08	3.19
1600	5	0.9026	99.09	3.02
1677.37	5	0.9093	99.08	2.76

figure shows that for the different modular implementations using modules of two or six interleaved phases, the current ripple is extremely high. In system with six-phase modules the total output current repeatedly reaches 0 A. Thus this entire system operates in DCM. Furthermore, even though the input voltage and duty cycle are identical to nominal the six-phase implementation, Table 5.1 shows that the average output current and voltage, as well as the input power does not correspond to the desired electrolyzer setpoint. It is therefore concluded that a different control strategy is required to operate this modular system, in addition to taking the appropriate measures described in Section 4.7 to design the modules to avoid DCM.

TABLE 5.6: Results for the different modular implementations

Total legs	Module topology	P_{in} [kW]	I_o [A]	U_o [V]
12	Two-phase IBC	2642.0	3775.0	692.56
12	Six-phase IBC	2584.3	3696.4	684.34
24	Two-phase IBC	2579.4	3708.3	686.88
24	Six-phase IBC	2551.9	3665.8	680.87

The inclusion of an output capacitor in the modular design is unlikely to improve for the same time period. However, steady-state is achieved in all implementations at the displayed timesteps.

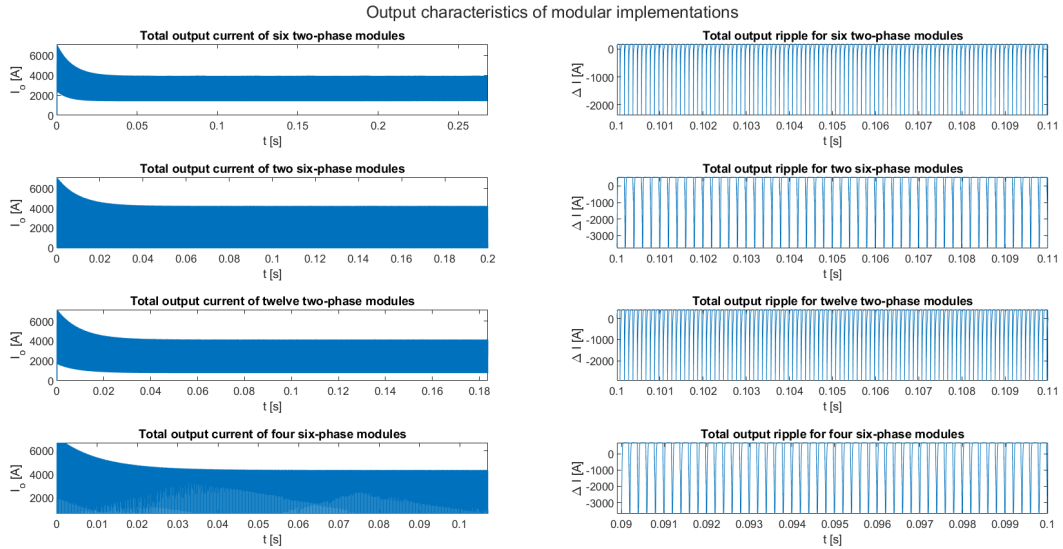


FIGURE 5.2: Total output current and ripple of the modular systems going into the the electrolyzer

this implementation. It can be calculated with Equation 4.11 that sizeable ideal capacitors would be required to reduce the voltage ripple to 1%, even for a purely resistive load, as represented in Table 5.7. However, as discussed in Section 5.2, non-ideal capacitors in parallel with the high capacitance of the electrolyzer have only a very small effect on the operation of the converter system. Therefore it is concluded that the modular design with the selected off-the-shelf components is less suitable than the single converter implementation considered in the previous sections.

TABLE 5.7: Required ideal capacitors to reduce the ripple to 1% for a purely resistive load

Total phases	Two-phase module	Six-phase module
12	27.04 mF	1.00 mF
24	348.29 μ F	12.9 μ F

5.6 Conclusion

In this chapter, the simulation results for the converter topologies considered in Chapter 4 are provided. These results are further discussed in Chapter 6, where a further analysis and conclusion on the designs is made.

In Sections 5.2 and 5.3, decisions are made on the modeled topology based on the efficiency results. This enables the simulations considered in the following sections to be based on the most efficient topologies, without having to model every design in

the many considered cases. Thus, it is concluded and further discussed in Chapter 6 that the six-phase IBC, designed for an input voltage of 700 V or below, with no output capacitor is the most efficient topology of the variations considered in Chapter 4.

Simulations at different operating points in Section 5.4 yields the efficiency curve for this converter shown in Figure 5.1. Additionally, the operating efficiency and ripple factor of the IBC converter are also considered with less and more parallel phases in Section 5.4 and Section 5.5 respectively. Still it is concluded that a six-phase implementation showcases the best characteristics for powering the **Commercial Electrolyzer** throughout its operating range.

Chapter 6

Results Discussion

6.1 Introduction

In this chapter, the results provided in Chapter 5 are closely considered and discussed. The different simulations from the previous chapter are compared to settle on a final converter design in Section 6.2, based on the reported efficiency, output ripple and costs.

Section 6.3 considers the final converter design in a system-wide perspective and provides the total efficiency of hydrogen production in the considered applications. The designed topology is then compared to the standard inverter-based case. The difference in hydrogen production, efficiency and cost are compared to consider whether the designed system succeeds in providing an efficient alternative for powering the electrolyzer to produce renewable hydrogen.

This section also considers the irradiance profiles for the solar farm case for two different geographical locations. This way, the amount of hydrogen produced in the considered locations can be compared, linking back to the consideration made in Section 2.2, where it is considered whether generating hydrogen in regions with high RES potential would be a valuable application.

6.2 Final Topology Design

6.2.1 Topology efficiency

For the operation of the electrolyzer at nominal capacity, input voltages of 700 V and 1000 V have been considered. Due to the lower duty cycles at a higher input voltage, the freewheeling diodes are replaced with the diodes from the IGBT modules in the 1000 V design. As a consequence of the higher conduction and switching losses showcased by these IGBT diodes, the topology made for 1000 V input operation achieves a lower efficiency than the 700 V topology. It thus suffers a trade-off in efficiency for the flexibility to operate at higher input voltages.

Furthermore, in Section 4.5, a capacitor is selected based on calculations considering an ideal component. In Section 5.2 however, the simulation results show that

the effect on the ripple factor of this capacitor is very small, due to the parasitic inductance of the capacitor and the capacitance of the electrolyzer. Since there is little benefit in including this component in the six-phase IBC, it is omitted from the design to save on final cost of the topology and speed up further simulations.

From the simulations in Section 5.4 the efficiency curve for the converter can be derived. It can be seen that it achieves its peak efficiency of 99.37% when operating at a duty cycle of either 0.7013 or 0.7537. From this, it can be assumed that the optimal input voltage for powering the electrolyzer at rated capacity would be between $U_{in} = 789.13$ V and $U_{in} = 848.10$ V. However the diode limitations of $I_{F,nom} = 77$ A limits the duty cycle for maximum power operation to $D = 0.836$. As a final comparison to achieve a definitive converter design, the efficiencies for the 1000 V and 700 V topologies operated at these respective optimal duty cycles are listed in Table 6.1. The required input voltage is calculated taking the losses into account to achieve the duty cycle of $D = 0.7537$ and $D = 0.836$ respectively.

TABLE 6.1: Input voltage, efficiency and ripple factor for the converter topologies, operating at the optimal duty cycle at nominal capacity

Topology	D [-]	U_{in} [V]	η [%]	RF [%]
1000 V	0.7537	796.44	98.73	1.59
700 V	0.836	716.44	99.12	0.81

It can be seen in Table 6.1 that operating at these duty cycles which are found to be optimal in Figure 5.1 does not yield efficiency improvements for the nominal operation of the electrolyzer, compared to the setpoints considered in Table 5.2. Therefore, the six-phase IBC designed for 700 V is still considered as the optimal converter design for the considered applications. Its final design model is depicted in Figure 6.1 with the selected components listed. With these components, the final cost for the converter becomes €11017.02.

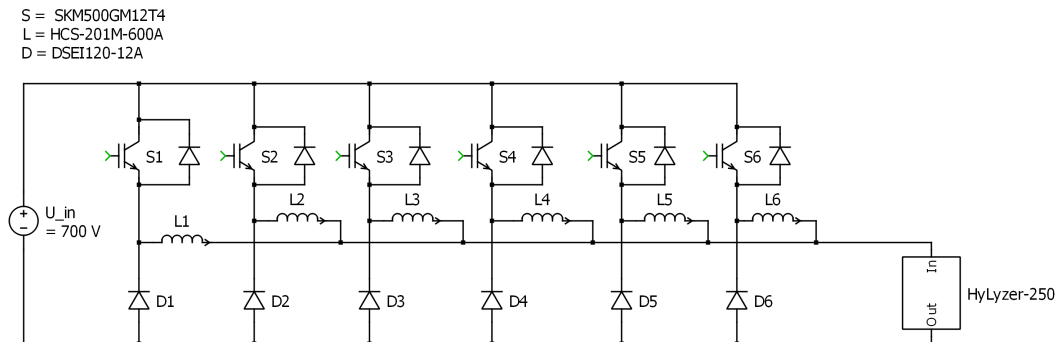


FIGURE 6.1: Final six-phase IBC design

6.3 Total System Efficiency

In this section the DC/DC converter is integrated in the considered operating cases. The efficiency results reported in Chapter 5 are combined with the voltage efficiency of the electrolyzer given by Equation 2.11 calculated with the electrolyzer model from Chapter 3. The total system efficiencies are then compared to the operating case using a rectifier to power the electrolyzer from an AC system. This rectifier has a reported efficiency of 97%¹.

6.3.1 LVDC operation

As discussed in Section 6.2 the most efficient result for operating the electrolyzer at nominal power is given in Table 5.2 for an input voltage of 700 V at an efficiency of $\eta = 99.13\%$. At this nominal power, the efficiency of the electrolyzer itself is given by Equation 6.1.

$$\eta_{el} = \frac{V_{oc}}{V_{el}} = 51.672\% \quad (6.1)$$

$$\eta_{DC} = \eta_c \cdot \eta_{el} = 51.22\% \quad (6.2)$$

Consequently, the system efficiency from the perspective of the LVDC grid is given by Equation 6.2. However, since the rectifier step is not taken into account to provide DC energy from an external AC connection, this efficiency only applies to power directly generated and injected into the DC grid.

The case where the electrolyzer is fully powered by DC renewable generation is further considered in the next subsection, where the variation of RES is considered to study its impact on the system efficiency. The efficiency of the electrolyzer powered by a LVDC grid with an AC connection, to stably operate at nominal capacity of the electrolyzer, is given by Equation 6.3².

$$\eta_{tot} = \frac{(\eta_{rect} \cdot \eta_c \cdot \eta_{el}) \cdot P_{AC} + (\eta_c \cdot \eta_{el}) \cdot P_{DC}}{P_{AC} + P_{DC}} \quad (6.3)$$

Therefore, to achieve a more efficient performance than simply using the AC-connected rectifier, which achieves a system efficiency of 50.12%. At least 28.38% of the power on the DC grid must be directly injected by DC renewable sources.

6.3.2 Solar farm system efficiency

In Section 5.4 the efficiency of the designed DC/DC converter for different operating setpoints is listed. This is done to represent the different power levels provided by a utility-scale solar farm meant to power the electrolyzer. As discussed in Chapter 2, the efficiency of an electrolyzer increases with decreasing power. By means of

¹The specific efficiency of this rectifier at different operating points is not known. Therefore, this peak efficiency of 97% is taken for any operating point of the rectifier, thus serving as an upper limit for the efficiency of the commercial rectifier-based operation.

²The same commercial rectifier is assumed for feeding the DC grid, so η_{rect} is also taken as 97%.

the electrolyzer model from Chapter 3, its efficiency is calculated for the considered power setpoint provided by the solar farm. The total resulting efficiency, combining the DC/DC converter and electrolyzer is listed in Table 6.2. Additionally, this table provides the hydrogen output achieved when operating the electrolyzer at each considered power setpoint, as well as the amount of hours these setpoints could be achieved based on data from renewables.ninja [81–83]. For these irradiance profiles the location of Energyville in Belgium and the location at the Ouarzazate solar farm in Morocco are used. In both cases a 1.7 MW south-facing solar farm at a tilt of 30° is considered.

TABLE 6.2: System results for PV hydrogen

P_{PV} [kW]	Capacity hours BE	Capacity hours MA	Hydrogen output [Nm ³ /h]	η_{el} [%]	η_{tot} [%]
0	5325	4855	0	0	0
85.56	36	35	17.64	68.94	68.48
100.66	299	118	20.48	68.22	67.77
201.27	463	133	38.47	64.79	64.38
301.93	325	228	55.40	62.58	62.18
402.54	231	269	71.72	60.94	60.55
503.27	295	98	87.41	59.63	59.24
604.05	224	186	102.65	58.53	58.14
704.93	239	274	117.55	57.58	57.17
805.80	233	244	132.17	56.73	56.32
906.62	204	139	146.45	55.97	55.56
1007.56	218	277	160.45	55.28	54.87
1108.42	198	335	174.28	54.64	54.23
1209.6	212	291	187.84	54.05	53.62
1310.48	173	437	201.23	53.50	53.07
1411.43	101	439	214.35	52.98	52.05
1512.55	8	331	227.38	52.49	52.05
1613.39	0	91	240.25	51.03	51.59
1691.04	0	4	250.87	51.67	51.24

With these results the total hydrogen production and energy efficiency can be calculated for both locations, as listed in Table 6.3. The results show that, due to the higher efficiency of the electrolyzer at lower powers, a higher total energy efficiency is achieved when the electrolyzer is connected to a PV plant in Belgium. However, over the course of an entire year, this electrolyzer would generate 40% less hydrogen than one connected to a PV farm in Morocco, where more energy is generated due to better conditions for PV generation. This example showcases the point made in Section 2.2 that generating large amounts of hydrogen is accompanied by low energetic efficiency and is most effective in regions with beneficial conditions for RES, provided that the cost of electricity is low enough to justify these energy losses.

Similarly to the nominal case operation, the comparison is made here to operating the system with a standard rectifier solution. The electrolyzer input powers considered in Table 5.4 result in the PV generation power listed in Table 6.2. To use this energy in a rectifier-based implementation, the DC power must first be converted to AC before being rectified back to DC, thus undergoing two conversion steps with an efficiency of 97%. The total power going into the electrolyzer, for the same PV

TABLE 6.3: Total hydrogen output and energy efficiency for PV based hydrogen production in different locations

Location	$E_{PV,tot}$ [MWh]	Hydrogen output [Nm ³]	η_{tot} [%]
Belgium	2219.3	364280	56.31
Morocco	3745.2	590190	54.31

conditions as considered in the DC/DC case, is listed in Table 6.4. This results in different setpoints for the electrolyzer, as well as a different system efficiency and hydrogen production rate at every power setpoint³. Table 6.5 shows the total energy

TABLE 6.4: Electrolyzer setpoints and efficiency for inverter-rectifier PV farm connection

P_{el} [kW]	I_{el} [A]	U_{el} [V]	η_{el} [%]	η_{tot} [%]
94.72	219	430.35	68.48	64.43
189.37	413	457.77	65.08	61.23
284.09	595	476.64	62.89	59.17
378.75	770	491.44	61.26	57.64
473.53	939	503.77	59.95	56.41
568.35	1104	514.52	58.86	55.38
663.27	1265	524.10	57.91	54.49
758.18	1422	532.79	57.07	53.70
853.04	1577	540.85	56.32	52.99
948.01	1728	548.30	55.63	52.34
1042.9	1877	555.33	55.00	51.75
1138.1	2024	561.99	54.41	51.20
1233.0	2169	568.35	53.86	50.68
1328.0	2311	574.38	53.35	50.20
1423.2	2452	580.80	52.86	49.74
1518.0	2591	585.80	52.40	49.31
1591.1	2696	589.95	52.07	48.99

efficiency and hydrogen production for the entire year. The PV energy is the slightly lower than in the DC/DC converter case since the PV power setpoint of 85.56 kW results in only 80.51 kW at the electrolyzer and thus falls below the minimum rated power. The resulting hydrogen production is considerably lower in both locations of the production. As expected, the total system energy efficiency is lower in the inverter-rectifier case, resulting in 57.92 and 92.88 MWh of additional lost energy for the Belgian and Moroccan cases respectively.

³Due to the low conversion efficiency, the solar power setpoints, originally at 85.56 kW fall below the minimum electrolyzer capacity of 5%. Therefore, these 36/35 hours of renewable generation do not contribute to the total generation of hydrogen in this case.

TABLE 6.5: Total hydrogen output and energy efficiency for PV based hydrogen production in different locations

Location	$E_{PV,tot}$ [MWh]	Hydrogen output [Nm ³]	η_{tot} [%]
Belgium	2216.3	346910	53.68
Morocco	3742.2	562970	51.82

6.4 Conclusion

In this chapter, the results from the simulations conducted in Chapter 5 are considered within the specific applications outlined for this thesis. The final DC/DC converter topology, resulting from the design in Chapter 4 and calculations in Chapter 5 is discussed. For nominal electrolyzer operation on a LVDC grid, the designed IBC outperforms a rectifier-based implementation if at least 28.38% of the power is generated by local DC sources. For an electrolyzer directly connected to a solar farm, either in Belgium or in Morocco, it is shown that using a DC/DC converter can save up to 57.92 or 92.88 MWh per year.

Since cheaper, modular implementations are not found to be feasible, based on the simulations in Chapter 5, the final converter cost amounts to €11017.02. The value of the DC/DC converter implementation can be calculated by comparing the costs of the two converter types and factoring in the value of the energy savings which are calculated and presented in this chapter. However, the exact cost for the high power rectifier, used as the reference case in this thesis, as well as the energy costs in the different operating cases are not known. Therefore, no definitive conclusion can be made on the value of the design on this thesis. It is however clear from the results discussed in this chapter that the use of a DC/DC converter has significant potential for energy savings when generating hydrogen from renewable sources.

Chapter 7

Conclusion

7.1 Contribution to Existing Research

In order to limit and reduce climate change, the energy system needs to transform to a more renewable and more efficient system. From the first part of the literature study, it can be concluded that the ambitions to include hydrogen in this new energy system are high. Furthermore, this energy carrier has the potential to allow decarbonization in certain applications and sectors where the potential for electrification is limited or saturated. Therefore, this thesis focused on improving the efficiency of generating clean hydrogen. In this regard it expanded on existing research and practical applications by designing a DC/DC converter based on commercial components to power a high-power industrial scale electrolyzer. The methodology used for this design allowed a basic cost calculation and simulations that resulted in a total converter efficiency. These calculations and the focus on realistic and possible commercial applications allow producers of electrolyzers like **Company** to consider these more efficient implementations and improve the efficiency and cost of hydrogen production in the future.

7.2 Evaluation of the Research Questions

Achieving this efficiency improvement was approached via four research questions set out in Section 1.3, repeated here in a shortened version for convenience:

- **Q1:** How to efficiently operate an electrolyzer?
- **Q2:** Which DC/DC converter topologies are suitable?
- **Q3:** How does the selected DC/DC converter perform?
- **Q4:** Can further improvements to the system efficiency be made?

An answer to these questions is provided in the different sections of this thesis. Chapter 3 treats the energetic working principles of the electrolyzer and outlines the build-up of a mathematical model from scientific literature, which allows the

electrolyzer efficiency to be calculated based on the applied power setpoint and operating conditions. Although it is not the aim of this thesis to improve the efficiency of the electrolysis process itself, taking the characteristics of the electrolyzer into account resulted in useful requirements for the DC/DC converter design, such as the output current and voltage setpoint, as well as the low ripple requirement. However, the calculation of the electrolyzer efficiency characteristic also proved that a high hydrogen output leads to a lower electrolyzer and system efficiency, as showcased by the results from Tables 6.3-6.5, where a lower hydrogen output results in a higher total energy efficiency. This underscores the considerations made in Section 2.2 of the literature review that electrolysis is inherently an energy-inefficient process and should thus be considered primarily for essential applications.

The answer to the first research question is provided in the form of the Simulink model, constructed in Chapter 3, based on scientific literature on the working principles of PEM electrolyzers. This model allowed the calculation of the optimal power setpoints and losses of the electrolyzer. Consequently the DC/DC converter was optimally designed for providing the electrolyzer's nominal power. The model also provides the optimal output power setpoints for the solar farm case study, considered in Sections 5.4 and 6.3, assuring that the electrolyzer is operated at its maximum efficiency for any given input power.

The basic converter topologies for operating the considered electrolyzer system are outlined based on scientific literature in Section 2.6. The main differences in the converter requirements in this thesis, compared to the topologies commonly discussed in literature, are the high output current requirement and high output voltage. Therefore, a full-bridge topology and interleaved buck converter are considered as contenders for the final design and further discussed in Chapter 4. The design methodology and requirements outlined in this chapter, as well as the calculations on the specific topologies in Section 4.4, resulted in the IBC as the converter topology of choice for the applications considered in this thesis, thus providing an answer to the second research question.

Research question 3 aims to analyse the performance of the converter design and compare it to the commercial rectifier-based implementation. This was done in this thesis by simulating the converter in different implementations and application use cases in PLECS to come to the results presented and discussed in Chapters 5 and 6. These results allowed the converter design to be further refined and generated a clear overview of the achieved efficiency in the different operating cases. An efficiency curve for the DC/DC converter, operating at an input voltage of 658 V was derived and displayed in Figure 5.1.

The total system efficiency, resulting from the use of a DC/DC converter connection to a LVDC grid, was then compared to the standard operating case in Section 6.3. These analyses showed that using an electrolyzer connected to a LVDC grid results in efficiency improvements if at least 28.38% of the total energy consists of DC renewable energy, in the form of local PV generation, that is directly injected into this system. Furthermore, this section also showed that to generate hydrogen directly from solar power, either in Belgium or in a region with more beneficial PV conditions, the use of a direct DC connection results in a higher production rate

compared to the case where an AC step is included. It is therefore concluded that the answer to the third research question is provided in these chapters and that the results show that the considered converter and application cases offer the potential for efficiency improvements in the generation of renewable hydrogen.

The final research question concerned the improvement of the standard converter topology selected in Chapter 4. As discussed in Section 4.7, several design improvements are presented in literature but for the application of powering the **Commercial Electrolyzer** electrolyzer, these improvements would not lead to efficiency improvements. Additionally, the implementation of soft-switching circuits is also considered but ultimately not implemented due to the frequency specific nature of these circuits limiting the flexibility of the converter. Different implementations were also considered with the aim of saving on the converter costs. Modular implementations using many parallel single-phase, two-phase or six-phase buck converter modules were considered in order to reduce the current stress and the cost of the output inductors. However, these implementations proved not to be suited for the application considered in this thesis, due to the high ripple and the occurrence of DCM. Finally it was investigated whether it would be possible and more cost effective to operate the converter with less than six interleaved phases but the results in Table 5.5 proved that this only led to additional losses.

With regards to the fourth research question it can consequently be stated that although several alternative and improved topologies were considered, these did not outperform the standard six-phase interleaved circuit. As a result, the disadvantage of this topology, mainly in the high cost needs to be accepted in this implementation and may form a barrier to its commercial implementation. Reducing the cost of this solution by designing a modular topology, accompanied by a control strategy to properly power the electrolyzer can be one of the main pathways for further research on this topic.

7.3 Further Research

Reducing the cost and improving the commercial viability of the designed converter and LVDC grid implementation by further developing a modular converter approach is one pathway for further research. The effects of DCM at low and high power operating conditions can be investigated in order to developing a proper control strategy to make a modular implementation more viable. Additionally, with the requirements for the DC/DC converter components outlined in this thesis, it would also be possible to conduct additional studies into finding or developing more efficient or less expensive components. In this thesis, a single online store is used as the main source of components. Further scientific research or separate suppliers of industrial grade components may lead to a different and possibly more efficient or cost effective result for the converter. However, the requirements and limitations outlined in this thesis would still be applicable to these components. Different converter requirements can be achieved by changing the input condition assumptions. For example, operating the industrial electrolyzer from a MV- or HVDC input grid can be considered to

investigate if this would result in additional efficiency benefits.

One of the specifications for the converter design is given by the requirement of a low output ripple for the electrolyzer efficiency. As discussed in Section 5.2, the effect of the ripple amplitude and frequency on the electrolyzer efficiency is not quantified in scientific literature, leading to uncertainty in deciding the allowed output ripple. For this reason the efficiency of the DC/DC converter is given a higher priority than the reduction of the output ripple in the design methodology in Section 4.3. Consequently, no output capacitor was ultimately included in the IBC design. If through further research the effects of the ripple current and voltage on the efficiency of an electrolyzer, comparable to the **Commercial Electrolyzer**, are quantified, this trade-off can be made in a more rigorous way. More extensive research could then be conducted in the specific effect and requirement of including a realistic output capacitor.

A different field of additional research lies in corroborating the electrolyzer model used in the electrical simulations in this thesis. Whereas the mathematical Simulink model for calculating the optimal power setpoint conditions has a strong scientific support, the electrical model shown in Figure 3.7 is constructed based on existing dynamic models for smaller scale electrolyzers and operational data provided by **Company**. Testing this model to measured electrical behavior of the **Commercial Electrolyzer** could lead to further improvements or an experimental validation, allowing the electrolyzer to be accurately electrically modeled. One assumption that was made in the electrolyzer model is the assumption of a Faradaic efficiency of 100%, which is supported by most literature [58–61], but does have an impact on the calculation of the current setpoint in Equation 4.11 and on the hydrogen production results in Section 6.3. Further characterizing and taking into account this energy loss, which is linked to the characterization of the ripple effect [64], may also lead to more detailed and realistic results for the calculation of electrolyzer current setpoints and system-wide hydrogen production efficiency.

Finally, the calculations regarding the converter efficiency and electrolyzer operation in this thesis are all based on models and simulations. Some assumptions presented in Table 3.1 were made regarding the electrolyzer in the model described in Chapter 3. Additionally, although the DC/DC converter is modeled based on realistic components, additional losses such as ohmic wire losses, or parasitic capacitances or inductances on all components may yet lead to different efficiency results than those found by the simulations in this thesis. Furthermore, practical aspects such as transient behavior, safety and reliability were not considered in the design and modeling of the converter. Practical tests or more detailed simulations can therefore be conducted to refine the results concluded in this thesis.

Bibliography

- [1] European Commission. *Communication from the Commission to the European Parliament, the Council, the European Economic and Social Committee of the Regions: A hydrogen strategy for a climate-neutral Europe, COM(2020) 301 final*. https://ec.europa.eu/energy/sites/ener/files/hydrogen_strategy.pdf. 2020.
- [2] IRENA. *Global Renewables Outlook. Energy transformation 2050*. Tech. rep. Abu Dhabi, UAE, 2020.
- [3] BloombergNEF. *Hydrogen Economy Outlook. Key messages*. Tech. rep. March 2020.
- [4] International Energy Agency. *The Future of Hydrogen. Seizing today's opportunities*. Tech. rep. FR, June 2019.
- [5] Daniel L. Gerber et al. „A simulation-based efficiency comparison of AC and DC power distribution networks in commercial buildings”. In: *Applied Energy* 210 (January 2018), pp. 1167–1187. ISSN: 03062619. DOI: [10.1016/j.apenergy.2017.05.179](https://doi.org/10.1016/j.apenergy.2017.05.179).
- [6] Guy Allee and William Tschudi. „Edison redux: 380 Vdc brings reliability and efficiency to sustainable data centers”. In: *IEEE Power and Energy Magazine* 10.6 (2012), pp. 50–59. ISSN: 15407977. DOI: [10.1109/MPE.2012.2212607](https://doi.org/10.1109/MPE.2012.2212607).
- [7] Scott Backhaus et al. *Los Alamos National Laboratory DC Microgrids Scoping Study-Estimate of Technical and Economic Benefits*. Tech. rep. 2015.
- [8] Fuel Cells and Hydrogen Joint Undertaking. *Hydrogen Roadmap Europe, A Sustainable Pathway for the European Energy Transition*. Tech. rep. Charleroi, BE, January 2019.
- [9] Bert Droste-Franke et al. *Balancing Renewable Electricity. Energy Storage, Demand Side Management, and Network Extension from an Interdisciplinary Perspective*. Ed. by Carl Friedrich Gethmann and Franziska Mosthaf. Vol. 40. Ethics of Science and Technology Assessment. Springer, 2012.
- [10] Usman Salahuddin, Haider Ejaz, and Naseem Iqbal. „Grid to wheel energy efficiency analysis of battery- and fuel cell-powered vehicles”. In: *International Journal of Energy Research* 42.5 (April 2018), pp. 2021–2028. ISSN: 1099114X. DOI: [10.1002/er.3994](https://doi.org/10.1002/er.3994).

- [11] *Powerwall*. Tesla Powerwall 2. Tesla. 2019. URL: https://www.tesla.com/sites/default/files/pdfs/powerwall/Powerwall%5C%202_AC_Datasheet_en_northamerica.pdf (visited on 05/25/2022).
- [12] Günther Brauner. *System Efficiency by Renewable Electricity. Strategies for Efficient Energy Supply until 2050*. Ed. by Daniel Frölich. Springer, 2022.
- [13] Shafiqur Rehman, Luai M. Al-Hadhrani, and Md Mahbub Alam. *Pumped hydro energy storage system: A technological review*. 2015. DOI: [10.1016/j.rser.2014.12.040](https://doi.org/10.1016/j.rser.2014.12.040).
- [14] IEC. *Electrical Energy Storage White Paper*. Tech. rep. Geneva, CH, December 2011.
- [15] Subodh Kharel and Bahman Shabani. „Hydrogen as a long-term large-scale energy storage solution to support renewables”. In: *Energies* 11.10 (2018). ISSN: 19961073. DOI: [10.3390/en11102825](https://doi.org/10.3390/en11102825).
- [16] K. A. Kavadias, D. Apostolou, and J. K. Kaldellis. „Modelling and optimisation of a hydrogen-based energy storage system in an autonomous electrical network”. In: *Applied Energy* 227 (October 2018), pp. 574–586. ISSN: 03062619. DOI: [10.1016/j.apenergy.2017.08.050](https://doi.org/10.1016/j.apenergy.2017.08.050).
- [17] Jason Moore and Bahman Shabani. *A critical study of stationary energy storage policies in Australia in an international context: The role of hydrogen and battery technologies*. 2016. DOI: [10.3390/en9090674](https://doi.org/10.3390/en9090674).
- [18] Felipe Ignacio Gallardo et al. „A Techno-Economic Analysis of solar hydrogen production by electrolysis in the north of Chile and the case of exportation from Atacama Desert to Japan”. In: *International Journal of Hydrogen Energy* 46.26 (April 2021), pp. 13709–13728. ISSN: 03603199. DOI: [10.1016/j.ijhydene.2020.07.050](https://doi.org/10.1016/j.ijhydene.2020.07.050).
- [19] John Andrews and Bahman Shabani. „Re-envisioning the role of hydrogen in a sustainable energy economy”. In: *International Journal of Hydrogen Energy* 37.2 (January 2012), pp. 1184–1203. ISSN: 03603199. DOI: [10.1016/j.ijhydene.2011.09.137](https://doi.org/10.1016/j.ijhydene.2011.09.137).
- [20] Johan Driesen. *Transport & Energy System Integration. “alternative” fuels*. https://p.cygnus.cc.kuleuven.be/bbcswebdav/pid-30058749-dt-content-rid-307705644_2/courses/B-KUL-H04C8a-2122/alternative%20fuels.pdf. 2019.
- [21] Ivan Mareev, Jan Becker, and Dirk Uwe Sauer. „Battery dimensioning and life cycle costs analysis for a heavy-duty truck considering the requirements of long-haul transportation”. In: *Energies* 11.1 (January 2018). ISSN: 19961073. DOI: [10.3390/en11010055](https://doi.org/10.3390/en11010055).
- [22] Heikki Liimatainen, Oscar van Vliet, and David Aplyn. „The potential of electric trucks – An international commodity-level analysis”. In: *Applied Energy* 236 (February 2019), pp. 804–814. ISSN: 03062619. DOI: [10.1016/j.apenergy.2018.12.017](https://doi.org/10.1016/j.apenergy.2018.12.017).

- [23] C. E. Thomas. „Fuel cell and battery electric vehicles compared”. In: *International Journal of Hydrogen Energy* 34.15 (August 2009), pp. 6005–6020. ISSN: 03603199. DOI: [10.1016/j.ijhydene.2009.06.003](https://doi.org/10.1016/j.ijhydene.2009.06.003).
- [24] Patrick Moriarty and Damon Honnery. „Prospects for hydrogen as a transport fuel”. In: *International Journal of Hydrogen Energy* 44.31 (June 2019), pp. 16029–16037. ISSN: 03603199. DOI: [10.1016/j.ijhydene.2019.04.278](https://doi.org/10.1016/j.ijhydene.2019.04.278).
- [25] Simon T. Thompson et al. „Direct hydrogen fuel cell electric vehicle cost analysis: System and high-volume manufacturing description, validation, and outlook”. In: *Journal of Power Sources* 399 (September 2018), pp. 304–313. ISSN: 03787753. DOI: [10.1016/j.jpowsour.2018.07.100](https://doi.org/10.1016/j.jpowsour.2018.07.100).
- [26] Yusuf Bicer and Ibrahim Dincer. „Life cycle evaluation of hydrogen and other potential fuels for aircrafts”. In: *International Journal of Hydrogen Energy* 42.16 (April 2017), pp. 10722–10738. ISSN: 03603199. DOI: [10.1016/j.ijhydene.2016.12.119](https://doi.org/10.1016/j.ijhydene.2016.12.119).
- [27] Yusuf Bicer and Ibrahim Dincer. „Clean fuel options with hydrogen for sea transportation: A life cycle approach”. In: *International Journal of Hydrogen Energy* 43.2 (2018), pp. 1179–1193. ISSN: 03603199. DOI: [10.1016/j.ijhydene.2017.10.157](https://doi.org/10.1016/j.ijhydene.2017.10.157).
- [28] FEBEG. *Statistieken gas. Import en consumptie van aardgas in België*. 2022. URL: <https://www.febeg.be/statistieken-gas> (visited on 04/29/2022).
- [29] Fluxys. *Natural gas & green gas. Lecture KU-Leuven*. https://p.cygnus.cc.kuleuven.be/bbcswebdav/pid-30121351-dt-content-rid-323458400_2/courses/B-KUL-H06P1a-2122/2022%20-%20gas%20grid%20training%2028part%201%29.pdf. April 2022.
- [30] Anselm Eisentraut and Adam Brown. *Heating Without Global Warming. Market Developments and Policy Considerations for Renewable Heat*. Tech. rep. Paris, FR: International Energy Agency, April 2014.
- [31] Richard Hoggett, Judith Ward, and Catherine Mitchell. *Heat in Homes: customer choice on fuel and technologies Study for Scotia Gas Networks Energy Policy Group Heat in Homes: customer choice on fuel and technologies*. Tech. rep. 2011. URL: www.exeter.ac.uk/epg.
- [32] Fluvius. *Premie warmtepomp*. 2022. URL: <https://www.fluvius.be/nl/thema/premies/premies-voor-huishoudelijke-klanten/premie-warmtepomp> (visited on 04/30/2022).
- [33] Vlaamse overheid. *Geen aardgasaansluitingen meer bij nieuwe grote projecten*. 2022. URL: <https://www.vlaanderen.be/nieuwe-verwarmingsinstallatie-kiezen/geen-aardgasaansluitingen-meer-bij-nieuwe-grote-projecten#q-5a16d194-4404-4c48-9b78-e2bdfa8a5a4c> (visited on 04/30/2022).
- [34] A Uytterhoeven et al. *Hybrid heat pump scenarios as a transition towards more flexible buildings*. Tech. rep. Liege: KULeuven, December 2018.

- [35] International Energy Agency. *Energy Technology Perspectives 2012. Pathways to a Clean Energy System*. Tech. rep. Paris, FR, June 2012.
- [36] Dries Haeseldonckx and William D’haeseleer. „The use of the natural-gas pipeline infrastructure for hydrogen transport in a changing market structure”. In: *International Journal of Hydrogen Energy* 32.10-11 (July 2007), pp. 1381–1386. ISSN: 03603199. DOI: [10.1016/j.ijhydene.2006.10.018](https://doi.org/10.1016/j.ijhydene.2006.10.018).
- [37] J Pangborn, M Scott, and J Sharer. *TECHNICAL PROSPECTS FOR COMMERCIAL AND RESIDENTIAL DISTRIBUTION AND UTILIZATION OF HYDROGEN*. Tech. rep. 1977, p. 431445.
- [38] Mahdi Deymi-Dashtebayaz et al. „Investigating the effect of hydrogen injection on natural gas thermo-physical properties with various compositions”. In: *Energy* 167 (January 2019), pp. 235–245. ISSN: 03605442. DOI: [10.1016/j.energy.2018.10.186](https://doi.org/10.1016/j.energy.2018.10.186).
- [39] Engineering ToolBox. *Fuels-Higher and Lower Calorific Values*. 2003. URL: https://www.engineeringtoolbox.com/fuels-higher-calorific-values-d_169.html (visited on 04/30/2022).
- [40] Weijia Liu, Fushuan Wen, and Yusheng Xue. *Power-to-gas technology in energy systems: current status and prospects of potential operation strategies*. May 2017. DOI: [10.1007/s40565-017-0285-0](https://doi.org/10.1007/s40565-017-0285-0).
- [41] Amela Ajanovic and Reinhard Haas. *On the long-term prospects of power-to-gas technologies*. January 2019. DOI: [10.1002/wene.318](https://doi.org/10.1002/wene.318).
- [42] Max Wei, Colin A. McMillan, and Stephane de la Rue du Can. *Electrification of Industry: Potential, Challenges and Outlook*. December 2019. DOI: [10.1007/s40518-019-00136-1](https://doi.org/10.1007/s40518-019-00136-1).
- [43] International Energy Agency. *Global Hydrogen Review 2021*. Tech. rep. FR, November 2021.
- [44] International Energy Agency. *Iron and Steel Technology Roadmap. Towards more sustainable steelmaking*. Tech. rep. FR, October 2020.
- [45] ArcelorMittal. *Climate Action in Europe, Our carbon emissions reduction roadmap: 30% by 2030 and carbon neutral by 2050*. Tech. rep. Luxembourg, May 2020.
- [46] R. R. Wang et al. *Hydrogen direct reduction (H-DR) in steel industry—An overview of challenges and opportunities*. December 2021. DOI: [10.1016/j.jclepro.2021.129797](https://doi.org/10.1016/j.jclepro.2021.129797).
- [47] „BASF preents roadmap to climate neutrality”. In: *www.basf.com* (March 2021). URL: <https://www.basf.com/global/en/who-we-are/sustainability/whats-new/sustainability-news/2021/basf-presents-roadmap-to-climate-neutrality.html>.
- [48] Mamoon Rashid et al. *Hydrogen Production by Water Electrolysis: A Review of Alkaline Water Electrolysis, PEM Water Electrolysis and High Temperature Water Electrolysis*. Tech. rep. 3. 2015, pp. 2249–8958.

- [49] Andrea Mazza, Ettore Bompard, and Gianfranco Chicco. *Applications of power to gas technologies in emerging electrical systems*. September 2018. DOI: [10.1016/j.rser.2018.04.072](https://doi.org/10.1016/j.rser.2018.04.072).
- [50] J.H. Russel, L.J. Nuttall, and A.P. Fickett. „Hydrogen generation by solid polymer electrolyte water electrolysis”. In: *American Chemical Society Division of Fuel Chemistry Preprints* 18 (1973), pp. 24–40.
- [51] Marcelo Carmo et al. *A comprehensive review on PEM water electrolysis*. April 2013. DOI: [10.1016/j.ijhydene.2013.01.151](https://doi.org/10.1016/j.ijhydene.2013.01.151).
- [52] S. Shiva Kumar and V. Himabindu. „Hydrogen production by PEM water electrolysis – A review”. In: *Materials Science for Energy Technologies* 2.3 (December 2019), pp. 442–454. ISSN: 25892991. DOI: [10.1016/j.mset.2019.03.002](https://doi.org/10.1016/j.mset.2019.03.002).
- [53] Anne Hauch et al. „Highly efficient high temperature electrolysis”. In: *Journal of Materials Chemistry* 18.20 (2008), pp. 2331–2340. ISSN: 09599428. DOI: [10.1039/b718822f](https://doi.org/10.1039/b718822f).
- [54] W Doenitz et al. *HYDROGEN PRODUCTION BY HIGH TEMPERATURE ELECTROLYSIS OF WATER VAPOUR*. Tech. rep. 1980, pp. 55–63.
- [55] M. A. Laguna-Bercero. *Recent advances in high temperature electrolysis using solid oxide fuel cells: A review*. April 2012. DOI: [10.1016/j.jpowsour.2011.12.019](https://doi.org/10.1016/j.jpowsour.2011.12.019).
- [56] Seyedmehdi Sharifian, Neda Asasian Kolor, and Michael Harasek. „Transient simulation and modeling of photovoltaic-PEM water electrolysis”. In: *Energy Sources, Part A: Recovery, Utilization and Environmental Effects* 42.9 (May 2020), pp. 1097–1107. ISSN: 15567230. DOI: [10.1080/15567036.2019.1602220](https://doi.org/10.1080/15567036.2019.1602220).
- [57] Z. Abdin, C. J. Webb, and E. Maca Gray. „Modelling and simulation of a proton exchange membrane (PEM) electrolyser cell”. In: *International Journal of Hydrogen Energy* 40.39 (October 2015), pp. 13243–13257. ISSN: 03603199. DOI: [10.1016/j.ijhydene.2015.07.129](https://doi.org/10.1016/j.ijhydene.2015.07.129).
- [58] R. García-Valverde et al. „Optimized photovoltaic generator-water electrolyser coupling through a controlled DC-DC converter”. In: *International Journal of Hydrogen Energy* 33.20 (October 2008), pp. 5352–5362. ISSN: 03603199. DOI: [10.1016/j.ijhydene.2008.06.015](https://doi.org/10.1016/j.ijhydene.2008.06.015).
- [59] Frano Barbir. „PEM electrolysis for production of hydrogen from renewable energy sources”. In: *Solar Energy* 78.5 (May 2005), pp. 661–669. ISSN: 0038092X. DOI: [10.1016/j.solener.2004.09.003](https://doi.org/10.1016/j.solener.2004.09.003).
- [60] Haluk Görgün. „Dynamic modelling of a proton exchange membrane (PEM) electrolyzer”. In: *International Journal of Hydrogen Energy* 31.1 (January 2006), pp. 29–38. ISSN: 03603199. DOI: [10.1016/j.ijhydene.2005.04.001](https://doi.org/10.1016/j.ijhydene.2005.04.001).

- [61] Vesa Ruuskanen et al. „PEM water electrolyzer model for a power-hardware-in-loop simulator”. In: *International Journal of Hydrogen Energy* 42.16 (April 2017), pp. 10775–10784. ISSN: 03603199. DOI: [10.1016/j.ijhydene.2017.03.046](https://doi.org/10.1016/j.ijhydene.2017.03.046).
- [62] François Parache et al. „Impact of Power Converter Current Ripple on the Degradation of PEM Electrolyzer Performances”. In: *Membranes* 12.2 (February 2022). ISSN: 20770375. DOI: [10.3390/membranes12020109](https://doi.org/10.3390/membranes12020109).
- [63] Vesa Ruuskanen et al. „Power quality estimation of water electrolyzers based on current and voltage measurements”. In: *Journal of Power Sources* 450 (February 2020). ISSN: 03787753. DOI: [10.1016/j.jpowsour.2019.227603](https://doi.org/10.1016/j.jpowsour.2019.227603).
- [64] Henning P.C. Buitendach et al. „Effect of a ripple current on the efficiency of a PEM electrolyser”. In: *Results in Engineering* 10 (June 2021). ISSN: 25901230. DOI: [10.1016/j.rineng.2021.100216](https://doi.org/10.1016/j.rineng.2021.100216).
- [65] Francisco Da Costa Lopes and Edson H. Watanabe. „Experimental and theoretical development of a PEM electrolyzer model applied to energy storage systems”. In: *2009 Brazilian Power Electronics Conference, COBEP2009*. IEEE Computer Society, 2009, pp. 775–782. ISBN: 9781424433704. DOI: [10.1109/COBEP.2009.5347619](https://doi.org/10.1109/COBEP.2009.5347619).
- [66] Yuedong Zhan et al. „Comprehensive influences measurement and analysis of power converter low frequency current ripple on PEM fuel cell”. In: *International Journal of Hydrogen Energy* 44.59 (November 2019), pp. 31352–31359. ISSN: 03603199. DOI: [10.1016/j.ijhydene.2019.09.231](https://doi.org/10.1016/j.ijhydene.2019.09.231).
- [67] Bouchra Wahdame et al. „Impact of power converter current ripple on the durability of a fuel cell stack”. In: *IEEE International Symposium on Industrial Electronics*. 2008, pp. 1495–1500. ISBN: 1424416655. DOI: [10.1109/ISIE.2008.4677206](https://doi.org/10.1109/ISIE.2008.4677206).
- [68] Brinda A. Thomas, Inês L. Azevedo, and Granger Morgan. „Edison Revisited: Should we use DC circuits for lighting in commercial buildings?” In: *Energy Policy* 45 (June 2012), pp. 399–411. ISSN: 03014215. DOI: [10.1016/j.enpol.2012.02.048](https://doi.org/10.1016/j.enpol.2012.02.048).
- [69] Vagelis Vossos, Karina Garbesi, and Hongxia Shen. „Energy savings from direct-DC in U.S. residential buildings”. In: *Energy and Buildings* 68.PARTA (2014), pp. 223–231. ISSN: 03787788. DOI: [10.1016/j.enbuild.2013.09.009](https://doi.org/10.1016/j.enbuild.2013.09.009).
- [70] Brock Glasgo, Inês Lima Azevedo, and Chris Hendrickson. „How much electricity can we save by using direct current circuits in homes? Understanding the potential for electricity savings and assessing feasibility of a transition towards DC powered buildings”. In: *Applied Energy* 180 (October 2016), pp. 66–75. ISSN: 03062619. DOI: [10.1016/j.apenergy.2016.07.036](https://doi.org/10.1016/j.apenergy.2016.07.036).
- [71] Bernd Wunder et al. „Energy efficient DC-grids for commercial buildings”. In: *INTELEC, International Telecommunications Energy Conference (Proceedings)*. Vol. 2014-January. January. Institute of Electrical and Electronics Engineers Inc., 2014. ISBN: 9781479931057. DOI: [10.1109/intlec.2014.6972215](https://doi.org/10.1109/intlec.2014.6972215).

- [72] U. Boeke and M. Wendt. „DC power grids for buildings”. In: *2015 IEEE 1st International Conference on Direct Current Microgrids, ICDCM 2015*. Institute of Electrical and Electronics Engineers Inc., July 2015, pp. 210–214. ISBN: 9781479998791. DOI: [10.1109/ICDCM.2015.7152040](https://doi.org/10.1109/ICDCM.2015.7152040).
- [73] Daniel Fregosi et al. „A comparative study of DC and AC microgrids in commercial buildings across different climates and operating profiles”. In: *2015 IEEE 1st International Conference on Direct Current Microgrids, ICDCM 2015*. Institute of Electrical and Electronics Engineers Inc., July 2015, pp. 159–164. ISBN: 9781479998791. DOI: [10.1109/ICDCM.2015.7152031](https://doi.org/10.1109/ICDCM.2015.7152031).
- [74] Masatoshi Noritake et al. „Demonstrative research on DC microgrids for office buildings”. In: *INTELEC, International Telecommunications Energy Conference (Proceedings)*. Vol. 2014-January. January. Institute of Electrical and Electronics Engineers Inc., 2014. ISBN: 9781479931057. DOI: [10.1109/intlec.2014.6972180](https://doi.org/10.1109/intlec.2014.6972180).
- [75] Vagelis Vossos et al. „Techno-economic analysis of DC power distribution in commercial buildings”. In: *Applied Energy* 230 (November 2018), pp. 663–678. ISSN: 03062619. DOI: [10.1016/j.apenergy.2018.08.069](https://doi.org/10.1016/j.apenergy.2018.08.069).
- [76] Daniel L. Gerber, Richard Liou, and Richard Brown. „Energy-saving opportunities of direct-DC loads in buildings”. In: *Applied Energy* 248 (August 2019), pp. 274–287. ISSN: 03062619. DOI: [10.1016/j.apenergy.2019.04.089](https://doi.org/10.1016/j.apenergy.2019.04.089).
- [77] Darian Andreas Schaab et al. „Simulative Analysis of a Flexible, Robust and Sustainable Energy Supply through Industrial Smart-DC-Grid with Distributed Grid Management”. In: *Procedia CIRP*. Vol. 69. Elsevier B.V., 2018, pp. 366–370. DOI: [10.1016/j.procir.2017.11.037](https://doi.org/10.1016/j.procir.2017.11.037).
- [78] Timm Kuhlmann, Isabella Bianchini, and Alexander Sauer. „Resource and energy efficiency assessment of an industrial DC smart grid”. In: *Procedia CIRP*. Vol. 90. Elsevier B.V., 2020, pp. 672–676. DOI: [10.1016/j.procir.2020.01.074](https://doi.org/10.1016/j.procir.2020.01.074).
- [79] Kris Baert. *EnergyVille Bipolar low-voltage DC lab. Flexible DC lab Test facility for the new low-voltage DC technology for building-level nanogrids and district-level microgrids*. https://www.energyville.be/sites/energyville/files/downloads/2020/dc_labnewstyleweb.pdf.
- [80] Qianqian Jiao, Rasoul Hosseini, and Robert M. Cuzner. „A comparison between silicon carbide based current source rectifier and voltage source rectifier for applications in community DC microgrid”. In: *2016 IEEE International Conference on Renewable Energy Research and Applications, ICRERA 2016*. Institute of Electrical and Electronics Engineers Inc., March 2017, pp. 544–549. ISBN: 9781509033881. DOI: [10.1109/ICRERA.2016.7884394](https://doi.org/10.1109/ICRERA.2016.7884394).
- [81] Stafan Pfenninger and Iain Staffell. *Renewables.ninja*. April 2020. URL: www.renewables.ninja (visited on 05/05/2022).

- [82] Iain Staffell and Stefan Pfenninger. „Using bias-corrected reanalysis to simulate current and future wind power output”. In: *Energy* 114 (November 2016), pp. 1224–1239. ISSN: 03605442. DOI: [10.1016/j.energy.2016.08.068](https://doi.org/10.1016/j.energy.2016.08.068).
- [83] Stefan Pfenninger and Iain Staffell. „Long-term patterns of European PV output using 30 years of validated hourly reanalysis and satellite data”. In: *Energy* 114 (November 2016), pp. 1251–1265. ISSN: 03605442. DOI: [10.1016/j.energy.2016.08.060](https://doi.org/10.1016/j.energy.2016.08.060).
- [84] Ned Mohan, Tore M. Underland, and William P. Robbins. *Power Electronics: Applications and Design*. 3rd ed. Danvers, MA: Wiley, 2003.
- [85] Kuei Hsiang Chao and Chun Hao Huang. „Bidirectional DC-DC soft-switching converter for stand-alone photovoltaic power generation systems”. In: *IET Power Electronics* 7.6 (2014), pp. 1557–1565. ISSN: 17554543. DOI: [10.1049/iet-pel.2013.0335](https://doi.org/10.1049/iet-pel.2013.0335).
- [86] Abdelfatah Kolli et al. *A review on DC/DC converter architectures for power fuel cell applications*. August 2015. DOI: [10.1016/j.enconman.2015.07.060](https://doi.org/10.1016/j.enconman.2015.07.060).
- [87] Martijn Deckers and Johan Driesen. *An Investigation on the Impact of the Driver to the Performance of GaN Components*. Leuven, BE.
- [88] Damien Guilbert, Stefania Maria Collura, and Angel Scipioni. *DC/DC converter topologies for electrolyzers: State-of-the-art and remaining key issues*. 2017. DOI: [10.1016/j.ijhydene.2017.07.174](https://doi.org/10.1016/j.ijhydene.2017.07.174).
- [89] Mohammad Kabalo et al. „State-of-the-art of DC-DC converters for fuel cell vehicles”. In: *2010 IEEE Vehicle Power and Propulsion Conference, VPPC 2010*. 2010. ISBN: 9781424482191. DOI: [10.1109/VPPC.2010.5729051](https://doi.org/10.1109/VPPC.2010.5729051).
- [90] Sakda Somkun, Chatchai Sirisamphanwong, and Sukruedee Sukchai. „A DSP-based interleaved boost DC-DC converter for fuel cell applications”. In: *International Journal of Hydrogen Energy* 40.19 (May 2015), pp. 6391–6404. ISSN: 03603199. DOI: [10.1016/j.ijhydene.2015.03.069](https://doi.org/10.1016/j.ijhydene.2015.03.069).
- [91] Damien Guilbert et al. „Fuel cell systems reliability and availability enhancement by developing a fast and efficient power switch open-circuit fault detection algorithm in interleaved DC/DC boost converter topologies”. In: *International Journal of Hydrogen Energy* 41.34 (September 2016), pp. 15505–15517. ISSN: 03603199. DOI: [10.1016/j.ijhydene.2016.01.169](https://doi.org/10.1016/j.ijhydene.2016.01.169).
- [92] Boris Axelrod, Yefim Berkovich, and Adrian Ioinovici. „Switched-capacitor/switched-inductor structures for getting transformerless hybrid DC-DC PWM converters”. In: *IEEE Transactions on Circuits and Systems I: Regular Papers* 55.2 (2008), pp. 687–696. ISSN: 10577122. DOI: [10.1109/TCSI.2008.916403](https://doi.org/10.1109/TCSI.2008.916403).
- [93] Il Oun Lee, Shin Young Cho, and Gun Woo Moon. „Interleaved buck converter having low switching losses and improved step-down conversion ratio”. In: *IEEE Transactions on Power Electronics* 27.8 (2012), pp. 3664–3675. ISSN: 08858993. DOI: [10.1109/TPEL.2012.2185515](https://doi.org/10.1109/TPEL.2012.2185515).

- [94] Wilmar Martinez et al. „A novel high step-down interleaved converter with coupled inductor”. In: *INTELEC, International Telecommunications Energy Conference (Proceedings)*. Vol. 2016-September. Institute of Electrical and Electronics Engineers Inc., September 2016. ISBN: 9781479965823. DOI: [10.1109/INTLEC.2015.7572421](https://doi.org/10.1109/INTLEC.2015.7572421).
- [95] Mriganka Biswas, Somanath Majhi, and Harshal Nemade. „Two-phase high efficiency interleaved buck converter with improved step-down conversion ratio and low voltage stress”. In: *IET Power Electronics* 12.15 (December 2019), pp. 3942–3952. ISSN: 17554543. DOI: [10.1049/iet-pel.2019.0547](https://doi.org/10.1049/iet-pel.2019.0547).
- [96] Menaouar Berrehil El Kattel et al. „Four-phase interleaved DC–DC step-down converter using coupled inductor for high power application”. In: *International Journal of Circuit Theory and Applications* 48.10 (October 2020), pp. 1696–1723. ISSN: 1097007X. DOI: [10.1002/cta.2843](https://doi.org/10.1002/cta.2843).
- [97] Andrei Blinov and Anna Andrijanovits. „New DC/DC Converter for Electrolyser Interfacing with Stand-Alone Renewable Energy System”. In: *Electrical, Control and Communication Engineering* 1.1 (February 2013), pp. 24–29. ISSN: 2255-9140. DOI: [10.2478/v10314-012-0004-1](https://doi.org/10.2478/v10314-012-0004-1).
- [98] P. Chandrasekhar and S. Rama Reddy. „Performance of soft-switched DC-DC resonant converter for Electrolyzer”. In: *Proceedings - ISRCS 2011: 4th International Symposium on Resilient Control Systems*. 2011, pp. 95–100. ISBN: 9781424492930. DOI: [10.1109/ISRCS.2011.6016096](https://doi.org/10.1109/ISRCS.2011.6016096).
- [99] Riccardo Pittini, Zhe Zhang, and Michael A.E. Andersen. „Isolated full bridge boost DC-DC converter designed for bidirectional operation of fuel cells/electrolyzer cells in grid-tie applications”. In: *2013 15th European Conference on Power Electronics and Applications, EPE 2013*. 2013. ISBN: 9781479901166. DOI: [10.1109/EPE.2013.6634433](https://doi.org/10.1109/EPE.2013.6634433).
- [100] Dharmraj V. Ghodke, Kishore Chatterjee, and B. G. Fernandes. „Three-phase three level, soft switched, phase shifted PWM DC-DC converter for high power applications”. In: *IEEE Transactions on Power Electronics* 23.3 (May 2008), pp. 1214–1227. ISSN: 08858993. DOI: [10.1109/TPEL.2008.920881](https://doi.org/10.1109/TPEL.2008.920881).
- [101] Damien Guilbert and Gianpaolo Vitale. „Dynamic emulation of a PEM electrolyzer by time constant based exponential model”. In: *Energies* 12.4 (February 2019). ISSN: 19961073. DOI: [10.3390/en12040750](https://doi.org/10.3390/en12040750).
- [102] Ángel Hernández-Gómez et al. „Development of an adaptive static-dynamic electrical model based on input electrical energy for PEM water electrolysis”. In: *International Journal of Hydrogen Energy* 45.38 (July 2020), pp. 18817–18830. ISSN: 03603199. DOI: [10.1016/j.ijhydene.2020.04.182](https://doi.org/10.1016/j.ijhydene.2020.04.182).
- [103] F. Marangio, M. Santarelli, and M. Calì. „Theoretical model and experimental analysis of a high pressure PEM water electrolyser for hydrogen production”. In: *International Journal of Hydrogen Energy* 34.3 (February 2009), pp. 1143–1158. ISSN: 03603199. DOI: [10.1016/j.ijhydene.2008.11.083](https://doi.org/10.1016/j.ijhydene.2008.11.083).

- [104] A. Awasthi, Keith Scott, and S. Basu. „Dynamic modeling and simulation of a proton exchange membrane electrolyzer for hydrogen production”. In: *International Journal of Hydrogen Energy* 36.22 (November 2011), pp. 14779–14786. ISSN: 03603199. DOI: [10.1016/j.ijhydene.2011.03.045](https://doi.org/10.1016/j.ijhydene.2011.03.045).
- [105] Vincenzo Liso et al. „Modelling and experimental analysis of a polymer electrolyte membrane water electrolysis cell at different operating temperatures”. In: *Energies* 11.12 (December 2018). ISSN: 19961073. DOI: [10.3390/en11123273](https://doi.org/10.3390/en11123273).
- [106] Raúl Sarrias-Mena et al. „Electrolyzer models for hydrogen production from wind energy systems”. In: *International Journal of Hydrogen Energy* 40.7 (February 2015), pp. 2927–2938. ISSN: 03603199. DOI: [10.1016/j.ijhydene.2014.12.125](https://doi.org/10.1016/j.ijhydene.2014.12.125).
- [107] Manuel Espinosa-López et al. „Modelling and experimental validation of a 46 kW PEM high pressure water electrolyzer”. In: *Renewable Energy* 119 (April 2018), pp. 160–173. ISSN: 18790682. DOI: [10.1016/j.renene.2017.11.081](https://doi.org/10.1016/j.renene.2017.11.081).
- [108] M. G. Santarelli, M. F. Torchio, and P. Cochis. „Parameters estimation of a PEM fuel cell polarization curve and analysis of their behavior with temperature”. In: *Journal of Power Sources* 159.2 (September 2006), pp. 824–835. ISSN: 03787753. DOI: [10.1016/j.jpowsour.2005.11.099](https://doi.org/10.1016/j.jpowsour.2005.11.099).
- [109] C. Y. Biaku et al. „A semiempirical study of the temperature dependence of the anode charge transfer coefficient of a 6 kW PEM electrolyzer”. In: *International Journal of Hydrogen Energy* 33.16 (August 2008), pp. 4247–4254. ISSN: 03603199. DOI: [10.1016/j.ijhydene.2008.06.006](https://doi.org/10.1016/j.ijhydene.2008.06.006).
- [110] Chen Gong et al. „Fick’s Law Assisted Propagation for Semisupervised Learning”. In: *IEEE Transactions on Neural Networks and Learning Systems* 26.9 (September 2015), pp. 2148–2162. ISSN: 21622388. DOI: [10.1109/TNNLS.2014.2376963](https://doi.org/10.1109/TNNLS.2014.2376963).
- [111] Faruk Civan. „CHAPTER 3 - PETROGRAPHICAL CHARACTERISTICS OF PETROLEUM-BEARING FORMATIONS”. In: *Reservoir Formation Damage (Second Edition)*. Ed. by Faruk Civan. Second Edition. Burlington: Gulf Professional Publishing, 2007, pp. 78–100. ISBN: 978-0-7506-7738-7. DOI: <https://doi.org/10.1016/B978-075067738-7/50004-X>. URL: <https://www.sciencedirect.com/science/article/pii/B978075067738750004X>.
- [112] Adam Z. Weber et al. „A Critical Review of Modeling Transport Phenomena in Polymer-Electrolyte Fuel Cells”. In: *Journal of The Electrochemical Society* 161.12 (2014), F1254–F1299. ISSN: 0013-4651. DOI: [10.1149/2.0751412jes](https://doi.org/10.1149/2.0751412jes).
- [113] Meng Ni, Michael K.H. Leung, and Dennis Y.C. Leung. „An electrochemical model of a solid oxide steam electrolyzer for hydrogen production”. In: *Chemical Engineering and Technology* 29.5 (May 2006), pp. 636–642. ISSN: 09307516. DOI: [10.1002/ceat.200500378](https://doi.org/10.1002/ceat.200500378).

- [114] Huayang Zhu and Robert J. Kee. „A general mathematical model for analyzing the performance of fuel-cell membrane-electrode assemblies”. In: *Journal of Power Sources* 117.1-2 (May 2003), pp. 61–74. ISSN: 03787753. DOI: [10.1016/S0378-7753\(03\)00358-6](https://doi.org/10.1016/S0378-7753(03)00358-6).
- [115] Adam Z. Weber and John Newman. „Transport in Polymer-Electrolyte Membranes”. In: *Journal of The Electrochemical Society* 150.7 (2003), A1008. ISSN: 00134651. DOI: [10.1149/1.1580822](https://doi.org/10.1149/1.1580822).
- [116] Burin Yodwong et al. „Proton exchange membrane electrolyzer emulator for power electronics testing applications”. In: *Processes* 9.3 (March 2021). ISSN: 22279717. DOI: [10.3390/pr9030498](https://doi.org/10.3390/pr9030498).
- [117] *Maxeon 3 400W Residential Solar Panel*. SPR-MAX3-400. Sunpower Maxeon. 2019. URL: <https://cdn-happerp.com/scripts/ajaxFileDisplay.php?file=data/files/articles/2414/documents/sunpower-maxeon-3-400w-nl.pdf&ajaxSubdomain=gd-energy> (visited on 06/08/2022).
- [118] Quinten Brosens, Ronald Leyman, and Merijn Van Deyck. „PV Battery System Design”. unpublished. May 2021.
- [119] Yuki Tsuno, Yoshihiro Hishikawa, and Kosuke Kurokawa. „Translation equations for temperature and irradiance of the I-V curves of various PV cells and modules”. In: *Conference Record of the 2006 IEEE 4th World Conference on Photovoltaic Energy Conversion, WCPEC-4*. Vol. 2. IEEE Computer Society, 2006, pp. 2246–2249. ISBN: 1424400163. DOI: [10.1109/WCPEC.2006.279619](https://doi.org/10.1109/WCPEC.2006.279619).
- [120] Farnell. *Farnell België - Distributeur elektronische componenten*. 2022. URL: <https://be.farnell.com> (visited on 04/20/2022).
- [121] Farnell. *Farnell UK - Electronic Components Distributor*. 2022. URL: <https://uk.farnell.com> (visited on 04/18/2022).
- [122] Giovanni Franceschini et al. „3boost: A high-power three-phase step-up full-bridge converter for automotive applications”. In: *IEEE Transactions on Industrial Electronics* 55.1 (January 2008), pp. 173–183. ISSN: 02780046. DOI: [10.1109/TIE.2007.905930](https://doi.org/10.1109/TIE.2007.905930).
- [123] Ling Gu, Ke Jin, and Chang Liu. „Current-tripler-rectifier pulse width modulation ZVS three-phase full-bridge DC/DC converter with Y- Δ connected transformer”. In: *IET Power Electronics* 8.7 (July 2015), pp. 1111–1118. ISSN: 17554543. DOI: [10.1049/iet-pel.2014.0415](https://doi.org/10.1049/iet-pel.2014.0415).
- [124] *High Current Inductor High Frequency 200 uH, 600 Amps*. HCS-201M-600A. Coil Winding Specialist Inc. 2022. URL: <https://www.coilws.com/images/HCS-201M-600A%5C%20REV.D.pdf> (visited on 05/25/2022).
- [125] *Semitrans 3. Fast IGBT4 Modules*. SKM400GM12T4. Semikron. 2013. URL: <https://www.farnell.com/datasheets/2085432.pdf> (visited on 05/25/2022).
- [126] *Fast Recovery Epitaxial Diode (FRED)*. DSEI120-12A. IXYS. 2012. URL: <https://www.farnell.com/datasheets/1678168.pdf> (visited on 05/25/2022).

- [127] J. A. Oliver et al. „Passive component analysis in interleaved buck converters”. In: *Conference Proceedings - IEEE Applied Power Electronics Conference and Exposition - APEC*. Vol. 1. 2004, pp. 623–628. DOI: [10.1109/apec.2004.1295871](https://doi.org/10.1109/apec.2004.1295871).
- [128] *KEMET Part Number: C44PLGR6500RBSK*. C44PLGR6500RASK. KEMET. 2022. URL: <https://api.kemet.com/component-edge/download/specsheet/C44PLGR6500RBSK.pdf> (visited on 05/29/2022).
- [129] Coil Winding Specialist. *Very High Current Power*. May 2022. URL: https://www.coilws.com/index.php?main_page=index&cPath=208_212_366 (visited on 05/26/2022).
- [130] *High Current Through-Hole Inductor, High Temperature*. IHXL-1500VZ-5A. Vishay. 2020. URL: <https://www.farnell.com/datasheets/3180558.pdf> (visited on 05/26/2022).
- [131] *1200V XPT Gen X4 IGBT. Ultra Low-Vsat PT IGBT for up to 5kHz switching*. IXYS. 2020. URL: <https://www.farnell.com/datasheets/3093869.pdf> (visited on 05/27/2022).
- [132] *IGBT - Ultra Field Stop*. FGH40T120SQDNL4. ON Semiconductor. March 2018. URL: <https://www.farnell.com/datasheets/2619971.pdf> (visited on 05/17/2022).
- [133] Drisya K Sasi and A. S Haryhar. „A transformer-less high efficiency interleaved buck converter with improved step-down conversion ratio and a pre-charging setup through snubber circuit”. eng. In: *2017 IEEE International Conference on Signal Processing, Informatics, Communication and Energy Systems (SPICES)*. IEEE, 2017, pp. 1–6. ISBN: 1538638649.
- [134] Morteza Esteki et al. „Interleaved Buck Converter with Continuous Input Current, Extremely Low Output Current Ripple, Low Switching Losses, and Improved Step-Down Conversion Ratio”. In: *IEEE Transactions on Industrial Electronics* 62.8 (August 2015), pp. 4769–4776. ISSN: 02780046. DOI: [10.1109/TIE.2015.2397881](https://doi.org/10.1109/TIE.2015.2397881).
- [135] Wuhua Li et al. „High-step-up and high-efficiency fuel-cell power-generation system with active-clamp flyback-forward converter”. In: *IEEE Transactions on Industrial Electronics* 59.1 (January 2012), pp. 599–610. ISSN: 02780046. DOI: [10.1109/TIE.2011.2130499](https://doi.org/10.1109/TIE.2011.2130499).
- [136] River Tin Ho Li and Carl Ngai Man Ho. „An Active Snubber Cell for N-Phase Interleaved DC-DC Converters”. In: *IEEE Journal of Emerging and Selected Topics in Power Electronics* 4.2 (June 2016), pp. 344–351. ISSN: 21686785. DOI: [10.1109/JESTPE.2015.2449865](https://doi.org/10.1109/JESTPE.2015.2449865).
- [137] Svetozar S. Broussev and Nikolay T. Tchamov. „Two-phase self-assisted zero-voltage switching DC-DC converter”. In: *IEEE Transactions on Circuits and Systems II: Express Briefs* 60.3 (2013), pp. 157–161. ISSN: 15497747. DOI: [10.1109/TCSII.2013.2240875](https://doi.org/10.1109/TCSII.2013.2240875).

- [138] Ahwan Rahimi, Vida Ranjbarizad, and Ebrahim Babaei. „Interleaved Buck–Boost N-Phase High-Efficiency Converter with Soft Switching and Low Output Voltage Ripple”. In: *Arabian Journal for Science and Engineering* 46.10 (October 2021), pp. 9497–9513. ISSN: 21914281. DOI: [10.1007/s13369-021-05337-9](https://doi.org/10.1007/s13369-021-05337-9).

Appendix A

Electrolyzer Model Code

A.1 Anode Function

```
1 function [pO2,nO2,n_an_H2O,XO2] = Anode(I,A,NH20,Pan)
2 F = 96485.3329;
3 N_O2_gen = I/(4*F);
4 N_H2O_const = I/(2*F);
5 n_an_H2O = (NH20+N_H2O_const)/A;
6 nO2 = N_O2_gen/A;
7 XO2 = nO2/(nO2+n_an_H2O);
8 X_H2O = n_an_H2O/(nO2+n_an_H2O);
9 pO2 = XO2*Pan;
10 end
```

A.2 Cathode Function

```
1 function [pH2,nH2,n_cat_H2O,XH2] = Cathode(I,A,NH20,Pcat)
2 F = 96485.3329;
3 N_H2_gen = I/(2*F);
4 n_cat_H2O = NH20/A;
5 nH2 = N_H2_gen/A;
6 XH2 = nH2/(nH2+n_cat_H2O);
7 X_H2O = n_cat_H2O/(nH2+n_cat_H2O);
8 pH2 = XH2*Pcat;
9 end
```

A.3 Membrane Function

```

1  function [N_H2O,D_eff_an,D_eff_cat] = membrane(I,A,T,
      nH2O_an,nH2O_cat,Pan,Pcat)
2  k = 1.38064852*10^-23;
3  R = 8.3144598;
4  M_H2O = 18.01528;
5  M_O2 = 31.9988;
6  M_H2 = 2.01588;
7  F = 96485.3329;
8
9  r = 10^-6;
10 rho_H2O = 1000;
11 mu_H2O = 1.1;
12 d_mem = 0.000254;
13 d_el = 0.00008;
14 d_el_an = d_el;
15 d_el_cat = d_el;
16 Dw = 1.28*10^-10;
17 K_darcy = 1.58*10^-18;
18 nd = 7;
19
20 sig_O2 = 3.467*10^-10;
21 sig_H2 = 2.827*10^-10;
22 sig_H2O = 2.641*10^-10;
23
24 delta_p = Pcat-Pan;
25
26 e = 0.3;
27 ksi = 4;
28
29 sig_O2_H2O = (sig_H2O+sig_O2)/2;
30 sig_H2_H2O = (sig_H2O+sig_H2)/2;
31
32 e_O2= k*106.7;
33 e_H2 = k*59.7;
34 e_H2O = k*809.1;
35
36 e_O2_H2O = sqrt(e_O2*e_H2O);
37 e_H2_H2O = sqrt(e_H2*e_H2O);
38
39 t_O2_H2O = (k*T)/e_O2_H2O;
40 t_H2_H2O = (k*T)/e_H2_H2O;
41

```

```

42 tau = t_02_H20;
43 Omega_02_H20 = 1.06/tau^0.156 + 0.193/exp(0.476*tau) +
    1.036/exp(1.53*tau) + 1.765/(3.894*tau);
44
45 tau = t_H2_H20;
46 Omega_H2_H20 = 1.06/tau^0.156 + 0.193/exp(0.476*tau) +
    1.036/exp(1.53*tau) + 1.765/(3.894*tau);
47
48 D_02_H20 = 0.00133*sqrt(1/M_02 + 1/M_H20)*T^(3/2)/(Pan*
    sig_02_H20^2*Omega_02_H20);
49 D_H2_H20 = 0.00133*sqrt(1/M_H2 + 1/M_H20)*T^(3/2)/(Pcat*
    sig_H2_H20^2*Omega_H2_H20);
50
51 D_eff_H20 = 4/3*r*sqrt(8*R*T/(pi*M_H20));
52
53 D_eff_cat = 1/(e/ksi*(1/D_H2_H20+1/D_eff_H20));
54 D_eff_an = 1/(e/ksi*(1/D_02_H20+1/D_eff_H20));
55
56 C_an_H20_ch = rho_H20*T/M_H20;
57 C_cat_H20_ch = rho_H20*T/M_H20;
58
59 C_an_H20_mem = C_an_H20_ch - (d_el_an*nH20_an)/D_eff_an;
60 C_cat_H20_mem = C_cat_H20_ch+(d_el_cat*nH20_cat)/
    D_eff_cat;
61
62 N_H20_diff = A*Dw/d_mem * (C_cat_H20_mem-C_an_H20_mem);
63 N_H20_eod = nd*I/F;
64 N_H20_pe = K_darcy*A*rho_H20*delta_p/(d_mem*mu_H20*M_H20)
    ;
65
66 N_H20 = N_H20_diff + N_H20_eod+N_H20_pe;

```

A.4 Voltage Function

A.4.1 Open-circuit voltage

```

1 function V_oc = Voltage_oc(pH2,pO2,T)
2 R = 8.3144598;
3 F = 96485.3329;
4 E0 = 1.229-0.9*10^-3*(T-298);
5 V_oc = E0+R*T/(2*F)*log(pH2*sqrt(pO2));
6 end

```

A.4.2 Activation voltage

```

1 function V_act = Voltage_act(I,T,A)
2 i = I/A;
3 R = 8.3144598;
4 F = 96485.3329;
5 a_an = 0.8;
6 a_cat = 0.25;
7 i0_an = 10^-3;
8 i0_cat = 10^3;
9 V_act = R*T/(a_an*F)*asinh(i/(2*i0_an))+R*T/(a_cat*F)*
    asinh(i/(2*i0_cat));
10 end

```

A.4.3 Ohmic voltage

```

1 function [V_ohm,R_ohm,R_el,R_pl,R_mem,L] = Voltage_ohm(I,
    A,n_ch,T)
2 rho_el = 10.6*10^-8;
3 rho_an = 43.1*10^-8;
4 rho_cat = 16*10^-5;
5 eps = 0.3;
6 d_el = 0.00008;
7 d_mem = 0.000245;
8 hp = d_mem/2;
9 hc = d_mem/2;
10 lambda = 21;
11 [L,W,n_sp,w_ch,w_sp] = cell_dims(A,n_ch);
12
13 rho_eff = rho_el/(1-eps)^1.5;
14
15 R_el = rho_eff/(8*L)*((w_ch+w_sp)/(n_ch*d_el)+(w_ch+w_sp)
    /(n_ch*d_el));

```

```

16
17 R2_an = rho_an*hp/(W*L);
18 R2_cat = rho_cat*hp/(W*L);
19 Rs_cat = rho_cat*hc/(n_sp*w_sp*L);
20 Rs_an = rho_an*hc/(n_sp*w_sp*L);
21 R_pl = Rs_an + Rs_cat + R2_cat + R2_an;
22
23 sig_mem = 100*(0.005139*lambda - 0.00326)*exp
      (1268*(1/303-1/T));
24 R_mem = d_mem/(A*sig_mem);
25
26 R_ohm = R_el + R_pl + R_mem;
27 V_ohm = R_ohm*I;
28 end

```

A.4.4 Concentration voltage

```

1 function V_con= Voltage_con(Pan,Pcat,T,nO2,XO2,nH2,XH2,
      D_eff_an,D_eff_cat)
2 d_el = 0.00008;
3 R = 8.3144598;
4 F = 96485.3329;
5
6 C_O2_mem = Pan*XO2/(R*T)+d_el*nO2/D_eff_an;
7 C_H2_mem = Pcat*XH2/(R*T)+d_el*nH2/D_eff_cat;
8
9 CO_H2_mem = 67.1;
10 CO_O2_mem = 35.946;
11
12 V_con_an = R*T/(4*F)*log(C_O2_mem/CO_O2_mem);
13 V_con_cat = R*T/(4*F)*log(C_H2_mem/CO_H2_mem);
14 V_con = V_con_an + V_con_cat;
15 end

```


Appendix B

Component Datasheets

B.1 HCS-201M-600A

From [124]:

The information contained in this drawing is the sole property of Coil Winding Specialist, Inc. Any reproduction in part or whole without written permission of Coil Winding Specialist, Inc. is prohibited.

DIMENSIONAL TOLERANCES INCHES (MM)							
C	D	E	F	L	L1	W	H
0.24 (6.10)	6.50 (166.75)	1.50 (38.10)	0.50 (12.70)	18.00 (457.20)	14.00 (355.60)	4.50 (114.30)	4.00 (101.60)

REVISION HISTORY			
REV	ECN	DESCRIPTION	REV # DATE
C1		REVISED SPEED & DESCRIPTION	TH 06/21/21 A. 06/21/21
C2		REVISED FOM SPEC & DESCRIPTION	TH 06/23/21 A. 06/23/21
C3		REVISED FOM SPEC	TH 06/28/21 A. 06/28/21
D		UPDATED COPPER LEAD CONSTRUCTION	TH 02/10/22 A. 02/10/22

SCHEMATIC

SIDE VIEW
TOP VIEW
BACK VIEW

DC BIAS TABLE	
DC-BIAS	L
0A	200uH
25A	187uH
50A	175uH
75A	160uH
100A	167uH
125A	162uH
150A	157uH
175A	142uH
200A	129uH
225A	114uH
250A	101uH
275A	88uH
300A	79uH
325A	72uH
350A	67uH
375A	63uH
400A	60uH
425A	58uH
450A	57uH
475A	56uH
500A	55uH

8 APPLICATION: OUTPUT CHOKE, HIGH CURRENT INDUCTOR, INPUT FILTER
 7 BUILT TO RoHS COMPLIANCE
 6 LABEL PART NUMBER AND REVISION WHERE SHOWN
 VARNISH PART AND OVEN CURE
 5 APPLY SILICON AS REQUIRED
 WRAP TAPE AROUND CORES WITH CORES AND NOMEX
 PRE FORMED FLAT COPPER FOIL CONSTRUCTION:
 4 WEIGHT: 52 LBS TYPICAL
 RECOMMENDED OPERATING FREQUENCY: 60Hz TO 500kHz
 RECOMMENDED AMBIENT OPERATING TEMP: -40°C TO 105°C
 HI-POT TEST FROM WINDING TO CORE: 2500VDC @ 2mA, 1 MIN
 INTERWINDING CAPACITANCE = 198pF TYP @ SRF
 [Z] = 2.3 KILO-OHM TYP @ SRF
 SRF = 880 KHz TYPICAL
 RATED CURRENT: 600 AMPS, APPROPRIATE AIR FLOW NEEDED.
 DCR BETWEEN PINS 1 - 2: 2.7 MILLIOHMS MAX.
 INDUCTANCE @ DC BIAS: SEE TABLE ON THE RIGHT.
 INDUCTANCE BETWEEN PINS 1-2: 190uH ± 25% NOM., MEASURED AT 1 KHz, 0.25V, ZERO DC BIAS

3 SPECIFICATIONS:
 VARNISH AND BAKE
 SILICONE DOW CORNING OR EQUAL
 OUTER WRAP: 3M GLASS OR EQUAL
 2 CORE: COMPACTED POWDERED CORE
 1 MATERIAL: UL RECOGNIZED

ANY TOLERANCE. THIS DIM. CAN VARY A LITTLE FROM PART TO PART.
 TYP IN DIM. TOL. TABLE REFERS TO A NON-CRITICAL TYPICAL (AVERAGE) DIM. WITHOUT

NOTES: UNLESS OTHERWISE SPECIFIED READ, FROM BOTTOM UP.
 CAGE CODE: 5DME2

UNLESS OTHERWISE SPECIFIED		AUTOCAD		X	
DIMENSIONING AND TOLERANCES FOR ANSI Y14.5M	SYMBOL	SYMBOL	DATE	SYMBOL	DATE
ALL DIMENSIONS ARE IN INCHES AND DECIMALS THEREOF	DRWN	JL	07/14/17	SOLEWORKS	
TOLERANCE METRIC: .000+0.010 .000+0.020 <-40/30	ENGR	JLAU	07/14/17		
.000+0.025 .000+0.050 <-40/30	APPR	BO	07/14/17		
ANGLE PROJECTOR @ 45°					
DO NOT SCALE DRAWING					

PARTS LIST			
QTY	DESCRIPTION	REV	DATE
1	High Current Inductor High Frequency 200 uH, 600 Amps		
	HCS-201M-600A	REV D	


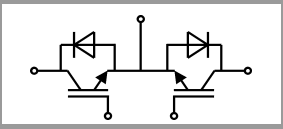
Coil Winding Specialist, Inc.
 333 W GROVE AVE
 ORANGE, CA 92665
 www.coilw.com
 coilw@coilw.com

SCALE: NOT_TO_SCALE SHEET 1 OF 1
 CAD-FILE:

EP FORM005 REV 3 10/01

B.2 Semitrans 3 IGBT

From [125]:

SKM400GM12T4						
						
SEMITRANS® 3						
Fast IGBT4 Modules						
SKM400GM12T4						
Features						
<ul style="list-style-type: none"> • IGBT4 = 4. generation fast trench IGBT (Infineon) • CAL4 = Soft switching 4. generation CAL-diode • Isolated copper baseplate using DBC technology (Direct Bonded Copper) • Increased power cycling capability • With integrated gate resistor • For higher switching frequencies up to 20kHz • UL recognized, file no. E63532 						
Typical Applications*						
<ul style="list-style-type: none"> • Matrix Inverter • Bidirectional switch 						
Remarks						
<ul style="list-style-type: none"> • Case temperature limited to $T_c = 125^\circ\text{C}$ max. • Recommended $T_{op} = -40 \dots +150^\circ\text{C}$ • Product reliability results valid for $T_j = 150^\circ\text{C}$ 						
						
GM						
Absolute Maximum Ratings						
Symbol	Conditions		Values	Unit		
IGBT						
V_{CES}	$T_j = 25^\circ\text{C}$		1200	V		
I_C	$T_j = 175^\circ\text{C}$	$T_c = 25^\circ\text{C}$	616	A		
		$T_c = 80^\circ\text{C}$	474	A		
I_{Cnom}			400	A		
I_{CRM}	$I_{CRM} = 3 \times I_{Cnom}$		1200	A		
V_{GES}			-20 ... 20	V		
t_{psc}	$V_{CC} = 800\text{ V}$ $V_{GE} \leq 15\text{ V}$ $V_{CES} \leq 1200\text{ V}$	$T_j = 150^\circ\text{C}$	10			μs
						-40 ... 175
T_j						
Inverse diode						
I_F	$T_j = 175^\circ\text{C}$	$T_c = 25^\circ\text{C}$	440		A	
		$T_c = 80^\circ\text{C}$	329		A	
I_{Fnom}			400		A	
I_{FRM}	$I_{FRM} = 3 \times I_{Fnom}$		1200		A	
I_{FSM}	$t_p = 10\text{ ms, sin } 180^\circ, T_j = 25^\circ\text{C}$		1980		A	
T_j			-40 ... 175 $^\circ\text{C}$			
Module						
$I_{j(RMS)}$	$T_{terminal} = 80^\circ\text{C}$		500		A	
T_{stg}			-40 ... 125		$^\circ\text{C}$	
V_{isol}	AC sinus 50 Hz, $t = 1\text{ min}$		4000		V	
Characteristics						
Symbol	Conditions		min.	typ.	max.	Unit
IGBT						
$V_{CE(sat)}$	$I_C = 400\text{ A}$ $V_{GE} = 15\text{ V}$ chiplevel	$T_j = 25^\circ\text{C}$	1.80	2.05	V	
		$T_j = 150^\circ\text{C}$	2.20	2.40	V	
V_{CE0}	chiplevel	$T_j = 25^\circ\text{C}$	0.8	0.9	V	
		$T_j = 150^\circ\text{C}$	0.7	0.8	V	
r_{CE}	$V_{GE} = 15\text{ V}$ chiplevel	$T_j = 25^\circ\text{C}$	2.50	2.88	$\text{m}\Omega$	
		$T_j = 150^\circ\text{C}$	3.75	4.00	$\text{m}\Omega$	
$V_{GE(th)}$	$V_{GE} = V_{CE}, I_C = 15.2\text{ mA}$		5	5.8	6.5	V
I_{CES}	$V_{GE} = 0\text{ V}$ $V_{CE} = 1200\text{ V}$	$T_j = 25^\circ\text{C}$	5		mA	
		$T_j = 150^\circ\text{C}$				
C_{ies}	$V_{CE} = 25\text{ V}$		24.6		nF	
C_{oes}	$V_{GE} = 0\text{ V}$		1.62		nF	
C_{res}			1.38		nF	
Q_G	$V_{GE} = -8\text{ V} \dots +15\text{ V}$		2260		nC	
R_{gint}	$T_j = 25^\circ\text{C}$		1.9		Ω	
$t_{d(on)}$	$V_{CC} = 600\text{ V}$ $I_C = 400\text{ A}$		220		ns	
t_r	$V_{GE} = \pm 15\text{ V}$	$T_j = 150^\circ\text{C}$	47		ns	
		$T_j = 150^\circ\text{C}$	33		mJ	
E_{on}	$R_{Gon} = 1\ \Omega$		505		ns	
$t_{d(off)}$	$R_{Goff} = 1\ \Omega$		78		ns	
t_f	$di/dt_{on} = 9700\text{ A}/\mu\text{s}$ $di/dt_{off} = 4300\text{ A}/\mu\text{s}$	$T_j = 150^\circ\text{C}$	42		mJ	
		$T_j = 150^\circ\text{C}$				
E_{off}			0.072		K/W	
$R_{th(j-c)}$	per IGBT					

SKM400GM12T4



SEMITRANS® 3

Fast IGBT4 Modules

SKM400GM12T4

Features

- IGBT4 = 4. generation fast trench IGBT (Infineon)
- CAL4 = Soft switching 4. generation CAL-diode
- Isolated copper baseplate using DBC technology (Direct Bonded Copper)
- Increased power cycling capability
- With integrated gate resistor
- For higher switching frequencies up to 20kHz
- UL recognized, file no. E63532

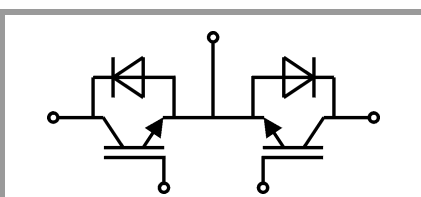
Typical Applications*

- Matrix Inverter
- Bidirectional switch

Remarks

- Case temperature limited to $T_c = 125^\circ\text{C}$ max.
- Recommended $T_{op} = -40 \dots +150^\circ\text{C}$
- Product reliability results valid for $T_j = 150^\circ\text{C}$

Characteristics						
Symbol	Conditions		min.	typ.	max.	Unit
Inverse diode						
$V_F = V_{EC}$	$I_F = 400\text{ A}$ $V_{GE} = 0\text{ V}$ chipelevel	$T_j = 25^\circ\text{C}$		2.20	2.52	V
		$T_j = 150^\circ\text{C}$		2.15	2.47	V
V_{F0}	chipelevel	$T_j = 25^\circ\text{C}$		1.3	1.5	V
		$T_j = 150^\circ\text{C}$		0.9	1.1	V
r_F	chipelevel	$T_j = 25^\circ\text{C}$		2.3	2.5	m Ω
		$T_j = 150^\circ\text{C}$		3.1	3.4	m Ω
I_{RRM}	$I_F = 400\text{ A}$	$T_j = 150^\circ\text{C}$		450		A
Q_{rr}	$di/dt_{off} = 8800\text{ A}/\mu\text{s}$	$T_j = 150^\circ\text{C}$		68		μC
E_{rr}	$V_{GE} = \pm 15\text{ V}$ $V_{CC} = 600\text{ V}$	$T_j = 150^\circ\text{C}$		30.5		mJ
$R_{th(j-c)}$	per diode				0.14	K/W
Module						
L_{CE}				15	20	nH
$R_{CC'+EE'}$	terminal-chip	$T_c = 25^\circ\text{C}$		0.25		m Ω
		$T_c = 125^\circ\text{C}$		0.5		m Ω
$R_{th(c-s)}$	per module			0.02	0.038	K/W
M_s	to heat sink M6			3	5	Nm
M_t		to terminals M6		2.5	5	Nm
						Nm
w					325	g



GM

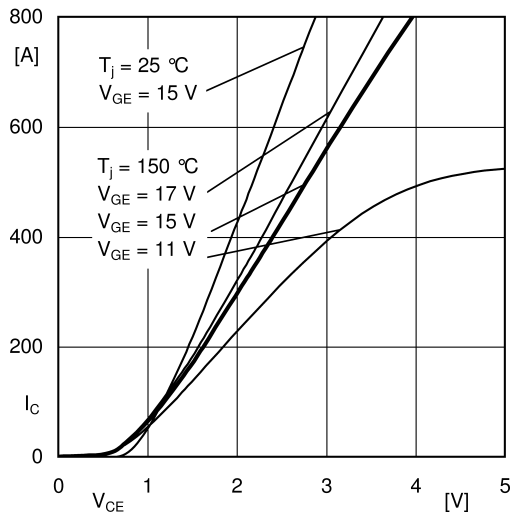


Fig. 1: Typ. output characteristic, inclusive R_{CC+EE}

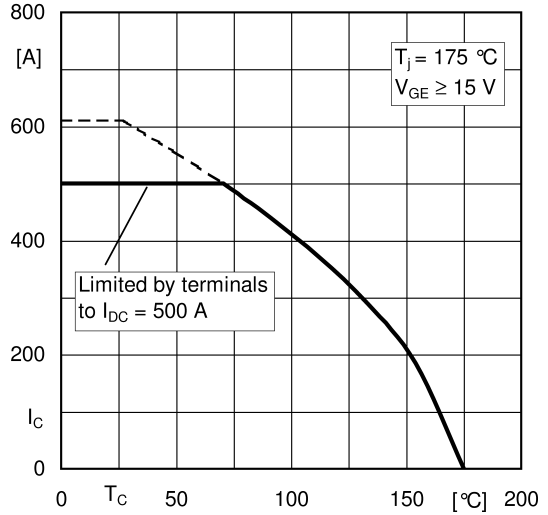


Fig. 2: Rated current vs. temperature $I_C = f(T_C)$

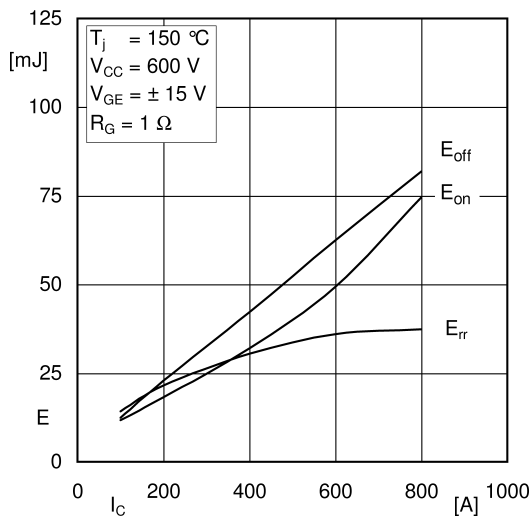


Fig. 3: Typ. turn-on /-off energy = $f(I_C)$

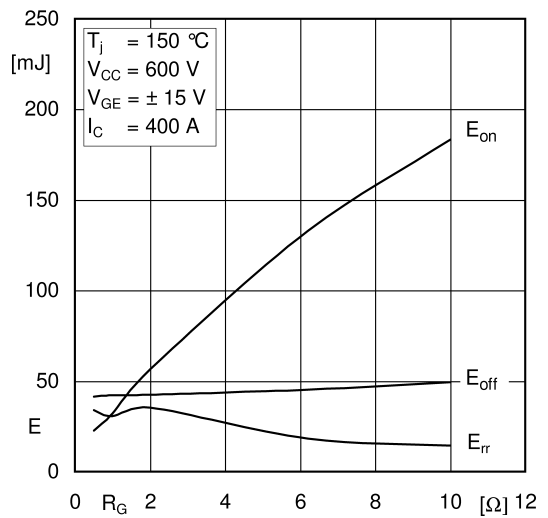


Fig. 4: Typ. turn-on /-off energy = $f(R_G)$

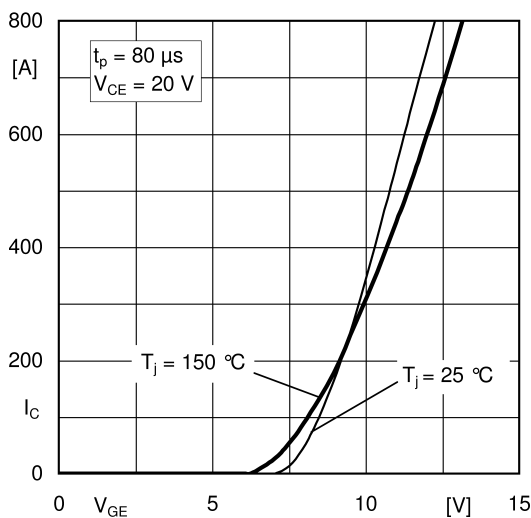


Fig. 5: Typ. transfer characteristic

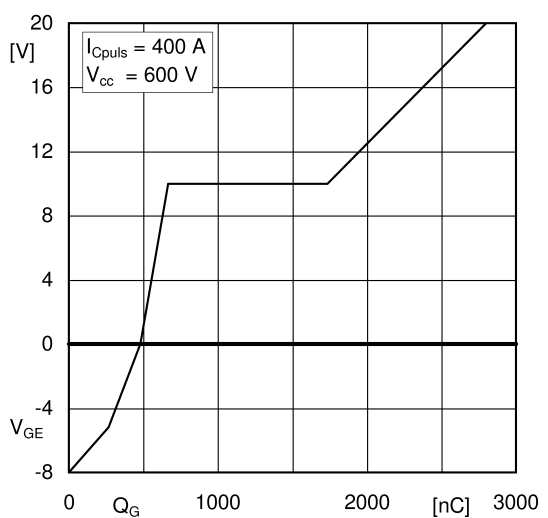


Fig. 6: Typ. gate charge characteristic

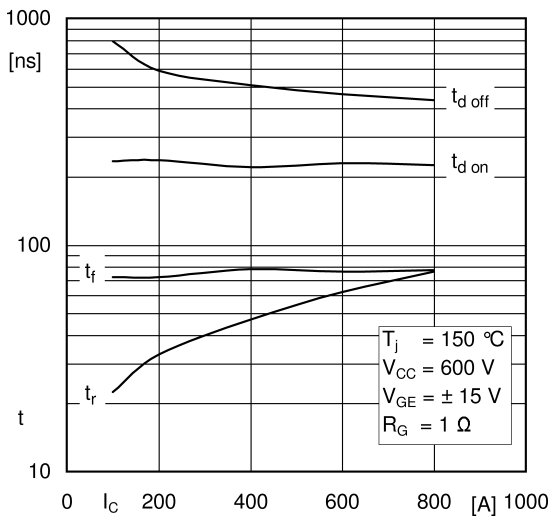


Fig. 7: Typ. switching times vs. I_C

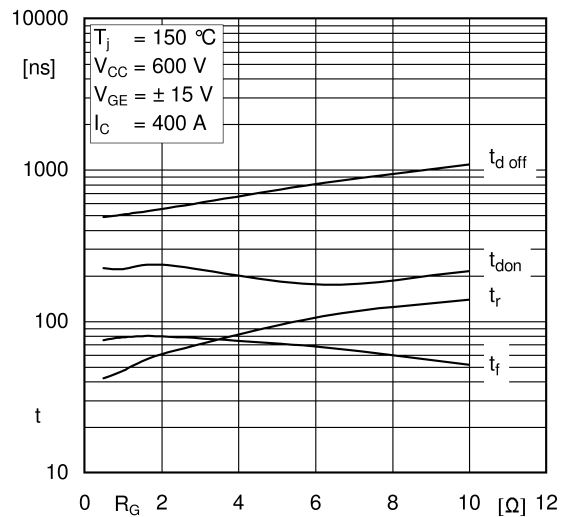


Fig. 8: Typ. switching times vs. gate resistor R_G

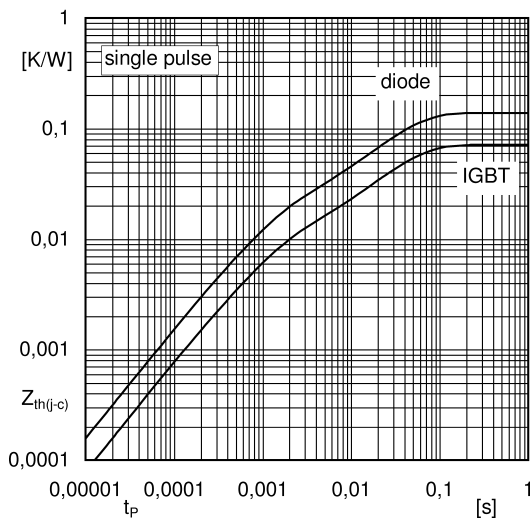


Fig. 9: Transient thermal impedance

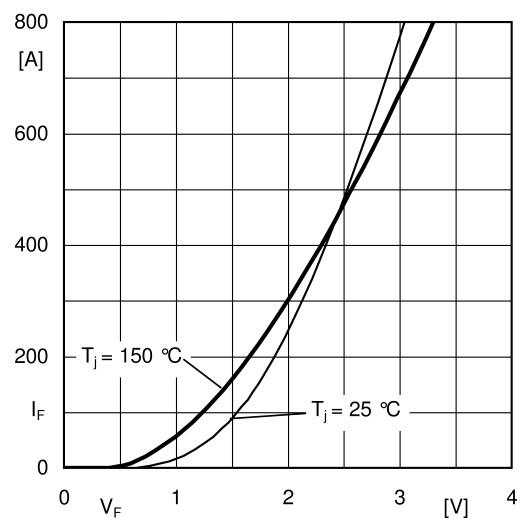


Fig. 10: Typ. CAL diode forward charact., incl. $R_{CC'+EE'}$

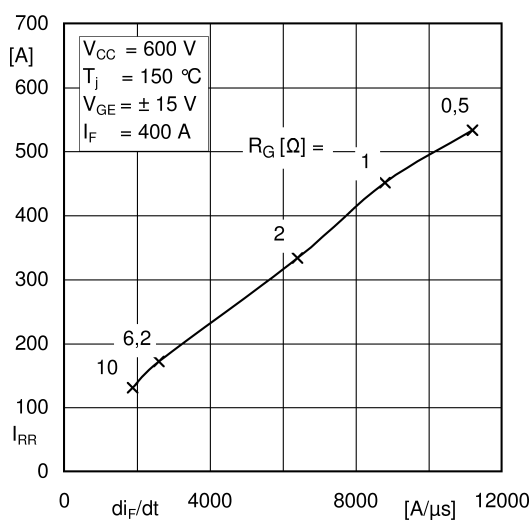


Fig. 11: CAL diode peak reverse recovery current

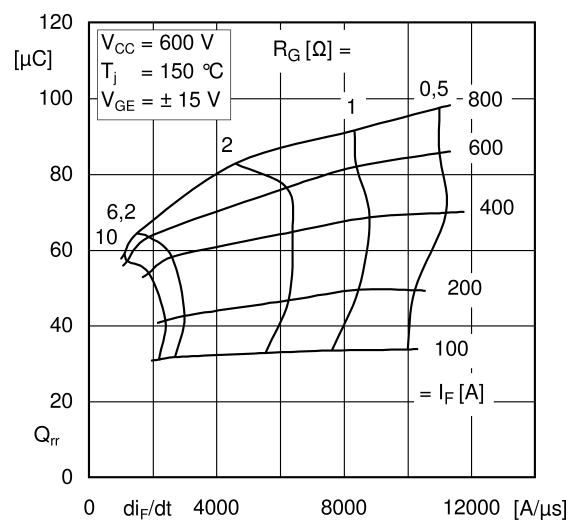
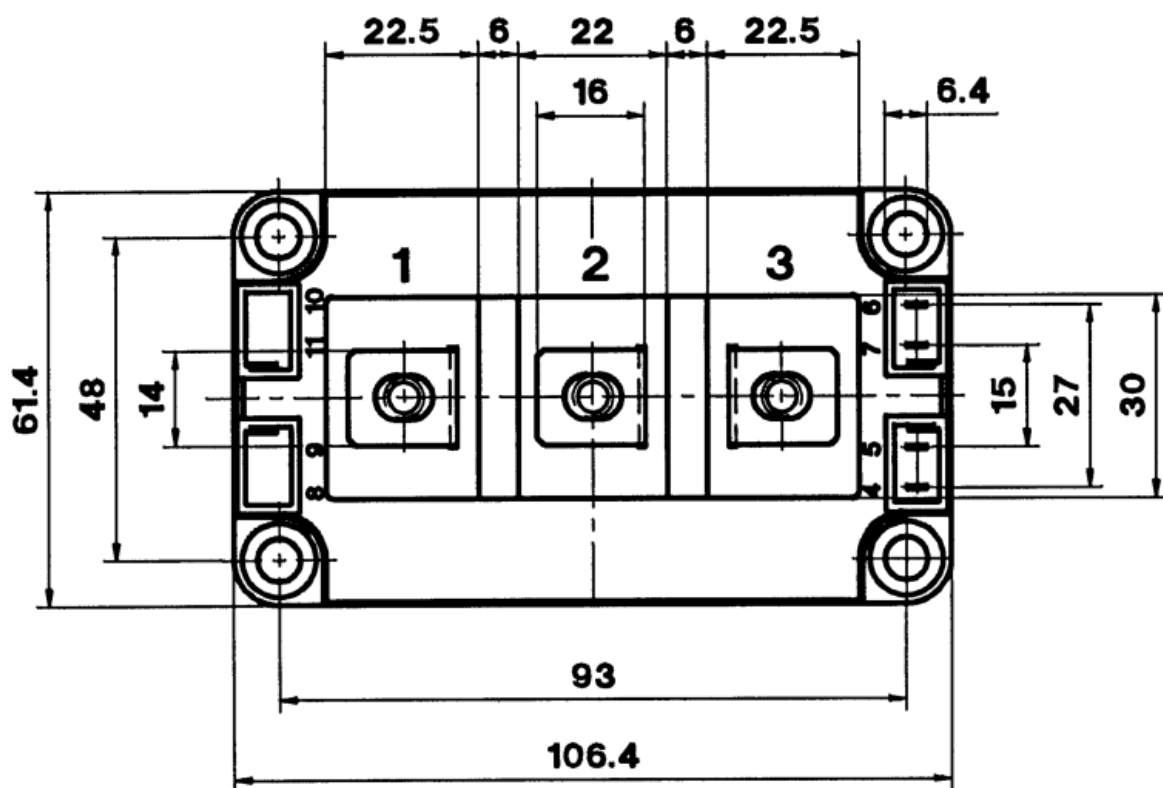
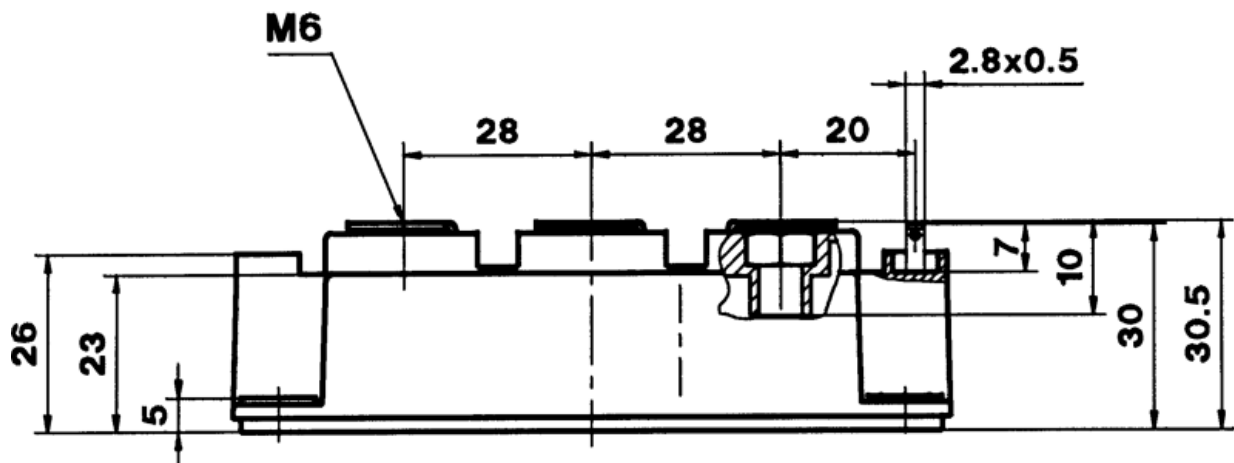
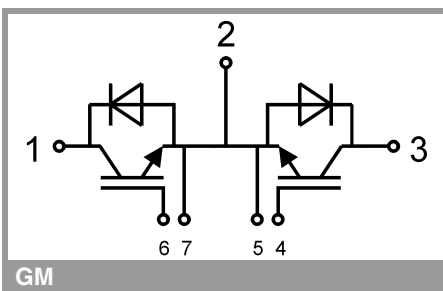


Fig. 12: Typ. CAL diode peak reverse recovery charge



SEMITRANS 3



This is an electrostatic discharge sensitive device (ESDS), international standard IEC 60747-1, Chapter IX

* The specifications of our components may not be considered as an assurance of component characteristics. Components have to be tested for the respective application. Adjustments may be necessary. The use of SEMIKRON products in life support appliances and systems is subject to prior specification and written approval by SEMIKRON. We therefore strongly recommend prior consultation of our staff.

B.3 DSEI-120-12A

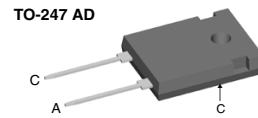
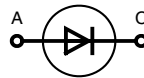
From [126]:



Fast Recovery Epitaxial Diode (FRED)

$I_{FAVM} = 109 \text{ A}$
 $V_{RRM} = 1200 \text{ V}$
 $t_{rr} = 40 \text{ ns}$

V_{RSM}	V_{RRM}	Type
V	V	
1200	1200	DSEI 120-12A



A = Anode, C = Cathode

Symbol	Conditions	Maximum Ratings	
I_{FRMS}	$T_{VJ} = T_{VJM}$	100	A
I_{FAVM} ①	$T_C = 60^\circ\text{C}$; rectangular, $d = 0.5$	109	A
I_{FAV} ②	$T_C = 95^\circ\text{C}$; rectangular, $d = 0.5$	75	A
I_{FRM}	$t_p < 10 \mu\text{s}$; rep. rating, pulse width limited by T_{VJM}	1200	A
I_{FSM}	$T_{VJ} = 45^\circ\text{C}$; $t = 10 \text{ ms}$ (50 Hz), sine	600	A
	$t = 8.3 \text{ ms}$ (60 Hz), sine	660	A
	$T_{VJ} = 150^\circ\text{C}$; $t = 10 \text{ ms}$ (50 Hz), sine	540	A
	$t = 8.3 \text{ ms}$ (60 Hz), sine	600	A
I^2t	$T_{VJ} = 45^\circ\text{C}$; $t = 10 \text{ ms}$ (50 Hz), sine	1800	A ² s
	$t = 8.3 \text{ ms}$ (60 Hz), sine	1800	A ² s
	$T_{VJ} = 150^\circ\text{C}$; $t = 10 \text{ ms}$ (50 Hz), sine	1450	A ² s
	$t = 8.3 \text{ ms}$ (60 Hz), sine	1500	A ² s
T_{VJ}		-40...+150	°C
T_{VJM}		150	°C
T_{sig}		-40...+150	°C
P_{tot}	$T_C = 25^\circ\text{C}$	357	W
M_d	mounting torque	0.8...1.2	Nm
Weight	typical	6	g

Features

- International standard package JEDEC TO-247 AD
- Planar passivated chips
- Very short recovery time
- Extremely low switching losses
- Low I_{FRM} -values
- Soft recovery behaviour
- Epoxy meets UL 94V-0

Applications

- Antiparallel diode for high frequency switching devices
- Anti saturation diode
- Snubber diode
- Free wheeling diode in converters and motor control circuits
- Rectifiers in switch mode power supplies (SMPS)
- Inductive heating and melting
- Uninterruptible power supplies (UPS)
- Ultrasonic cleaners and welders

Symbol	Conditions	Characteristic Values	
		typ.	max.
I_R	$V_R = V_{RRM}$ $T_{VJ} = 25^\circ\text{C}$		3 mA
	$V_R = 0.8 \cdot V_{RRM}$ $T_{VJ} = 25^\circ\text{C}$		1.5 mA
	$V_R = 0.8 \cdot V_{RRM}$ $T_{VJ} = 125^\circ\text{C}$		20 mA
V_F	$I_F = 70 \text{ A}$ $T_{VJ} = 150^\circ\text{C}$		1.55 V
	$T_{VJ} = 25^\circ\text{C}$		1.8 V
V_{T0}	for power-loss calculations only		1.2 V
r_T	$T_{VJ} = T_{VJM}$		4.6 mΩ
R_{thJC}	(version A)	0.25	0.35 K/W
R_{thCH}			K/W
R_{thJA}			35 K/W
t_{rr}	$I_F = 1 \text{ A}$; $-di/dt = 200 \text{ A}/\mu\text{s}$; $V_R = 30 \text{ V}$; $T_{VJ} = 25^\circ\text{C}$	40	60 ns
I_{RM}	$V_R = 350 \text{ V}$; $I_F = 75 \text{ A}$; $-di_F/dt = 200 \text{ A}/\mu\text{s}$	25	30 A
	$L \leq 0.05 \mu\text{H}$; $T_{VJ} = 100^\circ\text{C}$		

① Chip capability, ② limited to 70 A by leads Data according to IEC 60747

IXYS reserves the right to change limits, test conditions and dimensions.

20121114a

© 2012 IXYS All rights reserved

1 - 3

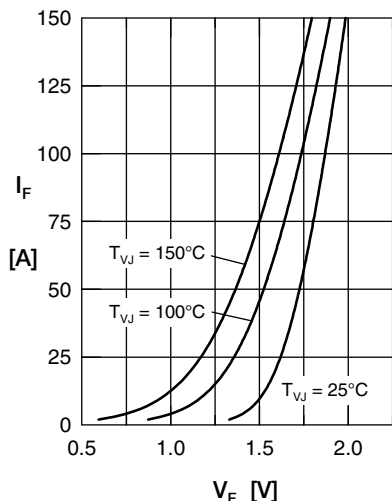


Fig. 1 Forward current I_F vs. V_F

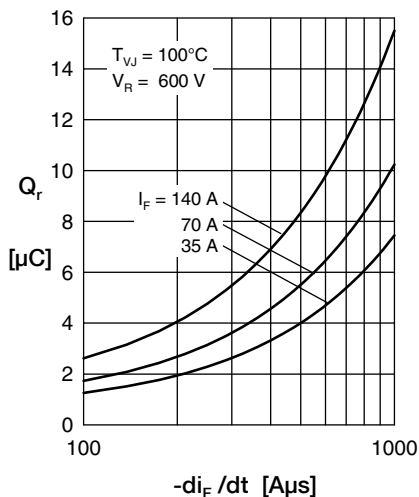


Fig. 2 Reverse recovery charge Q_r versus $-di_F/dt$

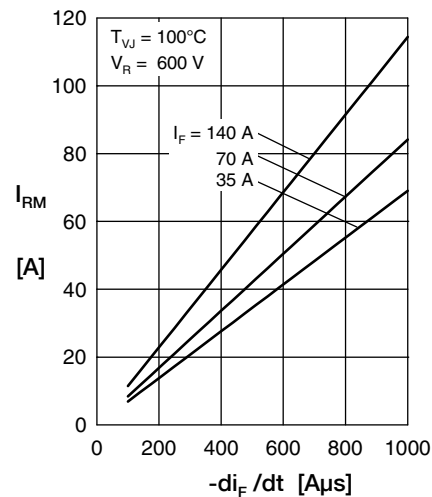


Fig. 3 Peak reverse current I_{RM} versus $-di_F/dt$

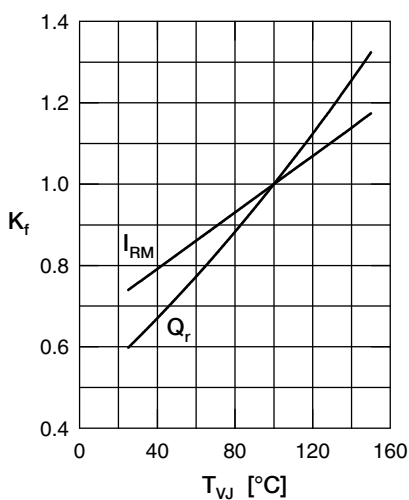


Fig. 4 Dynamic parameters Q_r, I_{RM} versus T_{VJ}

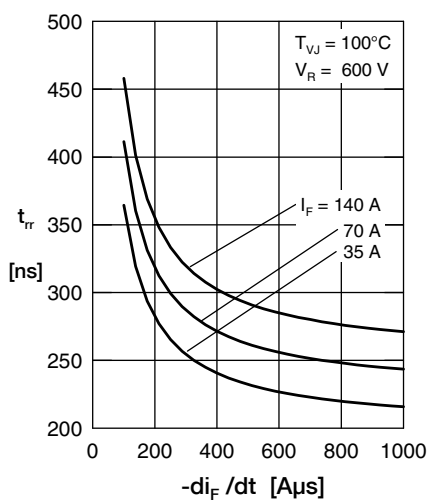


Fig. 5 Recovery time t_{rr} versus $-di_F/dt$

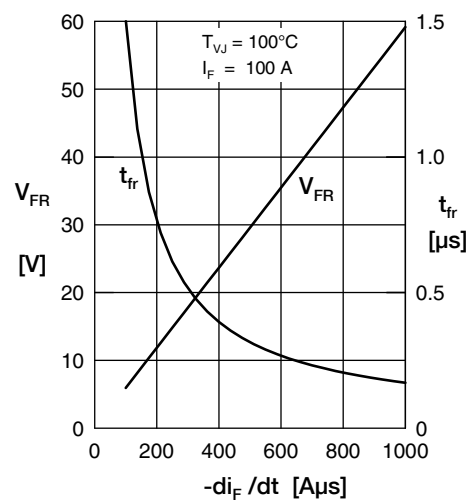


Fig. 6 Peak forward voltage V_{FR} and t_{fr} versus $-di_F/dt$

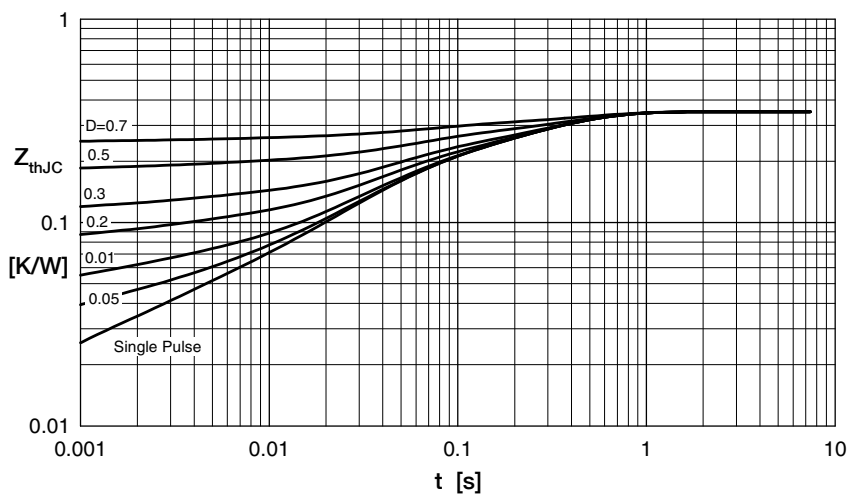
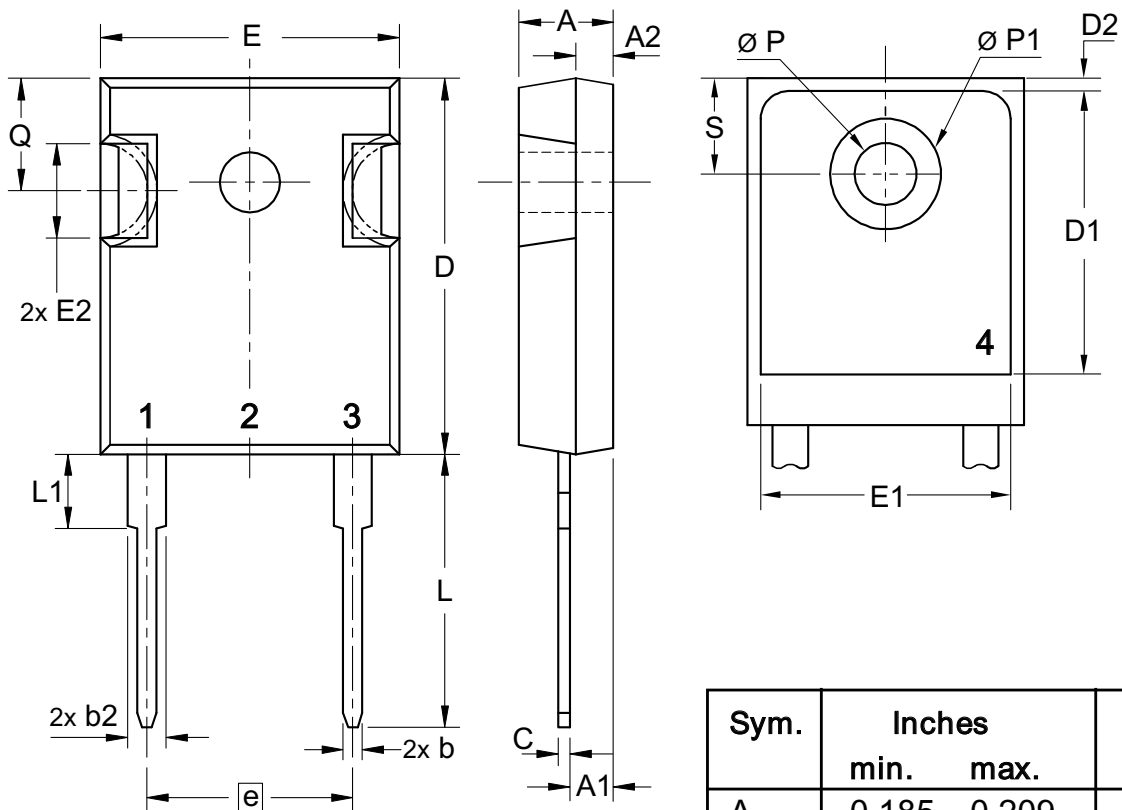


Fig. 7 Transient thermal resistance junction to case at various duty cycles

Constants for Z_{thJC} calculation:

i	R_{thi} (K/W)	t_i (s)
1	0.017	0.00038
2	0.0184	0.0026
3	0.1296	0.0387
4	0.185	0.274

Dimensions TO-247 AD




Sym.	Inches		Millimeter	
	min.	max.	min.	max.
A	0.185	0.209	4.70	5.30
A1	0.087	0.102	2.21	2.59
A2	0.059	0.098	1.50	2.49
D	0.819	0.845	20.79	21.45
E	0.610	0.640	15.48	16.24
E2	0.170	0.216	4.31	5.48
e	0.430 BSC		10.92 BSC	
L	0.780	0.800	19.80	20.30
L1	-	0.177	-	4.49
Ø P	0.140	0.144	3.55	3.65
Q	0.212	0.244	5.38	6.19
S	0.242 BSC		6.14 BSC	
b	0.039	0.055	0.99	1.40
b2	0.065	0.094	1.65	2.39
b4	0.102	0.135	2.59	3.43
c	0.015	0.035	0.38	0.89
D1	0.515	-	13.07	-
D2	0.020	0.053	0.51	1.35
E1	0.530	-	13.45	-
Ø P1	-	0.29	-	7.39

B.4 C44P-R

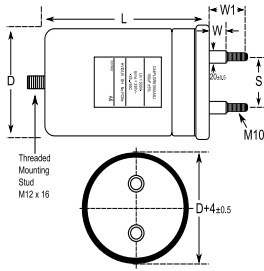
From [128]:

KEMET Part Number: C44PLGR6500RBSK



KEMET
a YAGEO company

C44P-R, Film, Metallized Polypropylene, AC Filter, 500 uF, 10%, 330 VAC, 700 VDC



Dimensions	
D	85mm +/-0.5mm
L	197mm +/-2mm
W	21mm +/-1mm
S	35mm +/-1mm
W1	45mm +/-1mm


Packaging Specifications	
Mounting:	Bolt - M12x16
Packaging:	Bulk, Bag

General Information	
Series:	C44P-R
Dielectric:	Metallized Polypropylene
Style:	Can
Features:	Single Phase PFC
RoHS:	With Exemptions
REACH:	SVHC (Pb – CAS 7439-92-1)
SCIP Number:	cc1c1ec4-db9e-4815-b26b-e8a34ddf776
Lead:	Threaded Studs M10
AEC-Q200:	No
Component Weight:	1300 g
Miscellaneous:	Thermal Resistance = 3.4 C/W.

Specifications	
Capacitance:	500 uF
Capacitance Tolerance:	10%
Voltage AC:	330 VAC
Voltage DC:	700 VDC
Temperature Range:	-25/+70°C
Rated Temperature:	70°C
Max dV/dt:	12.5 V/us
Resistance:	1.2 mOhms (10kHz)
Ripple Current:	63 Amps (10kHz 40C)
Inductance:	160 nH

Statements of suitability for certain applications are based on our knowledge of typical operating conditions for such applications, but are not intended to constitute - and we specifically disclaim - any warranty concerning suitability for a specific customer application or use. This information is intended for use only by customers who have the requisite experience and capability to determine the correct products for their application. Any technical advice inferred from this information or otherwise provided by us with reference to the use of our products is given gratis, and we assume no obligation or liability for the advice given or results obtained.

Generated 5/30/2022 - 9763175c-f0a6-44c8-aaf2-1df4ad3a4a72



KEMET
a YAGEO company

© 2006 - 2022 KEMET

B.5 IHXL-1500VZ-5A

From [130]:



www.vishay.com

IHXL-1500VZ-5A

Vishay Dale

High Current Through-Hole Inductor, High Temperature



FEATURES

- High temperature, up to 155 °C
- Shielded construction
- Frequency range up to 5.0 MHz
- Handles high transient current spikes without saturation
- Ultra low buzz noise, due to composite construction
- AEC-Q200 qualified
- Material categorization: for definitions of compliance please see www.vishay.com/doc?99912



APPLICATIONS

- Automotive high current filters
- Switching regulators
- In-line noise filters
- Differential mode choke
- Boost power factor correction choke
- 12 V, 24 V, 48 V DC/DC converters
- High current battery charging

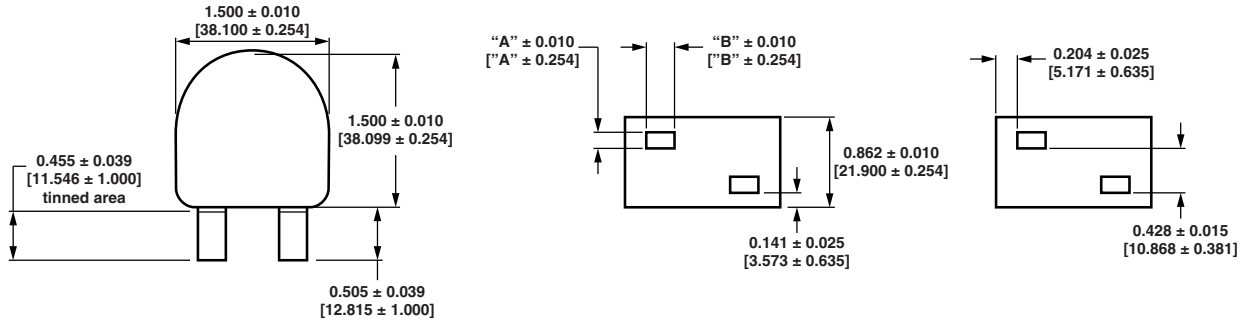
STANDARD ELECTRICAL SPECIFICATIONS						
L ₀ INDUCTANCE ± 20 % AT 500 kHz, 2 V, 0 A (μH)	DCR TYP. 25 °C (mΩ)	DCR MAX. 25 °C (mΩ)	HEAT RATING CURRENT DC TYP. (A) ⁽³⁾	HEAT RATING CURRENT DC TYP. (A) ⁽⁴⁾	SATURATION CURRENT DC TYP. (A) ⁽⁵⁾	SATURATION CURRENT DC TYP. (A) ⁽⁶⁾
0.68	0.12	0.13	154	235	301	420
0.82	0.17	0.18	132	196	235	332
1.5	0.25	0.26	120	178	138	193
2.2	0.32	0.34	115	168	104	150
3.3	0.40	0.42	96	150	87	124

Notes

- ⁽¹⁾ All test data is referenced to 25 °C ambient
- ⁽²⁾ Operating temperature range -55 °C to +155 °C
- ⁽³⁾ DC current (A) that will cause an approximate ΔT of 40 °C after one hour
- ⁽⁴⁾ DC current (A) that will cause an approximate ΔT of 100 °C after one hour
- ⁽⁵⁾ DC current (A) that will cause L₀ to drop approximately 20 %
- ⁽⁶⁾ DC current (A) that will cause L₀ to drop approximately 30 %
- ⁽⁷⁾ The part temperature (ambient + temp. rise) should not exceed 155 °C under worst case operating conditions. Circuit design, component placement, PWB trace size and thickness, airflow and other cooling provisions all affect the part temperature. Part temperature should be verified in the end application



DIMENSIONS in inches [millimeters]

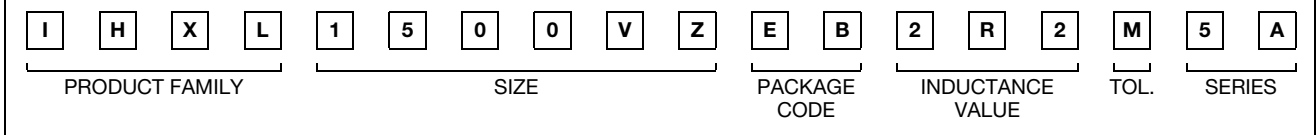


LEAD DIMENSIONS ± 0.010 [± 0.25]		
VALUE	A - HEIGHT	B - WIDTH
0.68	0.162 [4.11]	0.298 [7.34]
0.82	0.102 [2.59]	0.253 [6.43]
1.5	0.102 [2.59]	0.253 [6.43]
2.2	0.102 [2.59]	0.253 [6.43]
3.3	0.102 [2.59]	0.253 [6.43]

DESCRIPTION

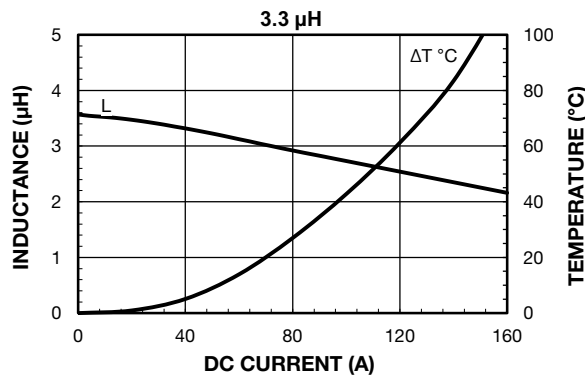
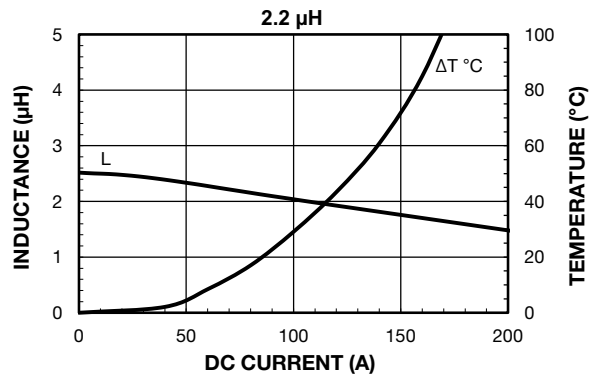
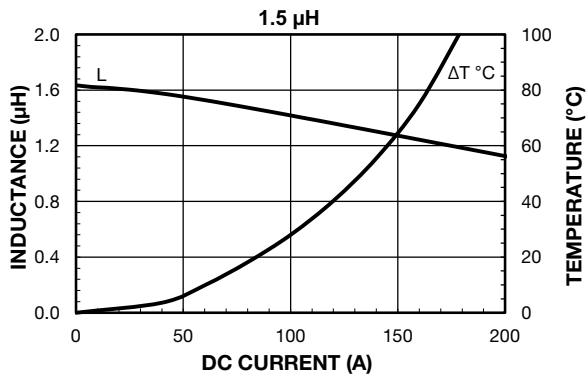
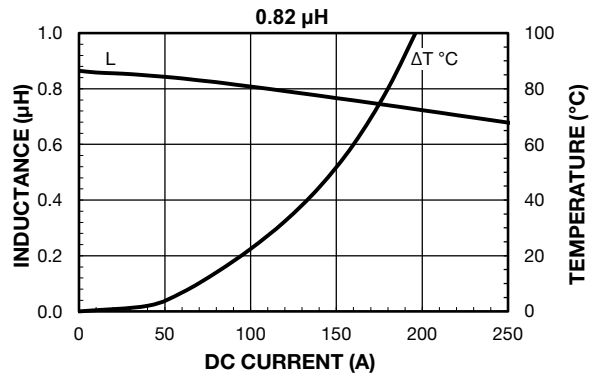
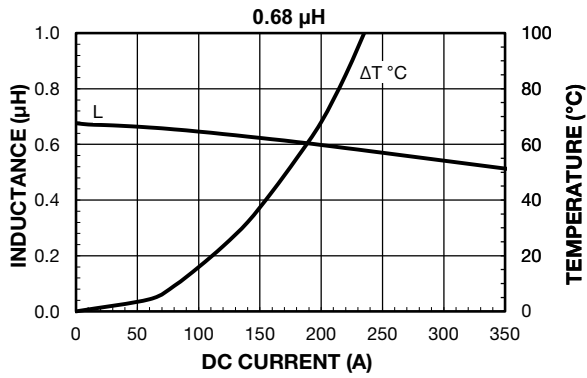
IHXL-1500VZ-5A	2.2 μH	± 20 %	EB	e3
MODEL	INDUCTANCE VALUE	INDUCTANCE TOLERANCE	PACKAGE CODE	JEDEC® LEAD (Pb)-FREE STANDARD

GLOBAL PART NUMBER



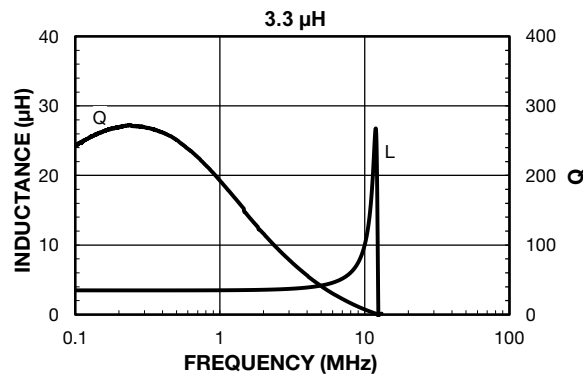
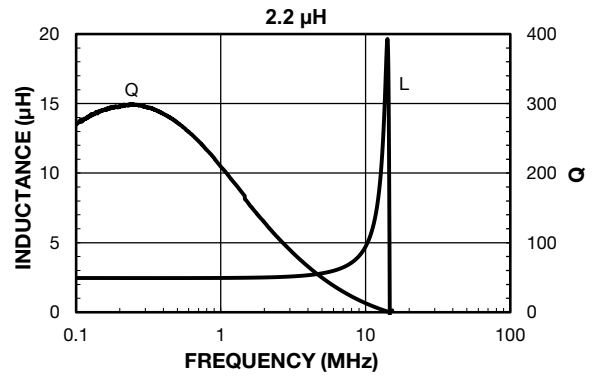
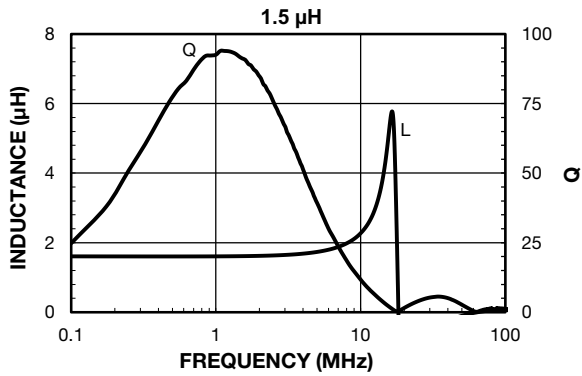
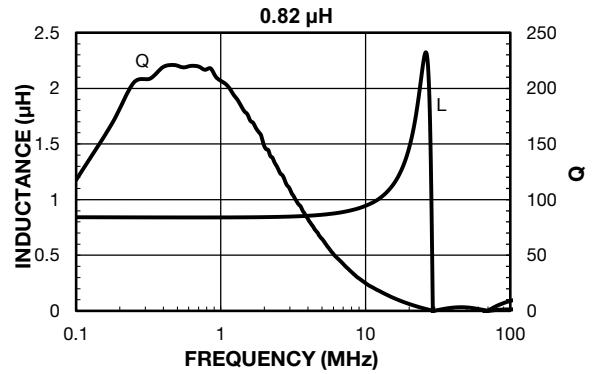
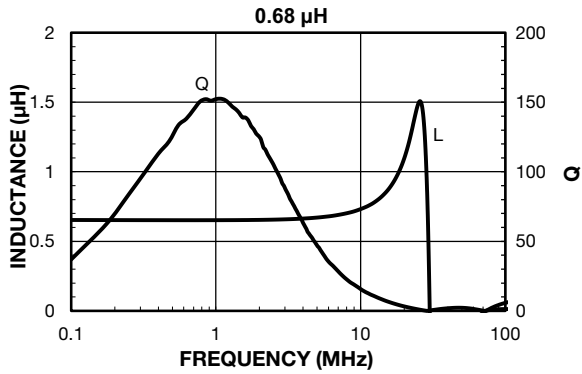


PERFORMANCE GRAPHS





PERFORMANCE GRAPHS: INDUCTANCE AND Q VS. FREQUENCY





Disclaimer

ALL PRODUCT, PRODUCT SPECIFICATIONS AND DATA ARE SUBJECT TO CHANGE WITHOUT NOTICE TO IMPROVE RELIABILITY, FUNCTION OR DESIGN OR OTHERWISE.

Vishay Intertechnology, Inc., its affiliates, agents, and employees, and all persons acting on its or their behalf (collectively, "Vishay"), disclaim any and all liability for any errors, inaccuracies or incompleteness contained in any datasheet or in any other disclosure relating to any product.

Vishay makes no warranty, representation or guarantee regarding the suitability of the products for any particular purpose or the continuing production of any product. To the maximum extent permitted by applicable law, Vishay disclaims (i) any and all liability arising out of the application or use of any product, (ii) any and all liability, including without limitation special, consequential or incidental damages, and (iii) any and all implied warranties, including warranties of fitness for particular purpose, non-infringement and merchantability.


Statements regarding the suitability of products for certain types of applications are based on Vishay's knowledge of typical requirements that are often placed on Vishay products in generic applications. Such statements are not binding statements about the suitability of products for a particular application. It is the customer's responsibility to validate that a particular product with the properties described in the product specification is suitable for use in a particular application. Parameters provided in datasheets and / or specifications may vary in different applications and performance may vary over time. All operating parameters, including typical parameters, must be validated for each customer application by the customer's technical experts. Product specifications do not expand or otherwise modify Vishay's terms and conditions of purchase, including but not limited to the warranty expressed therein.

Except as expressly indicated in writing, Vishay products are not designed for use in medical, life-saving, or life-sustaining applications or for any other application in which the failure of the Vishay product could result in personal injury or death. Customers using or selling Vishay products not expressly indicated for use in such applications do so at their own risk. Please contact authorized Vishay personnel to obtain written terms and conditions regarding products designed for such applications.

No license, express or implied, by estoppel or otherwise, to any intellectual property rights is granted by this document or by any conduct of Vishay. Product names and markings noted herein may be trademarks of their respective owners.

B.6 IXYH85N120A4

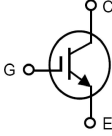
From [131]:



**1200V XPT™
GenX4™ IGBT**

Ultra Low-V_{sat} PT IGBT for
up to 5kHz Switching

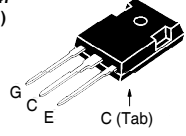
IXYH85N120A4



V_{CE(S)} = 1200V
I_{C110} = 85A
V_{CE(sat)} ≤ 1.8V
t_{fi(typ)} = 280ns

Symbol	Test Conditions	Maximum Ratings	
V _{CE(S)}	T _J = 25°C to 175°C	1200	V
V _{CGR}	T _J = 25°C to 175°C, R _{GE} = 1MΩ	1200	V
V _{GES}	Continuous	±20	V
V _{GEM}	Transient	±30	V
I _{C25}	T _C = 25°C (Chip Capability)	300	A
I _{L(RMS)}	Terminal Current Limit	160	A
I _{C110}	T _C = 110°C	85	A
I _{CM}	T _C = 25°C, 1ms	520	A
SSOA	V _{GE} = 15V, T _{VJ} = 125°C, R _G = 5Ω	I _{CM} = 170	A
(RBSOA)	Clamped Inductive Load	V _{CE} ≤ 0.8 • V _{CE(S)}	
P _C	T _C = 25°C	1150	W
T _J		-55 ... +175	°C
T _{JM}		175	°C
T _{sig}		-55 ... +175	°C
T _L	Maximum Lead Temperature for Soldering 1.6 mm (0.062 in.) from Case for 10s	300	°C
M _d	Mounting Torque	1.13 / 10	Nm/lb.in
Weight		6	g

**TO-247
(IXYH)**



G = Gate C = Collector
E = Emitter Tab = Collector

Features

- Optimized for Low Conduction Losses
- Positive Thermal Coefficient of V_{ce(sat)}
- International Standard Package

Advantages

- High Power Density
- Low Gate Drive Requirement

Applications

- Power Inverters
- UPS
- Motor Drives
- SMPS
- PFC Circuits
- Battery Chargers
- Welding Machines
- Lamp Ballasts
- Inrush Current Protector Circuits

Symbol	Test Conditions (T _J = 25°C, Unless Otherwise Specified)	Characteristic Values		
		Min.	Typ.	Max.
BV _{CE(S)}	I _C = 250μA, V _{GE} = 0V	1200		V
V _{GE(th)}	I _C = 250μA, V _{CE} = V _{GE}	4.0		6.5 V
I _{CE(S)}	V _{CE} = V _{CE(S)} , V _{GE} = 0V T _J = 150°C			10 μA 5 mA
I _{GES}	V _{CE} = 0V, V _{GE} = ±20V			±100 nA
V _{CE(sat)}	I _C = 85A, V _{GE} = 15V, Note 1 T _J = 150°C	1.5	1.7	1.8 V V

©2020 Littelfuse Inc.

DS100984C(4/20)

Symbol Test Conditions ($T_J = 25^\circ\text{C}$ Unless Otherwise Specified)		Characteristic Values		
		Min.	Typ.	Max.
g_{fs}	$I_C = 60\text{A}, V_{CE} = 10\text{V}, \text{Note 1}$	46	60	S
C_{ies}	$V_{CE} = 25\text{V}, V_{GE} = 0\text{V}, f = 1\text{MHz}$		3700	pF
C_{oes}			210	pF
C_{res}			140	pF
$Q_{g(on)}$	$I_C = 85\text{A}, V_{GE} = 15\text{V}, V_{CE} = 0.5 \cdot V_{CES}$		200	nC
Q_{ge}			30	nC
Q_{gc}			80	nC
$t_{d(on)}$	Inductive load, $T_J = 25^\circ\text{C}$ $I_C = 60\text{A}, V_{GE} = 15\text{V}$ $V_{CE} = 0.5 \cdot V_{CES}, R_G = 5\Omega$ Note 2		40	ns
t_{ri}			40	ns
E_{on}			4.9	mJ
$t_{d(off)}$			400	ns
t_{fi}			280	ns
E_{off}			8.3	mJ
$t_{d(on)}$	Inductive load, $T_J = 150^\circ\text{C}$ $I_C = 60\text{A}, V_{GE} = 15\text{V}$ $V_{CE} = 0.5 \cdot V_{CES}, R_G = 5\Omega$ Note 2		30	ns
t_{ri}			43	ns
E_{on}			8.3	mJ
$t_{d(off)}$			460	ns
t_{fi}			530	ns
E_{off}			13.7	mJ
R_{thJC}			0.13	$^\circ\text{C/W}$
R_{thCS}		0.21		$^\circ\text{C/W}$

Notes:

1. Pulse test, $t \leq 300\mu\text{s}$, duty cycle, $d \leq 2\%$.
2. Switching times & energy losses may increase for higher $V_{CE}(\text{clamp})$, T_J or R_G .

Littelfuse Reserves the Right to Change Limits, Test Conditions, and Dimensions.

IXYS MOSFETs and IGBTs are covered	4,835,592	4,931,844	5,049,961	5,237,481	6,162,665	6,404,065 B1	6,683,344	6,727,585	7,005,734 B2	7,157,338B2
by one or more of the following U.S. patents:	4,860,072	5,017,508	5,063,307	5,381,025	6,259,123 B1	6,534,343	6,710,405 B2	6,759,692	7,063,975 B2	
	4,881,106	5,034,796	5,187,117	5,486,715	6,306,728 B1	6,583,505	6,710,463	6,771,478 B2	7,071,537	

Fig. 1. Output Characteristics @ $T_J = 25^\circ\text{C}$

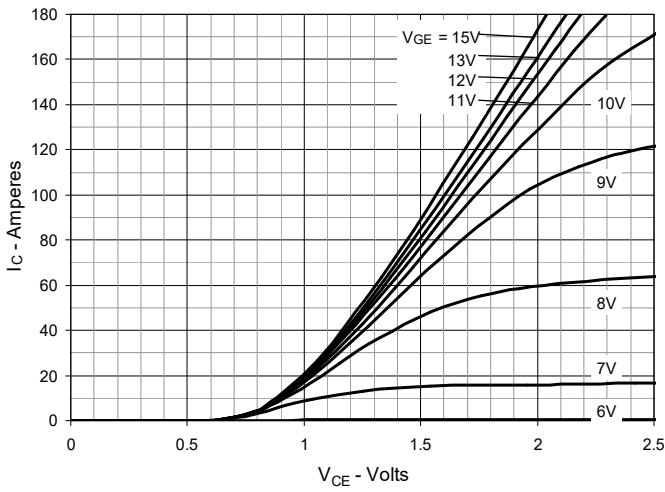


Fig. 2. Extended Output Characteristics @ $T_J = 25^\circ\text{C}$

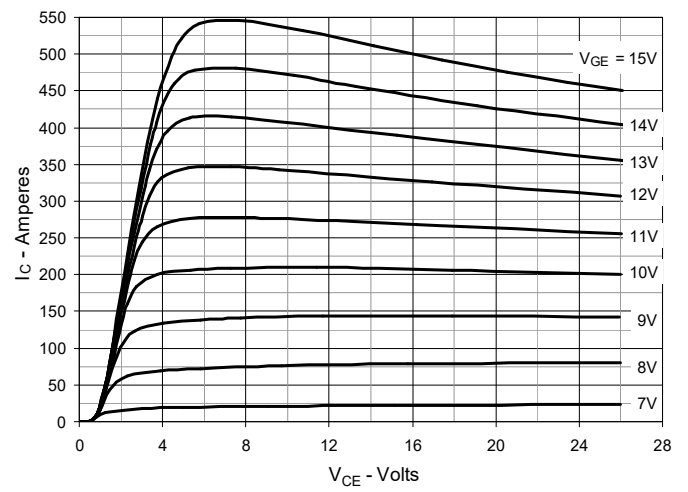


Fig. 3. Output Characteristics @ $T_J = 150^\circ\text{C}$

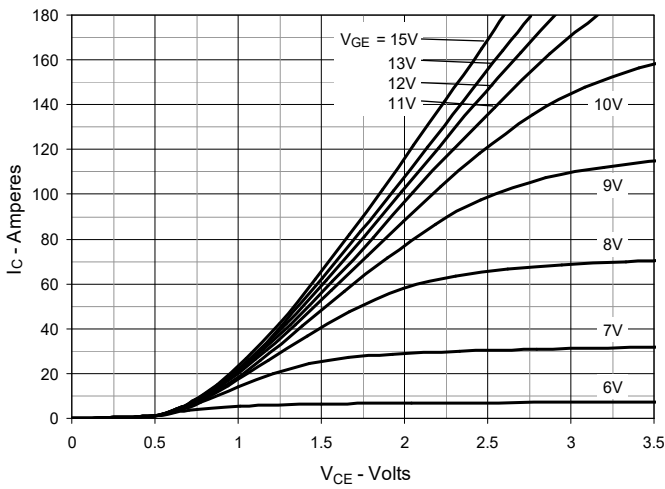


Fig. 4. Dependence of $V_{CE(sat)}$ on Junction Temperature

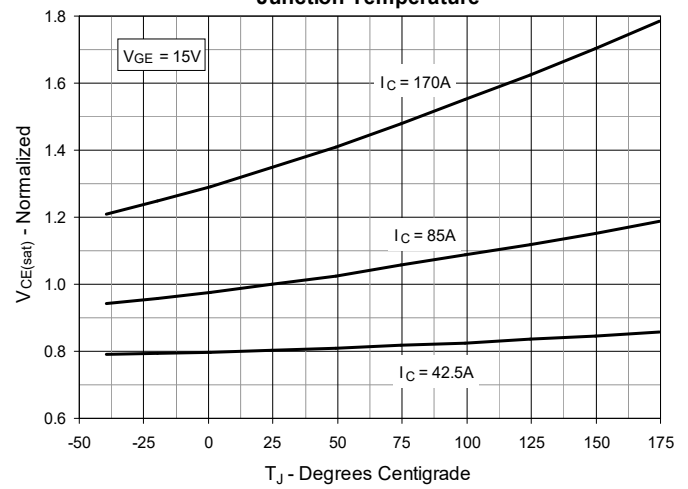


Fig. 5. Collector-to-Emitter Voltage vs. Gate-to-Emitter Voltage

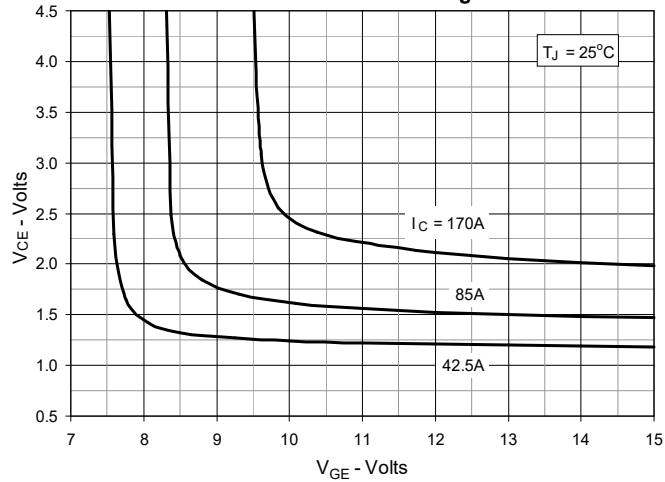


Fig. 6. Input Admittance

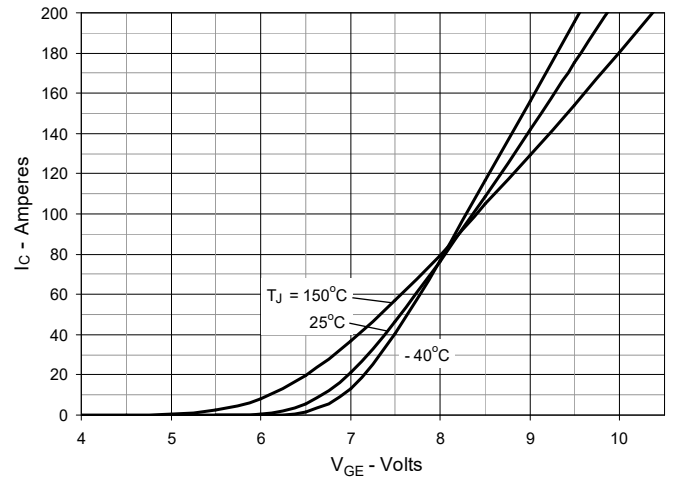


Fig. 7. Transconductance

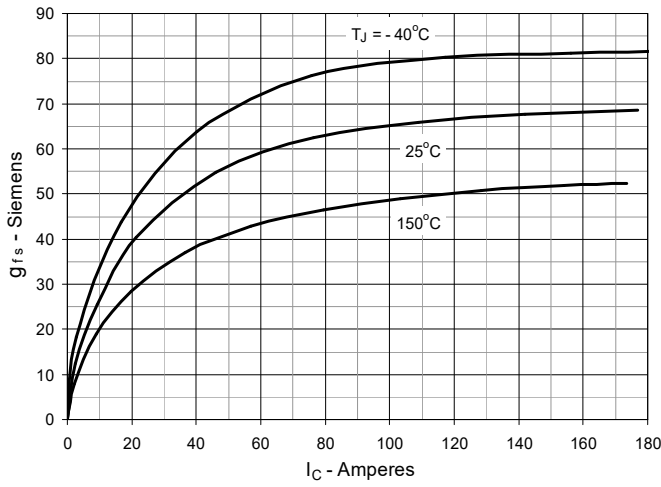


Fig. 8. Gate Charge

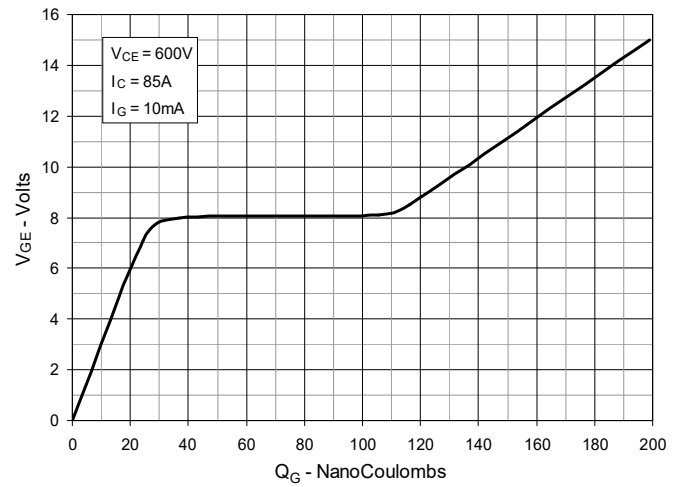


Fig. 9. Capacitance

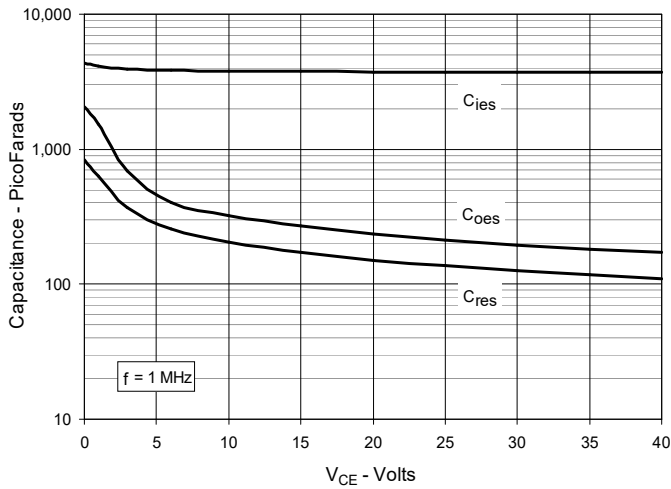


Fig. 10. Reverse-Bias Safe Operating Area

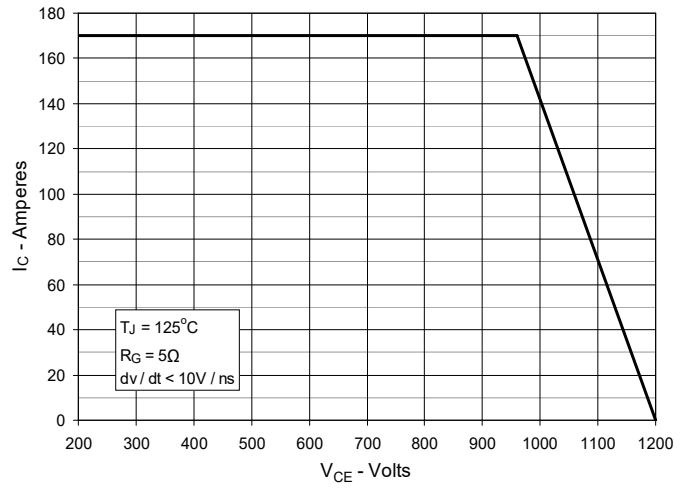


Fig. 11. Maximum Transient Thermal Impedance

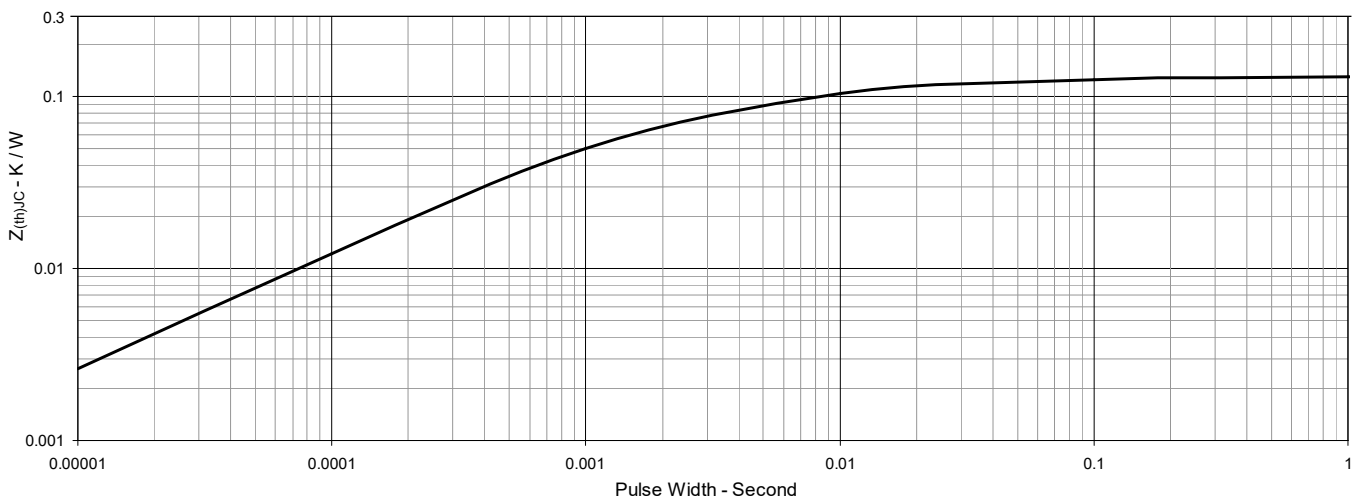


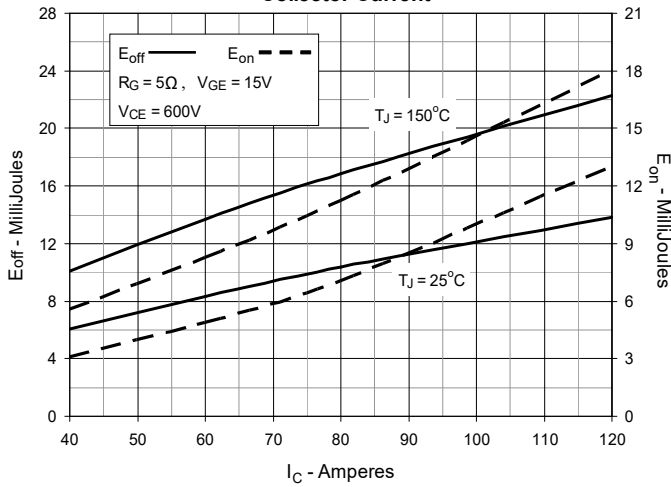
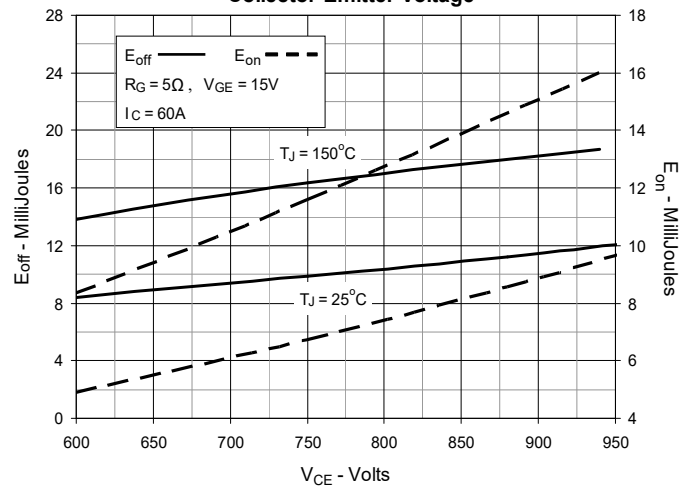
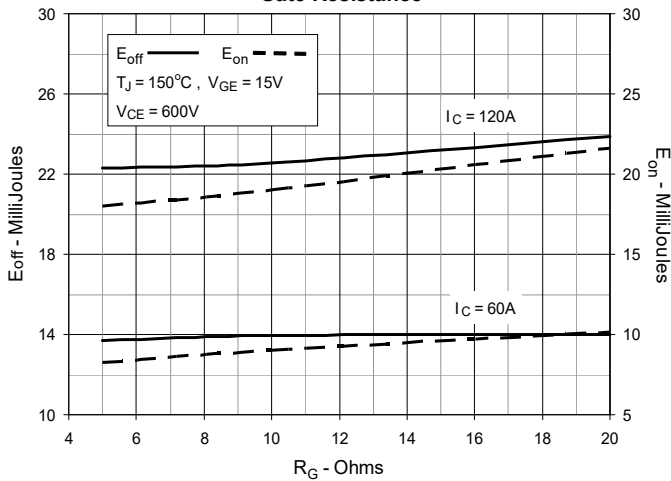
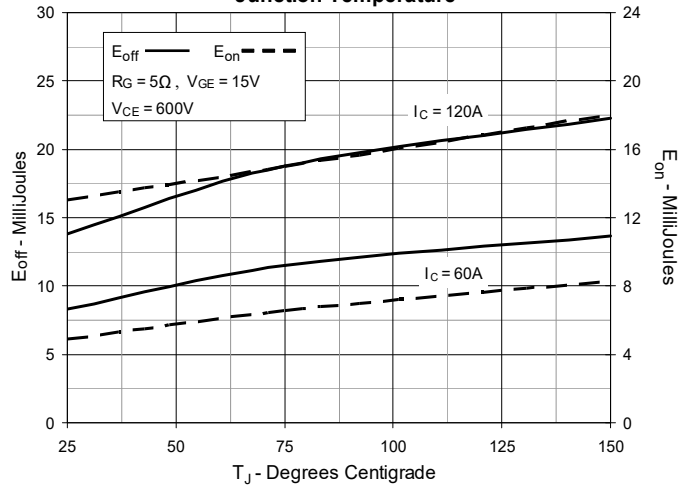
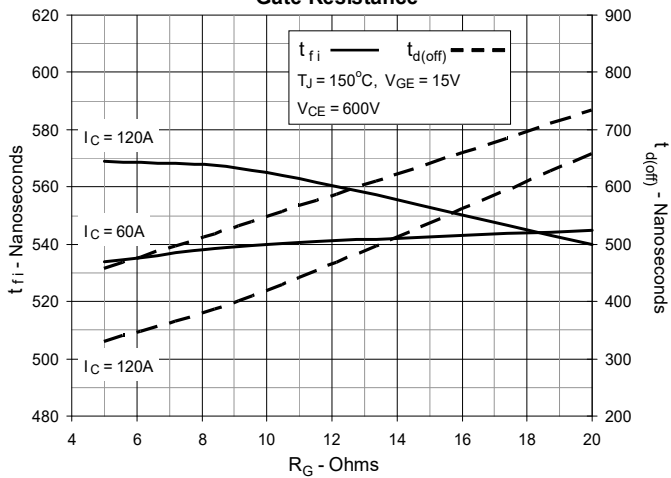
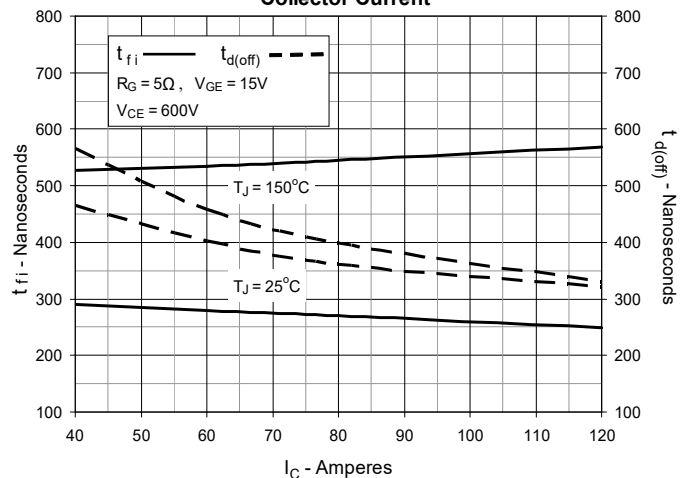
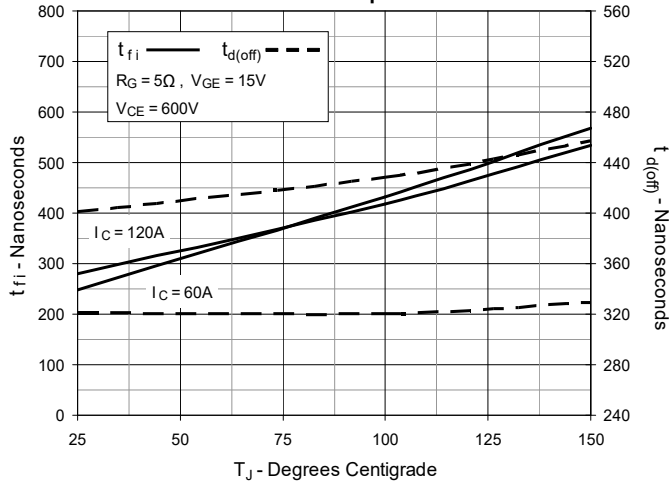
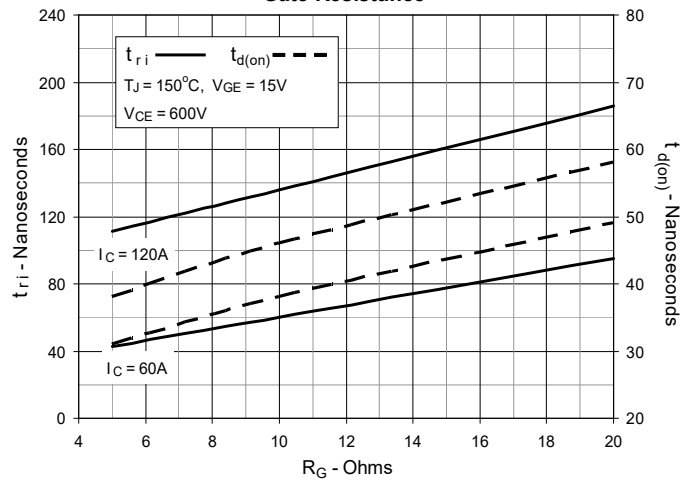
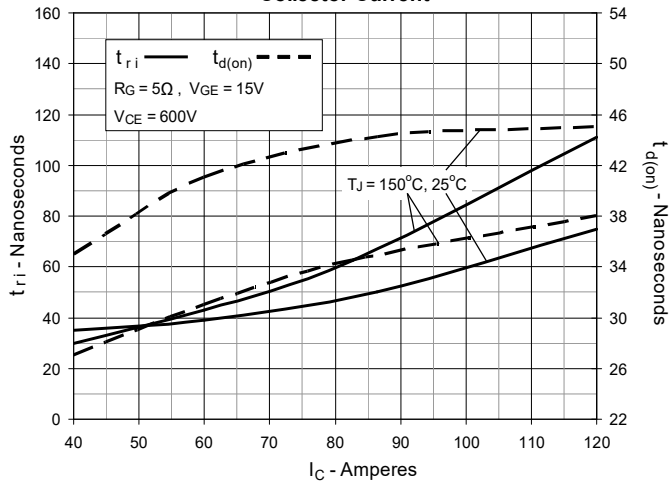
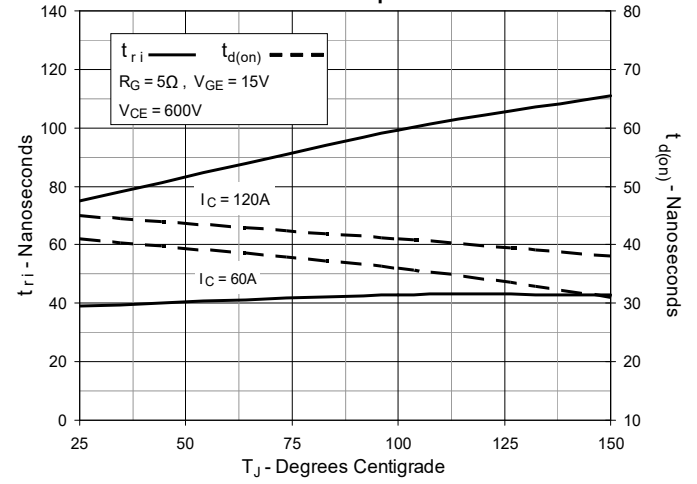
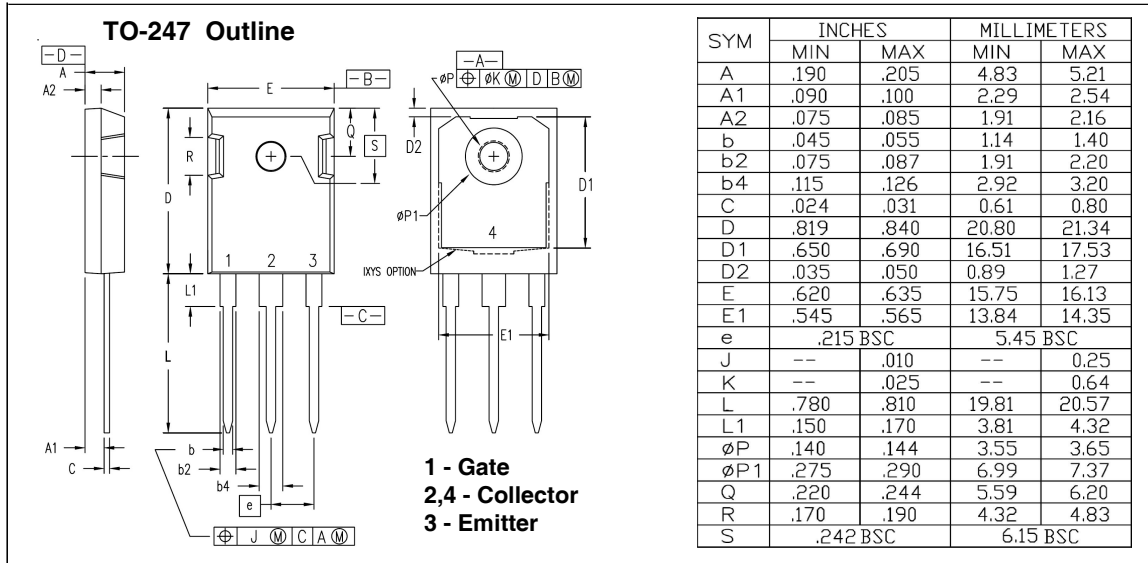
Fig. 12. Inductive Switching Energy Loss vs. Collector Current

Fig. 13. Inductive Switching Energy Loss vs. Collector-Emitter Voltage

Fig. 14. Inductive Switching Energy Loss vs. Gate Resistance

Fig. 15. Inductive Switching Energy Loss vs. Junction Temperature

Fig. 16. Inductive Turn-off Switching Times vs. Gate Resistance

Fig. 17. Inductive Turn-off Switching Times vs. Collector Current


Fig. 18. Inductive Turn-off Switching Times vs. Junction Temperature

Fig. 19. Inductive Turn-on Switching Times vs. Gate Resistance

Fig. 20. Inductive Turn-on Switching Times vs. Collector Current

Fig. 21. Inductive Turn-on Switching Times vs. Junction Temperature






Disclaimer Notice - Information furnished is believed to be accurate and reliable. However, users should independently evaluate the suitability of and test each product selected for their own applications. Littelfuse products are not designed for, and may not be used in, all applications. Read complete Disclaimer Notice at www.littelfuse.com/disclaimer-electronics.

Littelfuse Reserves the Right to Change Limits, Test Conditions, and Dimensions.

B.7 FGH40T120SQDNL4

From [132]:

FGH40T120SQDNL4

IGBT - Ultra Field Stop

This Insulated Gate Bipolar Transistor (IGBT) features a robust and cost effective Ultra Field Stop Trench construction, and provides superior performance in demanding switching applications, offering both low on-state voltage and minimal switching loss. The IGBT is well suited for UPS and solar applications. Incorporated into the device is a soft and fast co-packaged free wheeling diode with a low forward voltage.

Features

- Extremely Efficient Trench with Field Stop Technology
- $T_{jmax} = 175^{\circ}\text{C}$
- Soft Fast Reverse Recovery Diode
- Optimized for High Speed Switching
- These are Pb-Free Devices

Typical Applications

- Solar Inverter
- Uninterruptible Power Inverter Supplies (UPS)
- Welding

ABSOLUTE MAXIMUM RATINGS

Rating	Symbol	Value	Unit
Collector-emitter voltage	V_{CES}	1200	V
Collector current @ $T_c = 25^{\circ}\text{C}$ @ $T_c = 100^{\circ}\text{C}$	I_C	160 40	A
Pulsed collector current, T_{pulse} limited by T_{jmax}	I_{CM}	160	A
Diode forward current @ $T_c = 25^{\circ}\text{C}$ @ $T_c = 100^{\circ}\text{C}$	I_F	160 40	A
Diode pulsed current, T_{pulse} limited by T_{jmax}	I_{FM}	160	A
Gate-emitter voltage Transient gate-emitter voltage ($T_{pulse} = 5 \mu\text{s}$, $D < 0.10$)	V_{GE}	± 20 ± 30	V
Power Dissipation @ $T_c = 25^{\circ}\text{C}$ @ $T_c = 100^{\circ}\text{C}$	P_D	454 227	W
Operating junction temperature range	T_J	-55 to +175	$^{\circ}\text{C}$
Storage temperature range	T_{stg}	-55 to +175	$^{\circ}\text{C}$
Lead temperature for soldering, 1/8" from case for 5 seconds	T_{SLD}	260	$^{\circ}\text{C}$

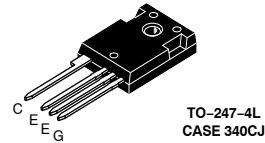
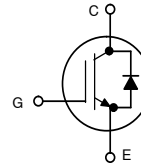
Stresses exceeding those listed in the Maximum Ratings table may damage the device. If any of these limits are exceeded, device functionality should not be assumed, damage may occur and reliability may be affected.



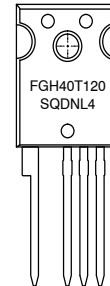
ON Semiconductor®

www.onsemi.com

40 A, 1200 V
 $V_{CEsat} = 1.7 \text{ V}$
 $E_{off} = 1.1 \text{ mJ}$



MARKING DIAGRAM



ORDERING INFORMATION

Device	Package	Shipping
FGH40T120SQDNL4	TO-247 (Pb-Free)	30 Units / Rail

FGH40T120SQDNL4

THERMAL CHARACTERISTICS

Rating	Symbol	Value	Unit
Thermal resistance junction-to-case, for IGBT	$R_{\theta JC}$	0.33	$^{\circ}\text{C}/\text{W}$
Thermal resistance junction-to-case, for Diode	$R_{\theta JC}$	0.61	$^{\circ}\text{C}/\text{W}$
Thermal resistance junction-to-ambient	$R_{\theta JA}$	40	$^{\circ}\text{C}/\text{W}$

ELECTRICAL CHARACTERISTICS ($T_J = 25^{\circ}\text{C}$ unless otherwise specified)

Parameter	Test Conditions	Symbol	Min	Typ	Max	Unit
-----------	-----------------	--------	-----	-----	-----	------

STATIC CHARACTERISTIC

Collector-emitter breakdown voltage, gate-emitter short-circuited	$V_{GE} = 0\text{ V}, I_C = 500\ \mu\text{A}$	$V_{(BR)CES}$	1200 1250*	-	-	V
Collector-emitter saturation voltage	$V_{GE} = 15\text{ V}, I_C = 40\text{ A}$ $V_{GE} = 15\text{ V}, I_C = 40\text{ A}, T_J = 175^{\circ}\text{C}$	V_{CEsat}	-	1.78 2.3	1.95	V
Gate-emitter threshold voltage	$V_{GE} = V_{CE}, I_C = 400\ \mu\text{A}$	$V_{GE(th)}$	4.5	5.5	6.5	V
Collector-emitter cut-off current, gate-emitter short-circuited	$V_{GE} = 0\text{ V}, V_{CE} = 1200\text{ V}$ $V_{GE} = 0\text{ V}, V_{CE} = 1200\text{ V}, T_J = 175^{\circ}\text{C}$	I_{CES}	-	-	0.4	mA
Gate leakage current, collector-emitter short-circuited	$V_{GE} = 20\text{ V}, V_{CE} = 0\text{ V}$	I_{GES}	-	-	200	nA

* Guaranteed by design.

Input capacitance	$V_{CE} = 20\text{ V}, V_{GE} = 0\text{ V}, f = 1\text{ MHz}$	C_{ies}	-	5000	-	pF
Output capacitance		C_{oes}	-	140	-	
Reverse transfer capacitance		C_{res}	-	80	-	
Gate charge total	$V_{CE} = 600\text{ V}, I_C = 40\text{ A}, V_{GE} = 15\text{ V}$	Q_g	-	221	-	nC
Gate to emitter charge		Q_{ge}	-	52	-	
Gate to collector charge		Q_{gc}	-	100	-	

SWITCHING CHARACTERISTIC, INDUCTIVE LOAD

Turn-on delay time	$T_J = 25^{\circ}\text{C}$ $V_{CC} = 600\text{ V}, I_C = 40\text{ A}$ $R_g = 10\ \Omega$ $V_{GE} = 0\text{ to }15\text{ V}$	$t_{d(on)}$	-	46	-	ns
Rise time		t_r	-	33	-	
Turn-off delay time		$t_{d(off)}$	-	220	-	
Fall time		t_f	-	56	-	mJ
Turn-on switching loss		E_{on}	-	1.4	-	
Turn-off switching loss		E_{off}	-	1.1	-	
Total switching loss	E_{ts}	-	2.5	-		
Turn-on delay time	$T_J = 175^{\circ}\text{C}$ $V_{CC} = 600\text{ V}, I_C = 40\text{ A}$ $R_g = 10\ \Omega$ $V_{GE} = 0\text{ to }15\text{ V}$	$t_{d(on)}$	-	47	-	ns
Rise time		t_r	-	33	-	
Turn-off delay time		$t_{d(off)}$	-	240	-	
Fall time		t_f	-	132	-	mJ
Turn-on switching loss		E_{on}	-	2.7	-	
Turn-off switching loss		E_{off}	-	1.8	-	
Total switching loss	E_{ts}	-	4.5	-		

DIODE CHARACTERISTIC

Forward voltage	$V_{GE} = 0\text{ V}, I_F = 40\text{ A}$ $V_{GE} = 0\text{ V}, I_F = 40\text{ A}, T_J = 175^{\circ}\text{C}$	V_F	-	3.4 3.1	3.8	V
Reverse recovery time	$T_J = 25^{\circ}\text{C}$ $I_F = 40\text{ A}, V_R = 400\text{ V}$ $di_F/dt = 500\text{ A}/\mu\text{s}$	t_{rr}	-	166	-	ns
Reverse recovery charge		Q_{rr}	-	0.78	-	μC
Reverse recovery current		I_{rrm}	-	9.0	-	A
Reverse recovery time	$T_J = 125^{\circ}\text{C}$ $I_F = 40\text{ A}, V_R = 400\text{ V}$ $di_F/dt = 500\text{ A}/\mu\text{s}$	t_{rr}	-	390	-	ns
Reverse recovery charge		Q_{rr}	-	4.0	-	μC
Reverse recovery current		I_{rrm}	-	20	-	A

Product parametric performance is indicated in the Electrical Characteristics for the listed test conditions, unless otherwise noted. Product performance may not be indicated by the Electrical Characteristics if operated under different conditions.

FGH40T120SQDNL4

TYPICAL CHARACTERISTICS

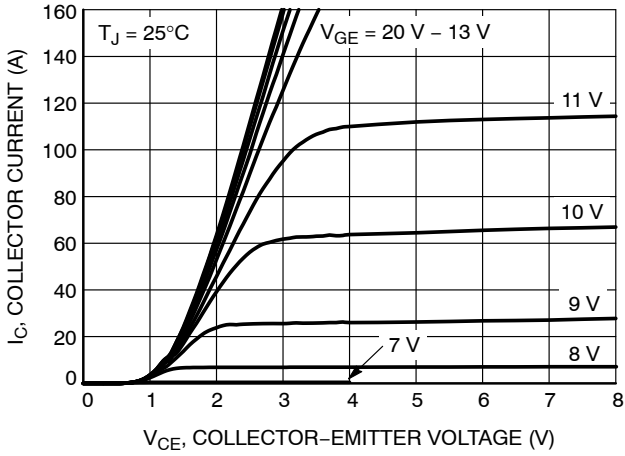


Figure 1. Output Characteristics

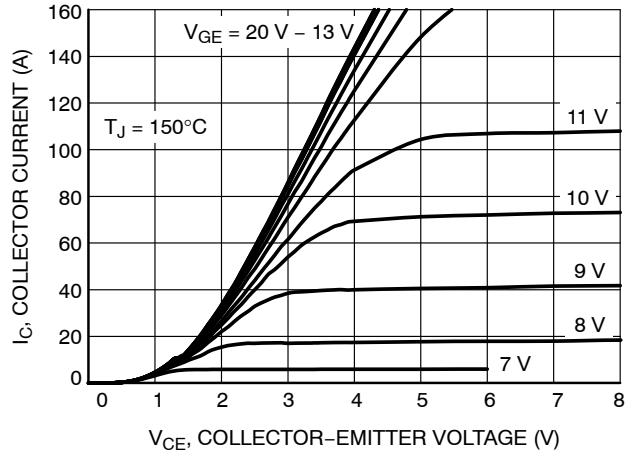


Figure 2. Output Characteristics

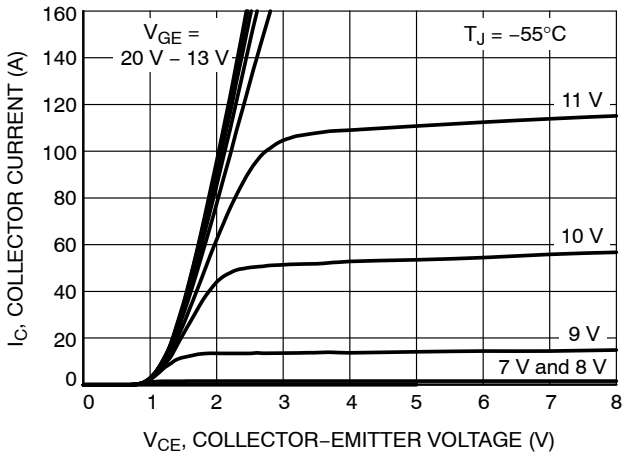


Figure 3. Output Characteristics

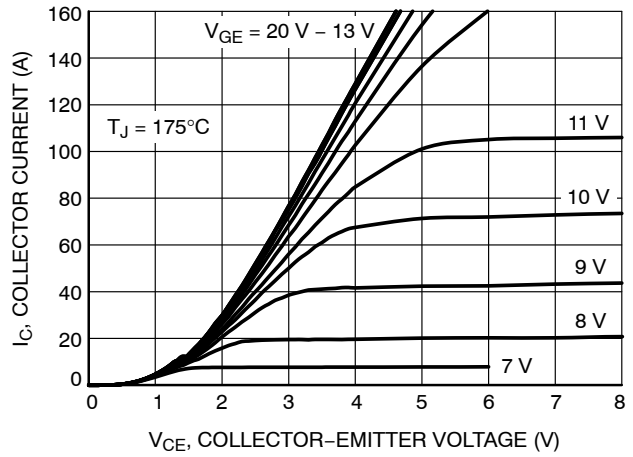


Figure 4. Output Characteristics

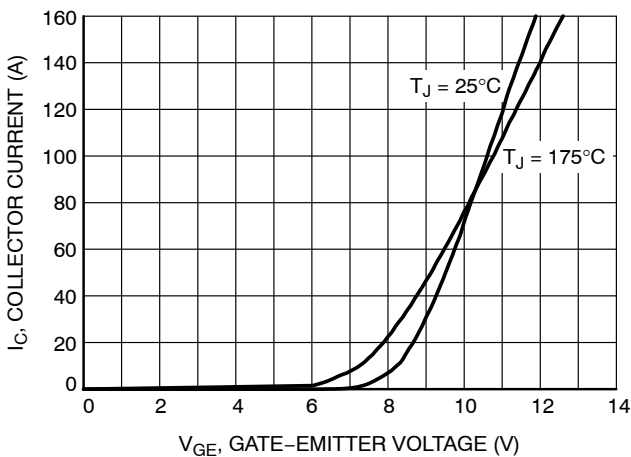


Figure 5. Typical Transfer Characteristics

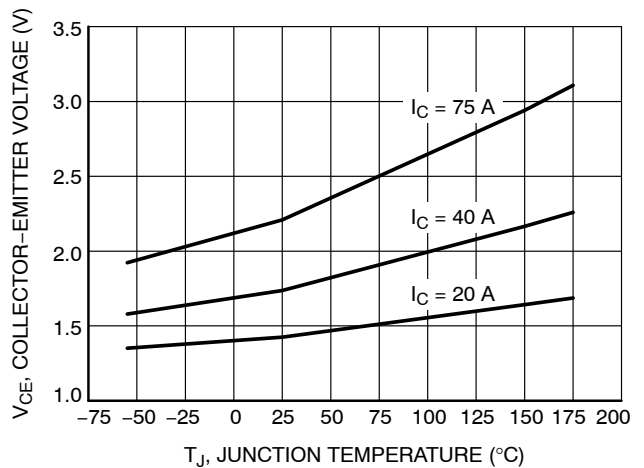


Figure 6. $V_{CE(sat)}$ vs. T_J

FGH40T120SQDNL4

TYPICAL CHARACTERISTICS

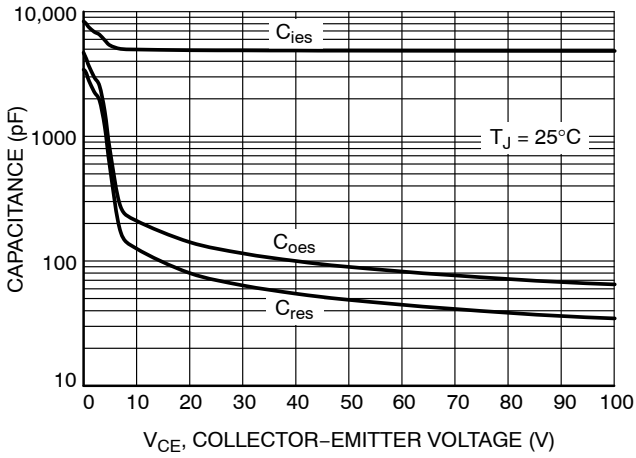


Figure 7. Typical Capacitance

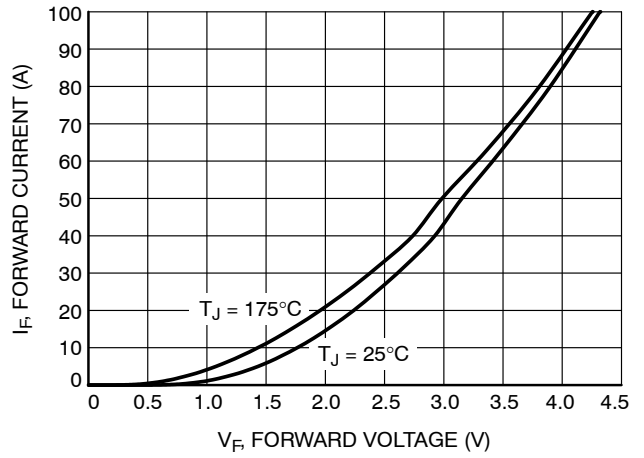


Figure 8. Diode Forward Characteristics

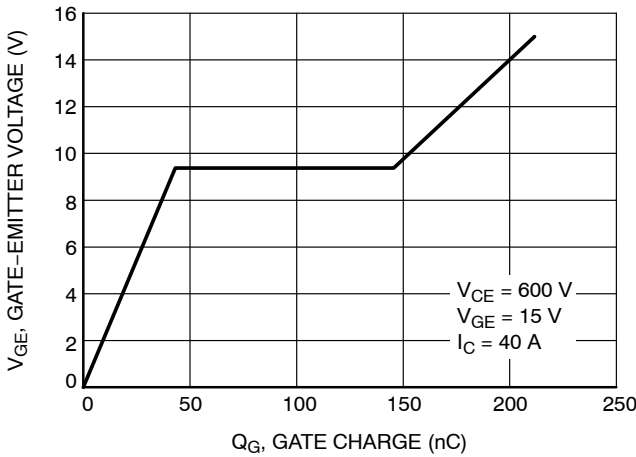


Figure 9. Typical Gate Charge

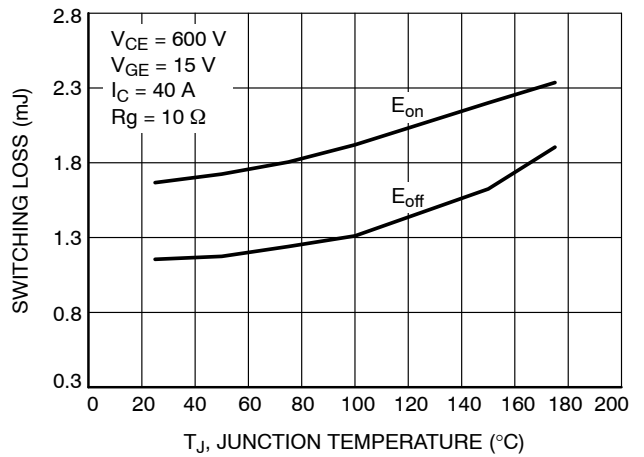


Figure 10. Switching Loss vs. Temperature

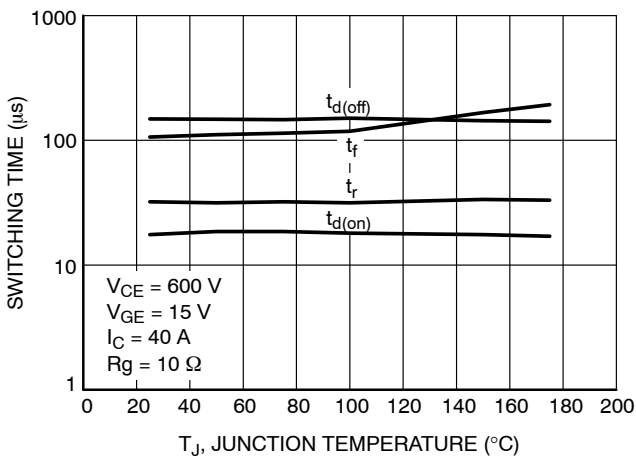


Figure 11. Switching Time vs. Temperature

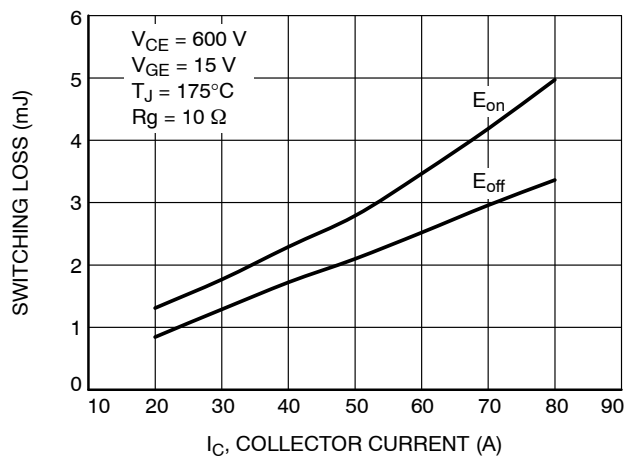


Figure 12. Switching Loss vs. I_C

FGH40T120SQDNL4

TYPICAL CHARACTERISTICS

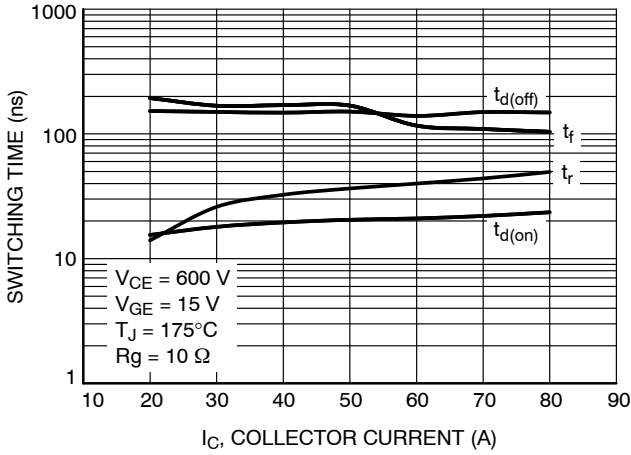


Figure 13. Switching Time vs. I_C

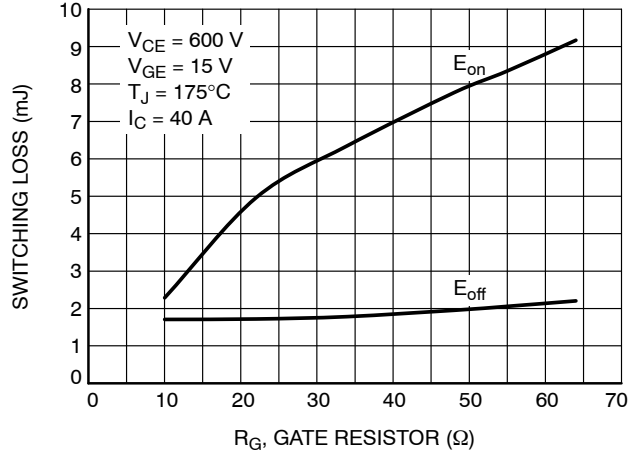


Figure 14. Switching Loss vs. R_G

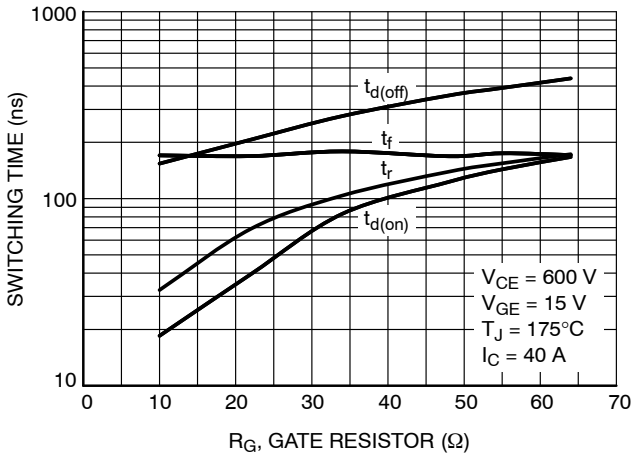


Figure 15. Switching Time vs. R_G

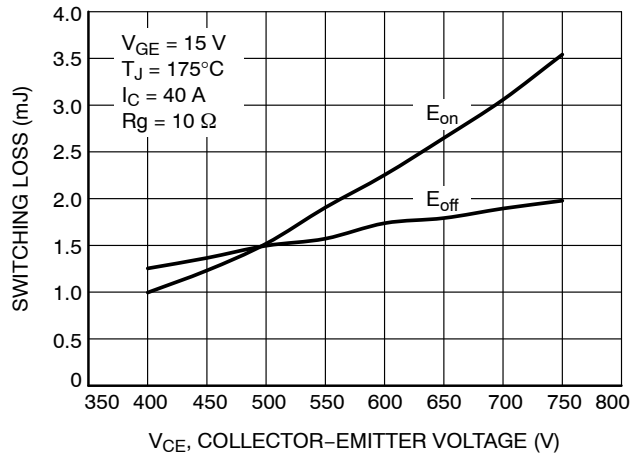


Figure 16. Switching Loss vs. V_{CE}

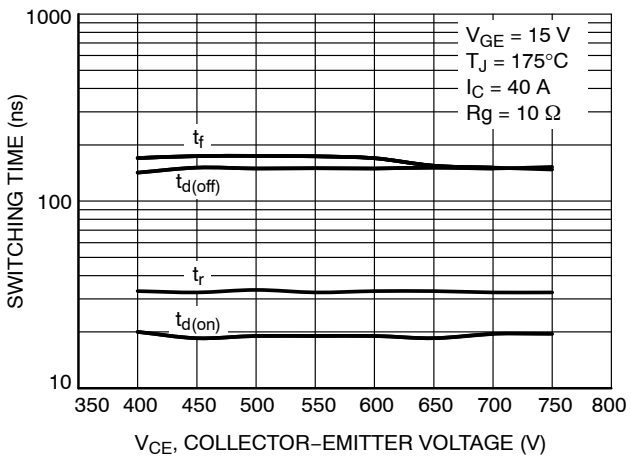


Figure 17. Switching Time vs. V_{CE}

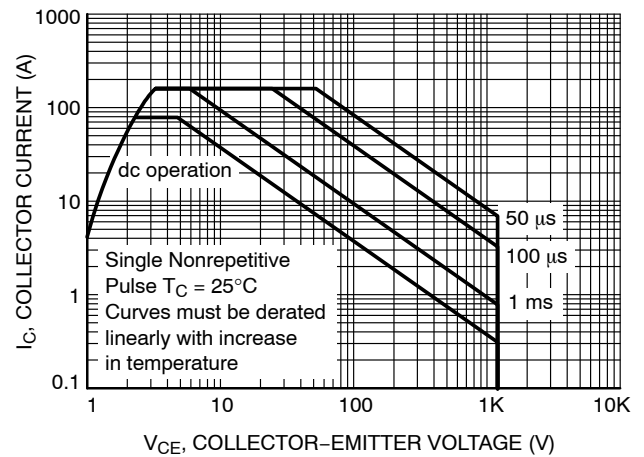


Figure 18. Safe Operating Area

FGH40T120SQDNL4

TYPICAL CHARACTERISTICS

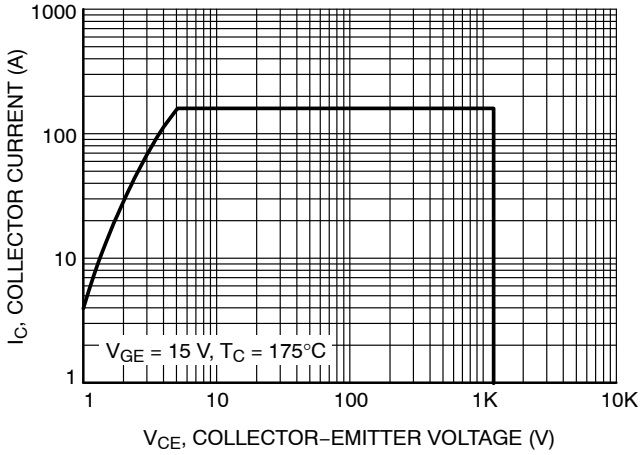


Figure 19. Reverse Bias Safe Operating Area

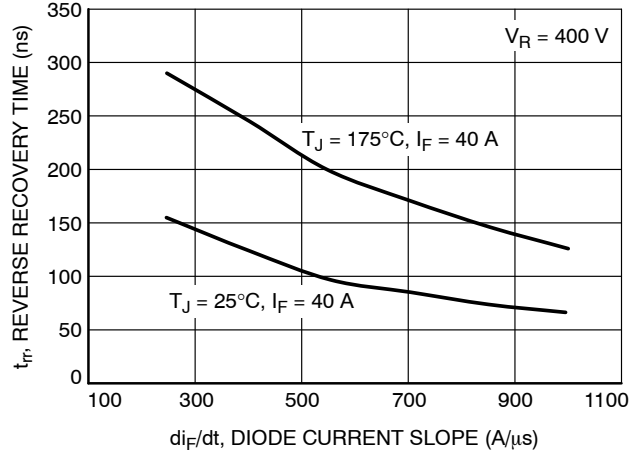


Figure 20. t_{rr} vs. di_F/dt

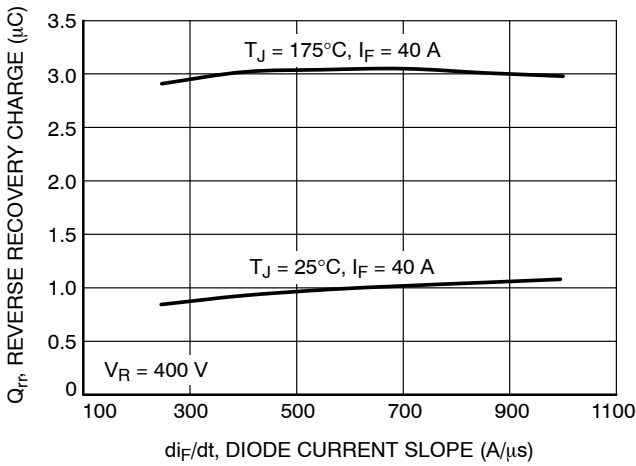


Figure 21. Q_{rr} vs. di_F/dt

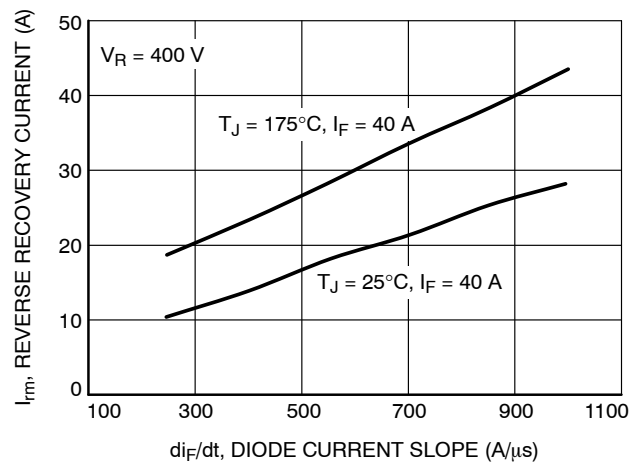


Figure 22. I_{rrm} vs. di_F/dt

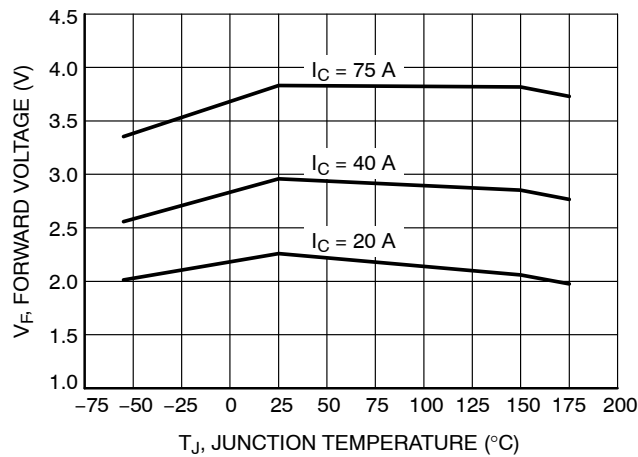


Figure 23. V_F vs. T_J

FGH40T120SQDNL4

TYPICAL CHARACTERISTICS

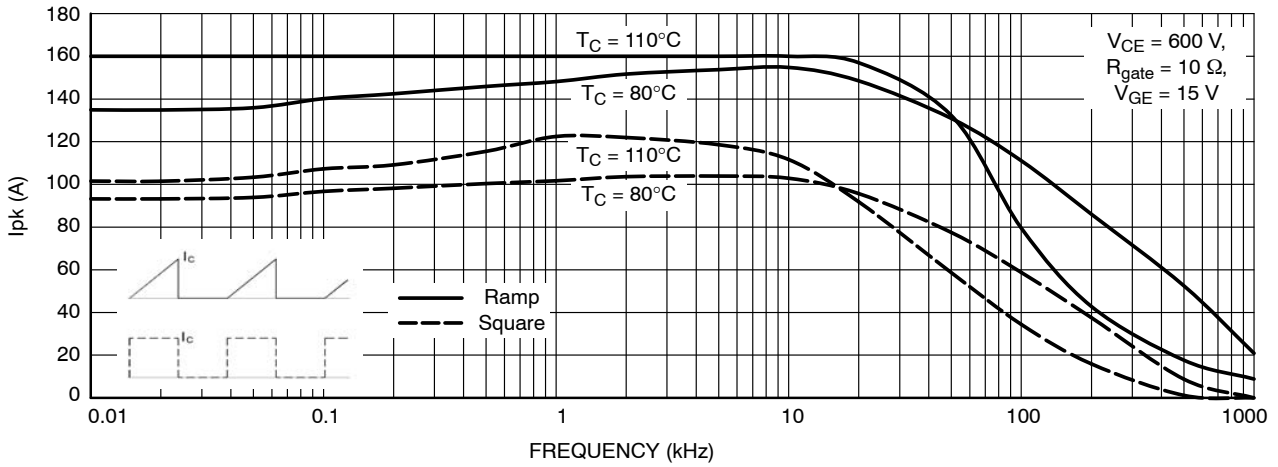


Figure 24. Collector Current vs. Switching Frequency

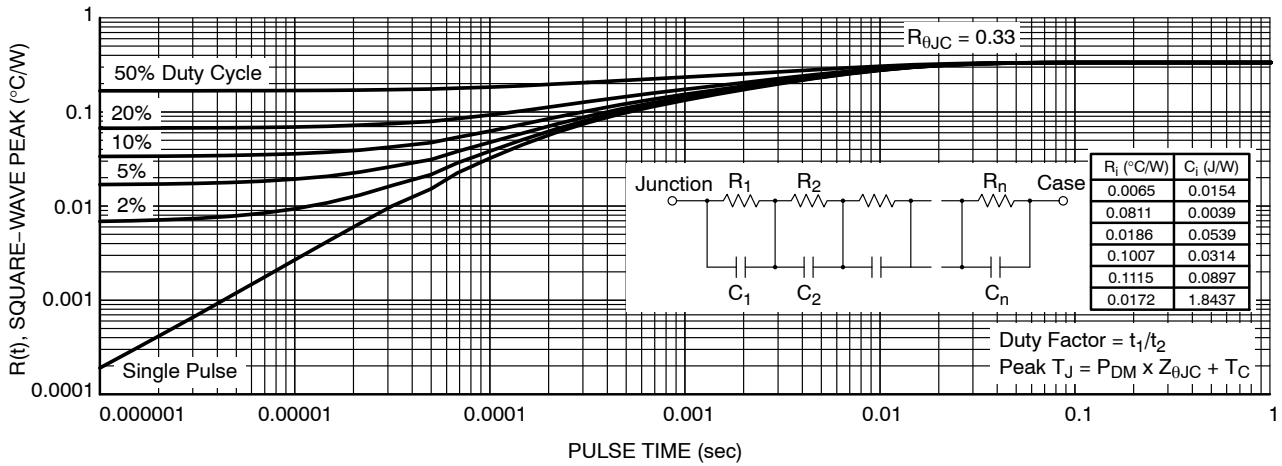


Figure 25. IGBT Transient Thermal Impedance

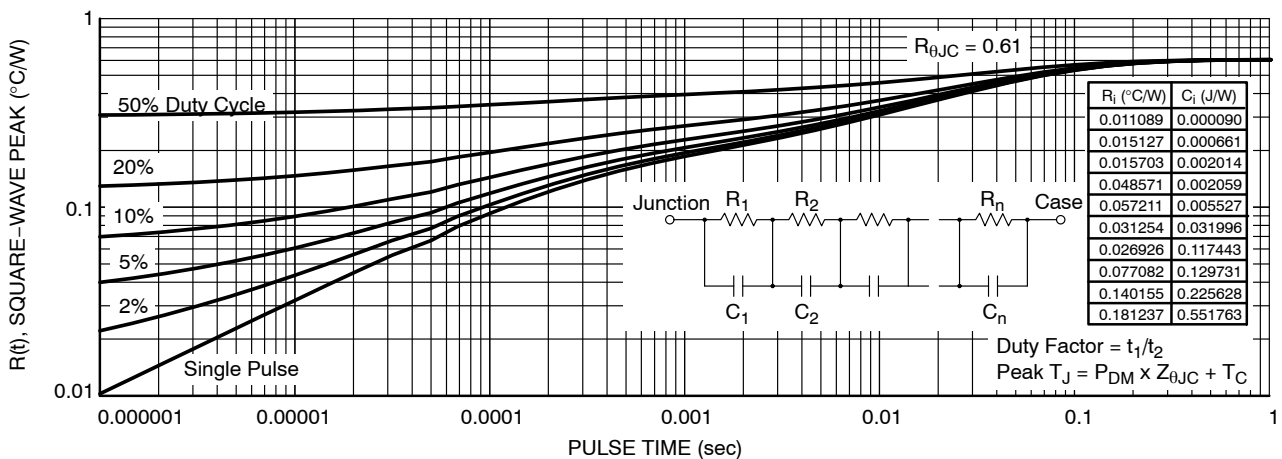


Figure 26. Diode Transient Thermal Impedance

FGH40T120SQDNL4

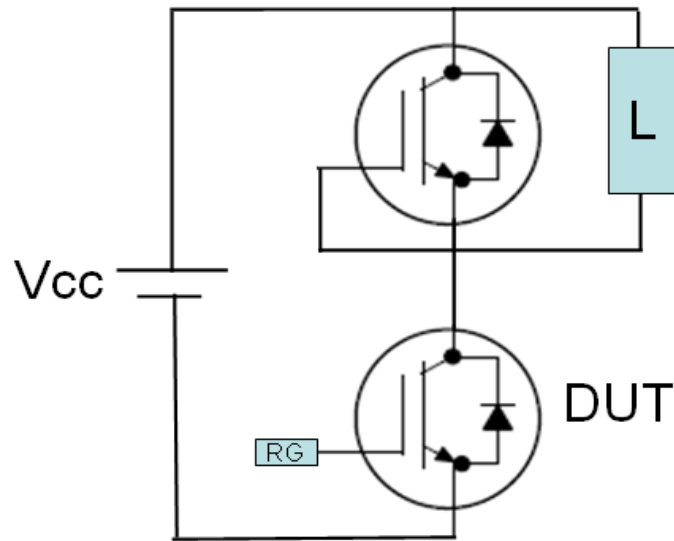


Figure 27. Test Circuit for Switching Characteristics

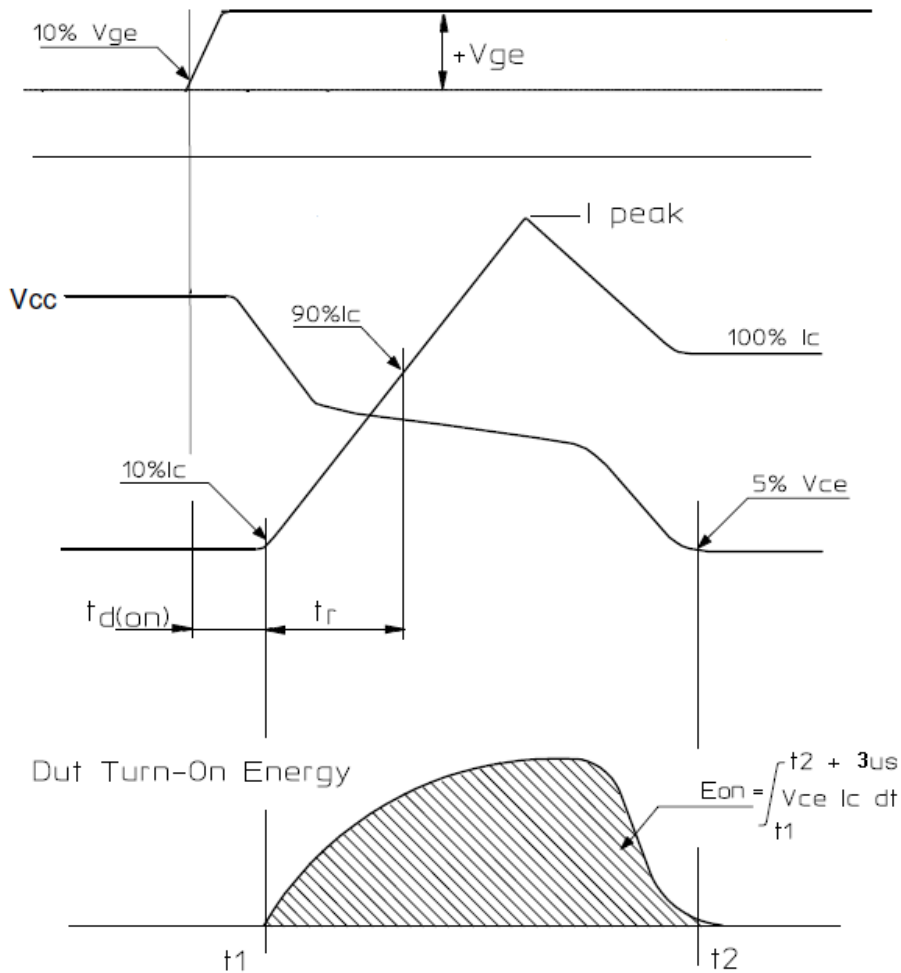


Figure 28. Definition of Turn On Waveform

FGH40T120SQDNL4

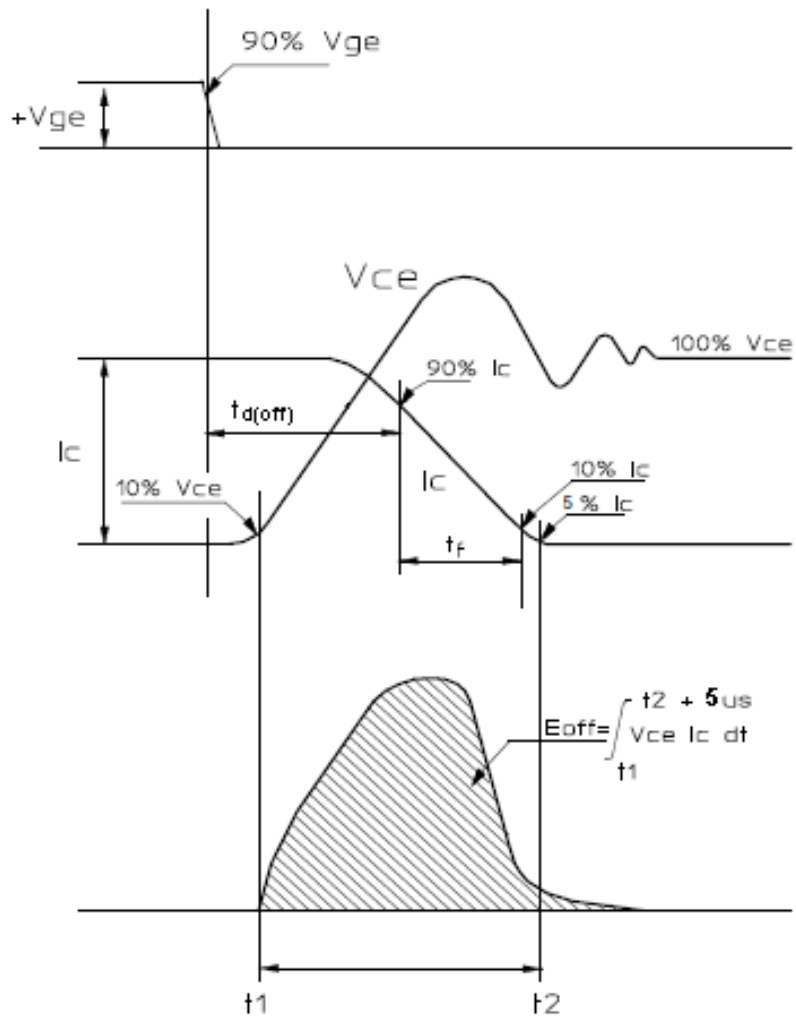
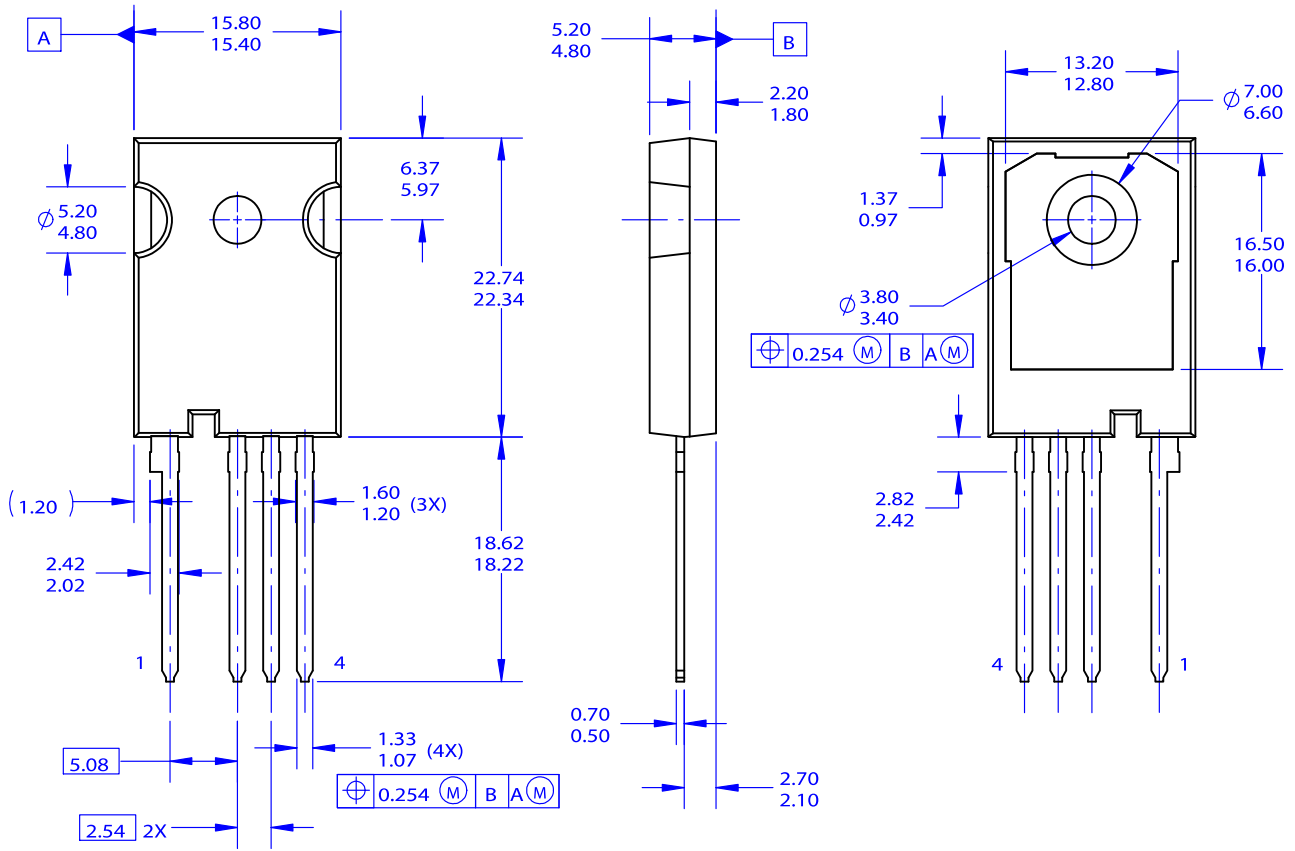


Figure 29. Definition of Turn Off Waveform

FGH40T120SQDNL4

PACKAGE DIMENSIONS

TO-247-4LD
CASE 340CJ
ISSUE O



NOTES:

- A. NO INDUSTRY STANDARD APPLIES TO THIS PACKAGE.
- B. DIMENSIONS ARE EXCLUSIVE OF BURRS, MOLD FLASH, AND TIE BAR EXTRUSIONS.
- C. ALL DIMENSIONS ARE IN MILLIMETERS.
- D. DRAWING CONFORMS TO ASME Y14.5-2009.

ON Semiconductor and are trademarks of Semiconductor Components Industries, LLC dba ON Semiconductor or its subsidiaries in the United States and/or other countries. ON Semiconductor owns the rights to a number of patents, trademarks, copyrights, trade secrets, and other intellectual property. A listing of ON Semiconductor's product/patent coverage may be accessed at www.onsemi.com/site/pdf/Patent-Marking.pdf. ON Semiconductor reserves the right to make changes without further notice to any products herein. ON Semiconductor makes no warranty, representation or guarantee regarding the suitability of its products for any particular purpose, nor does ON Semiconductor assume any liability arising out of the application or use of any product or circuit, and specifically disclaims any and all liability, including without limitation special, consequential or incidental damages. Buyer is responsible for its products and applications using ON Semiconductor products, including compliance with all laws, regulations and safety requirements or standards, regardless of any support or applications information provided by ON Semiconductor. "Typical" parameters which may be provided in ON Semiconductor data sheets and/or specifications can and do vary in different applications and actual performance may vary over time. All operating parameters, including "Typicals" must be validated for each customer application by customer's technical experts. ON Semiconductor does not convey any license under its patent rights nor the rights of others. ON Semiconductor products are not designed, intended, or authorized for use as a critical component in life support systems or any FDA Class 3 medical devices or medical devices with a same or similar classification in a foreign jurisdiction or any devices intended for implantation in the human body. Should Buyer purchase or use ON Semiconductor products for any such unintended or unauthorized application, Buyer shall indemnify and hold ON Semiconductor and its officers, employees, subsidiaries, affiliates, and distributors harmless against all claims, costs, damages, and expenses, and reasonable attorney fees arising out of, directly or indirectly, any claim of personal injury or death associated with such unintended or unauthorized use, even if such claim alleges that ON Semiconductor was negligent regarding the design or manufacture of the part. ON Semiconductor is an Equal Opportunity/Affirmative Action Employer. This literature is subject to all applicable copyright laws and is not for resale in any manner.

PUBLICATION ORDERING INFORMATION

LITERATURE FULFILLMENT:

Literature Distribution Center for ON Semiconductor
19521 E. 32nd Pkwy, Aurora, Colorado 80011 USA
Phone: 303-675-2175 or 800-344-3860 Toll Free USA/Canada
Fax: 303-675-2176 or 800-344-3867 Toll Free USA/Canada
Email: orderlit@onsemi.com

N. American Technical Support: 800-282-9855 Toll Free
USA/Canada

Europe, Middle East and Africa Technical Support:
Phone: 421 33 790 2910

ON Semiconductor Website: www.onsemi.com

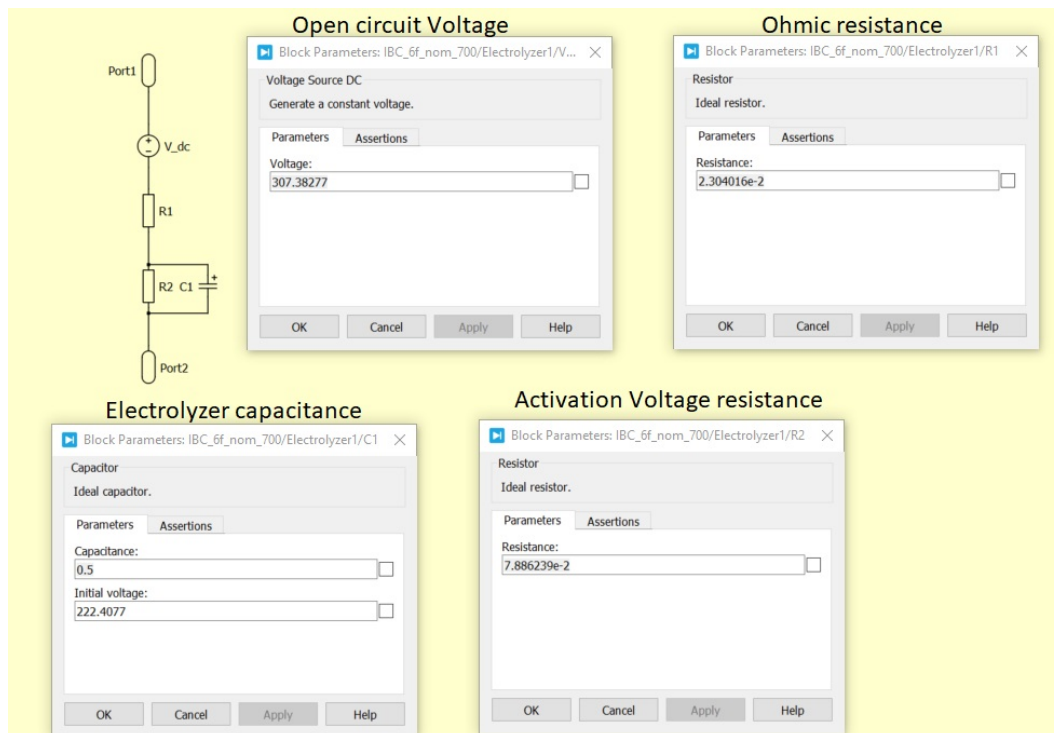
Order Literature: <http://www.onsemi.com/orderlit>

For additional information, please contact your local Sales Representative

Appendix C

Detailed Plecs Models

C.1 Electrolyzer Model



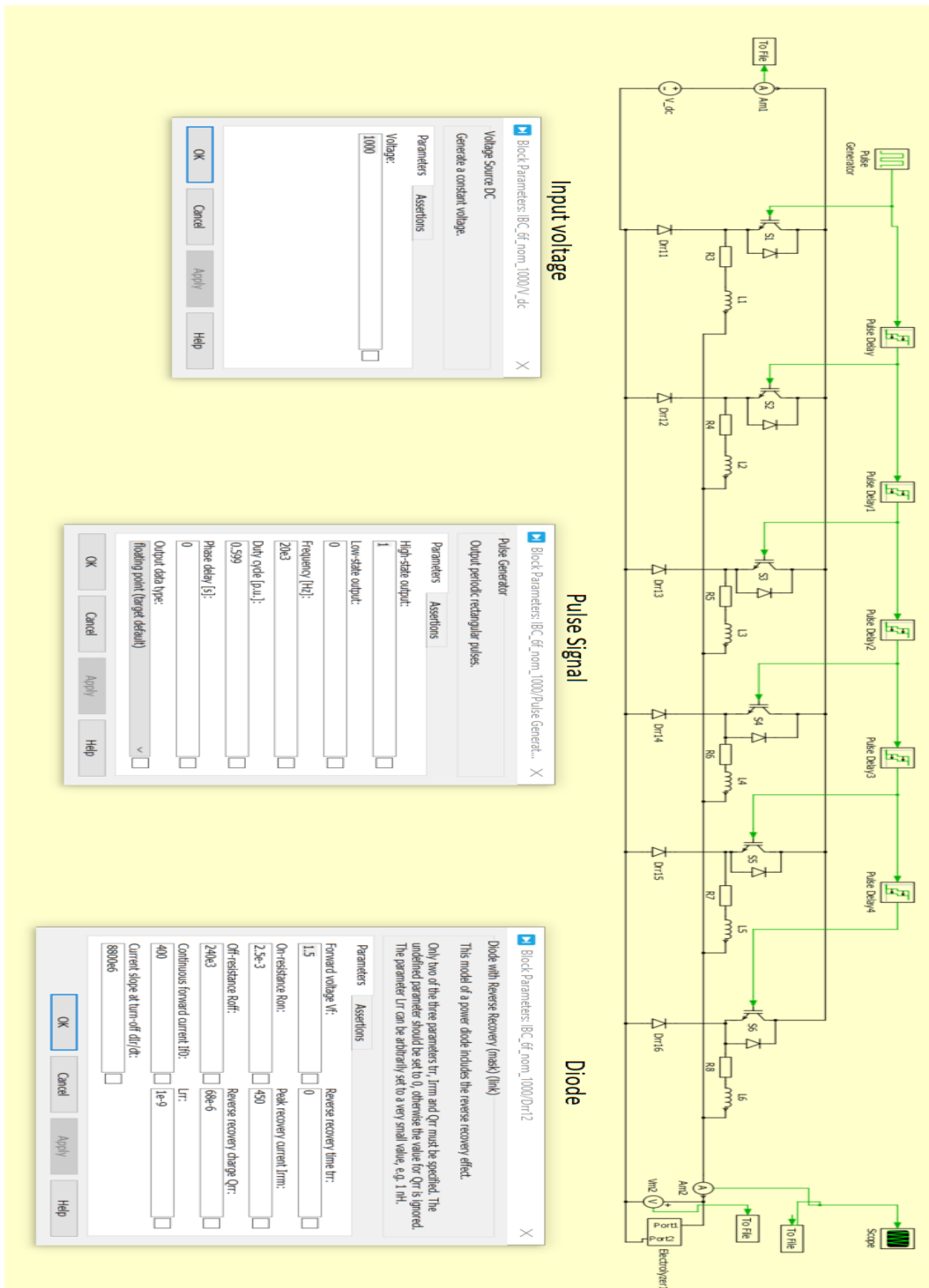
C.2 700 V IBC Model

The image displays a circuit simulation software interface for a 700V IBC model. The main window shows a circuit diagram with a 700V DC voltage source, a pulse generator, and an IGBT module. The IGBT module consists of three IGBTs (IGBT1, IGBT2, IGBT3) and three diodes (Diode1, Diode2, Diode3). The circuit is connected to a 10mV probe and a 10mV scope. The simulation results are shown in a plot window.

Several dialog boxes are open, showing the configuration of various components:

- Input voltage:** Block Parameters: BC_of_nom_700V_dc. Parameters: Voltage: 700.
- Pulse signal:** Block Parameters: BC_of_nom_700/Pulse Generator. Parameters: High-state output: 1, Low-state output: 0, Frequency [Hz]: 20k, Duty cycle [p.u.]: 0.3333, Phase delay [S]: 0, Output data type: Floating point (user default).
- Pulse delay:** Block Parameters: BC_of_nom_700/Pulse Delay. Parameters: Time delay: 1/(6*20k), Initial output: 0.
- IGBT Diode:** Block Parameters: BC_of_nom_700/D7. Parameters: Forward voltage V_F: 2.5-3, On-resistance Ron: 0.
- IGBT Module:** Block Parameters: BC_of_nom_700/S1. Parameters: Blocking voltage V_{ces}: 1200, Continuous collector current I_c: 600, Forward voltage V_F: 0.8, On-resistance Ron: 0.025, Off-resistance Roff: 2.45.
- Diode:** Block Parameters: BC_of_nom_700/Dn2. Parameters: Reverse recovery time trr: 1.2, On-resistance Ron: 4.6e-3, Off-resistance Roff: 0.236, Continuous forward current Ifc: 1.77, Current slope at turn-off di/dt: 200e.
- Parasitic inductor resistance:** Block Parameters: BC_of_nom_700/R4. Parameters: Resistor: Ideal resistor, Resistance: 27e-3.
- Inductor:** Block Parameters: BC_of_nom_700/L2. Parameters: Inductor: Ideal Inductor, Inductance: 5e-6, Initial current: 0.

C.3 1000 V IBC Model



Appendix D

PV Case Study Scripts

D.1 Solar Generation Data Processing

```
1 SF = readmatrix('Solar hours Belgium.csv'); %data from
   renewables.ninja
2 SFM = readmatrix('Solar hours Morocco.csv');
3 Pg = SF(1:8784,5)/1000; %Output power Blgium
4 PgM = SFM(1:8784,5)/1000; %Output power Morocco
5 M = size(Pg,1);
6 eff = [0, 0.99276, 0.99393, 0.9937, 0.99383, 0.99381,
        0.99370, 0.99366, 0.99350, 0.99328, 0.99322, 0.99296,
        0.99284, 0.99269, 0.99263, 0.99242, 0.992314, 0.9920,
        0.99211]; %Converter efficiency at input power
   setpoints
7 P_in = [0, 85, 100, 200, 300, 400, 500, 600, 700, 800,
        900, 1000, 1100, 1200, 1300, 1400,1500,1600,1677.37] ./
   eff;
8 Qn = zeros(19,1);
9 Qv = transpose(P_in);
10 Q = [Qv Qn Qn];
11 for i = 1:M
12     if Pg(i) < Qv(2)
13         Q(1,2) = Q(1,2) +1;
14     else
15         a = min(abs(Qv - Pg(i)));
16         [~,idx] = min(abs(Qv - Pg(i)));
17         Q(idx,2) = Q(idx,2) + 1;
18     end
19     if PgM(i) < Qv(2)
20         Q(1,3) = Q(1,3) +1;
21     else
22         a = min(abs(Qv - PgM(i)));
```

```

23         [~,idx] = min(abs(Qv - PgM(i)));
24         Q(idx,3) = Q(idx,3) + 1;
25     end
26 end

```

D.2 Approximate IU-Setpoint Calculation

```

1  %find optimal current and voltage to operate electrolyzer
   at given input
2  %power
3  Q = transpose([0, 85, 100, 200, 300, 400, 500, 600, 700,
   800, 900, 1000, 1100, 1200, 1300, 1400, 1500, 1600,
   1677.37]);
4  Pi = Q;
5  Pi(:,[2 3]) = 0;
6  [~,Po_inv] = Pin();
7  %Pi(2:end,1) = Po_inv; %% include these lines to
   calculate the electrolyzer input power after an
   inverter-rectifier step
8  for p = 1:size(Pi,1)
9      P = Pi(p,1)*1000;
10     %find the most efficient rate at which hydrogen can be
        produced
11     t_end = 10;
12     n = 100;
13     I_max = 2820.2; %maximum rated current
14     i = 10;
15     er = 10^6;
16     timesteps = transpose(linspace(0,t_end,n));
17     while i <= I_max
18         Vp = P/i;
19         I_in = ones(size(timesteps))*i;
20         simI = [timesteps I_in];
21         %run simulink model
22         res = sim("cell_model.slx");
23         %extract output
24         Voc = res.Voc(end,1);
25         Vel = res.Vel(end,1);
26         I_max = min(P/Voc,2820.2); %maximum current if
            minimum voltage Voc is used, or total rated
            current
27         if Vel <= Vp
28             if Vp-Vel < er

```



```

29         er = Vp-Vel;
30         if i < I_max
31             I = i;
32             V = Vel;
33         end
34         Pi(p,2) = I;
35         Pi(p,3) = V;
36     end
37 end
38 i = i+10; %to reduce iterations, current is
          calculated with accuracy of 10^-1 in this script
39
40 I_max = min(P/Voc,2820.2);
41 end
42 end

```

D.2.1 Inverter-based input power

```

1 function [P_in,Pow_inv] = Pin()
2 Pow = [85, 100, 200, 300, 400, 500, 600, 700, 800, 900,
        1000, 1100, 1200, 1300, 1400, 1500, 1600, 1677]; %
        electrolyzer input power in DC conditions
3 eff = [99.34, 99.34, 99.37, 99.36, 99.37, 99.35, 99.33,
        99.30, 99.28, 99.27, 99.25, 99.24, 99.21, 99.20,
        99.19, 99.17 99.17, 99.17]; %DC/DC converter at
        considered power setpoints
4 P_in = Pow./(eff/100); %PV power generation
5 Pow_inv = P_in*0.97^2; %Electrolyzer input power after
        inverter-rectifier step
6 end

```

D.3 Detailed IU-Setpoint Calculation

```

1 %detailed power setpoint calculation
2 Pi_def = Pi;
3 for p = 2:size(Pi,1)
4     P = Pi(p,1)*1000;
5     t_end = 10;
6     n = 100;
7     I_max = min(Pi(p,2)+10,2820.1);
8     i = Pi(p,2)-10; %calculate the optimal current in
        steps of 1 A in the interval of [-10,+10] around
        the approximate calculation

```

```
9   er = 10^6;
10  timesteps = transpose(linspace(0,t_end,n));
11  while i <= I_max
12      Vp = P/i;
13      I_in = ones(size(timesteps))*i;
14      simI = [timesteps I_in];
15      %run simulink
16      res = sim("cell_model.slx");
17      %extract output
18      Vel = res.Vel(end,1);
19      Voc = res.Voc(end,1);
20      if Vel <= Vp
21          if Vp-Vel < er
22              er = Vp-Vel;
23              I = i;
24              V = Vel;
25              Pi_def(p,2) = I;
26              Pi_def(p,3) = V;
27              Pi_def(p,4) = Voc;
28          end
29      end
30      i = i+1;
31  end
32 end
```